

COMMISSIONING OF THE SEPARATOR FOR CAPTURE REACTIONS IN
ASTROPHYSICS

By

Sara Ayoub Miskovich

A DISSERTATION

Submitted to
Michigan State University
in partial fulfillment of the requirements
for the degree of

Physics - Doctor of Philosophy

2021

ABSTRACT

COMMISSIONING OF THE SEPARATOR FOR CAPTURE REACTIONS IN ASTROPHYSICS

By

Sara Ayoub Miskovich

The SEparator for CAPture Reactions (SECAR) [6] is a next-generation recoil mass separator system at the National Superconducting Cyclotron Laboratory (NSCL) and Facility for Rare Isotope Beams (FRIB) at Michigan State University. SECAR was designed for precise and direct measurements of reaction rates relevant to the explosive synthesis of elements in astrophysical sites such as X-ray bursts and novae. Once SECAR is operational, it will be utilized for precise measurements of low energy (p,γ) and (p,α) reactions in inverse kinematics with beams of proton-rich radioactive nuclei of masses up to $A = 65$. The work discussed in this thesis was dedicated to the commissioning of the beamline, including diagnostic devices, to characterizing the system, and defining operational approaches that ensure reliable, reproducible, and optimal performance.

To maximize the performance of the device, careful beam alignment to the central ion optical axis needs to be achieved, which can be difficult to attain through manual tuning in a quantitative and reproducible way. Additionally, the ion optical settings need to be verified and optimized to ensure adequate mass separation. In this thesis, the first development of an online Bayesian optimization with a Gaussian process model to tune a nuclear astrophysics recoil separator and improve its ion optical properties is reported. The method is shown to improve recoil separator performance, increase objectivity and reproducibility, and reduce setup and tuning time significantly. It is now used routinely for all separator tuning.

As precise knowledge of the beam energy is critical when measuring narrow resonances,

the energy calibration of the first bending dipole pair was performed to provide independent incoming beam energy determinations in the SECAR system. This was achieved through the measurement of the γ -ray yields of the $^{27}\text{Al}(p,\gamma)^{28}\text{Si}$ resonances at $E_p = 992$ and 1800 keV/u with a BGO (Bismuth Germanate) array at the SECAR target chamber. Two measurements were obtained for each resonance, one with a H^+ beam and one with a H_2^+ , to cover a larger rigidity range. By fitting the observed γ -ray yields with a thick target yield curve, a dipole calibration factor of $k = 3.6501 \times 10^{-3} \pm 6.2 \times 10^{-6}$ (0.17%) $\text{T}/\sqrt{\text{keVamu}}$ was obtained. To achieve higher accuracy when extrapolating to higher energies, the energy calibration was also performed taking into account relativistic effects.

This commissioning work paves the way for SECAR to achieve its scientific goals of improving our understanding of stellar explosions. By providing accurate thermonuclear reaction rates, astrophysical models will in turn provide better understanding of explosions such as novae and X-ray bursts.

Dedicated to Mounir Sholy.

ACKNOWLEDGMENTS

First, I want to thank my advisor Hendrik Schatz, and Fernando Montes for all their support and patience throughout my years in graduate school. This work would not have been possible without the help of the entire nuclear astrophysics group and everyone who took part in the many commissioning runs we had. Know that I thank you all for your help, especially Louis Wagner, Rahul Jain, Kirby Hermansen, Nabin Rijal, April Garrity, Justin Browne, Stephanie Lyons, and Konrad Schmidt. I am thankful for the SECAR collaboration, and in particular Michael Smith, Manoel Couder, Georg Berg and Kelly Chipps for always having an answer ready to my many questions. I also thank Elaine Yakura for her amazing support in navigating this journey, and my committee members, Alex Brown, Ed Brown, Brad Sherrill, and Kirsten Tollefson for their guidance over the years.

The commissioning of this complex beamline was a lab-wide effort, and I would like to thank everyone that supported any work that helped the completion of this thesis. I cannot possibly name everyone that was involved here, but know that I am grateful for your support. I would especially like to thank the ReA3 group, in particular Tasha Summers, Daniel Crisp, Antonio Villari, Sam Nash, and Ana Henriques for all their hard work.

Graduate school would not have been the same without the support and companionship of my friends. Our pre-covid office was always fun, thanks to Mara Grinder, Dayah Chrisman, and Aalayah Spencer. I would also like to thank Kristen Dage for being generous and helpful in every way since the day we met. Last but not least, I thank Elsie Arayes for her unyielding support and encouragement for many, many years.

I cannot thank my parents enough for their unwavering support as I pursued any dream I had, and for always believing in me no matter what. My journey would not have been

possible without the support of my wonderful family, and for that I am grateful. I particularly thank Rayane for always being there for me, and Rudy for providing support and reassurance when I needed it. Finally, I thank my husband Andrew, for calming me down when I was overwhelmed, for celebrating small victories with me, and for his never-ending support that ultimately helped me complete this degree.

TABLE OF CONTENTS

LIST OF TABLES	ix
LIST OF FIGURES	x
LIST OF ALGORITHMS	xvii
Chapter 1 Introduction	1
1.1 Motivation	1
1.2 Importance of Radiative Capture Reactions	3
1.2.1 Radiative Capture Reactions in X-ray bursts	4
1.2.2 Radiative Capture Reactions in Novae	7
1.3 Direct Measurement of Radiative Capture Reactions	9
1.3.1 Experimental Studies	9
1.3.2 Inverse Kinematics	10
1.3.3 Recoil Separator Design Principles	13
1.3.4 Previous Recoil Separators	18
1.4 SECAR at FRIB and NSCL	22
1.5 Machine Learning for Tuning Optimization	23
Chapter 2 Experimental Determination of Astrophysical Stellar Rates	25
2.1 Stellar Reaction Rates	25
2.2 Narrow Resonances	28
2.3 Narrow Resonance Yields	31
Chapter 3 SECAR Design and Experimental Setup	38
3.1 The NSCL and ReA3 Facility	38
3.2 The FRIB Facility	39
3.3 The SECAR Design	40
3.3.1 Design Properties	44
3.3.2 Ion Optical Design	45
3.4 Beam Diagnostics	52
3.5 Gas Target Systems	57
3.5.1 JENSA Target System	58
3.5.2 Extended Gas Target System	61
3.6 Detectors and Data Acquisition	62
3.6.1 Gamma-Ray Detection	63
3.6.2 Recoil Detection	65
3.6.3 Digital Data Acquisition System	72

Chapter 4	Beamline Commissioning	73
4.1	Separator Control System	73
4.2	Magnet Stability and Reproducibility	76
4.2.1	Magnet Cycling and Hysteresis	77
4.2.2	Long Term Stability Tests	79
4.3	Initial Tests with Beam	85
4.3.1	Diagnostic Devices Tests	87
Chapter 5	Tuning and Bayesian Optimization	97
5.1	Tuning Methods	97
5.1.1	Manual Tuning Procedure	99
5.2	Dipoles and WF Tuning	103
5.3	Bayesian Optimization for Beam Tuning	106
5.3.1	The Bayesian Approach	107
5.3.2	Gaussian Processes	110
5.3.3	Hyperparameter Selection	114
5.3.4	Acquisition Functions	116
5.3.5	Method and Algorithm	119
5.3.6	Beam Incoming Angle Optimization	121
5.3.7	Ion Optics Optimization	131
Chapter 6	Dipole Energy Calibration	141
6.1	Theory	141
6.2	Resonant Reactions and Target Properties	143
6.3	Experimental Setup	145
6.3.1	Target Installation	146
6.3.2	Gamma Detection Array	146
6.3.3	SECAR Beamline	149
6.4	Experimental Procedures	150
6.5	Analysis and Errors	152
6.5.1	Beam Current Integration and Normalization	152
6.5.2	Dipole Field Determination	153
6.5.3	Gamma-ray Spectra	155
6.5.4	Yield Curve Fitting and Uncertainties	158
6.5.5	Energy Calibration Results	164
Chapter 7	Conclusions	172
7.1	Next Steps and Future Developments	174
REFERENCES		178

LIST OF TABLES

Table 3.1:	SECAR separator properties for optimized direct measurements of p- and α -capture reactions on unstable proton-heavy nuclei.	45
Table 3.2:	Pole tip magnetic fields for COSY INFINITY nominal tune at 0.8 Tm used in this work.	53
Table 3.3:	Beam requirements for optimal recoil separation in SECAR.	53
Table 4.1:	SECAR commissioning runs.	86
Table 4.2:	Faraday cup collector current readbacks up to FP2 after tuning the $^{20}\text{Ne}^{8+}$ beam in July 2020.	91
Table 5.1:	Slit gaps needed to admit the 2σ beam width within dE/E for each tune.	137
Table 5.2:	Beam spot diameter at FP2 calculated in COSY with a target width of 1.5 mm (2σ), compared to the widths ($\pm 2\sigma$) measured experimentally with the nominal beam settings and with the best settings after optimization.	137
Table 6.1:	Parameters of $^{27}\text{Al}(p,\gamma)^{28}\text{Si}$ resonances scanned for the dipole calibration.	143
Table 6.2:	Calibration factors, beam energy spreads and calibration dipole fields obtained for the $^{27}\text{Al}(p,\gamma)^{28}\text{Si}$ resonance energies with their statistical uncertainties.	164

LIST OF FIGURES

Figure 1.1:	Simplified illustration of resonant radiative capture in the laboratory frame.	11
Figure 1.2:	Maximum recoil half-angle in the laboratory frame as a function of the center of mass energy for a number of reactions of astrophysical interest.	13
Figure 2.1:	Maxwell-Boltzmann factor (dashed line) and Gamow factor (dotted line) versus energy for an arbitrary temperature T. The product $e^{-k_b T} e^{-2\pi\eta}$, representing the Gamow peak, is shown with the solid line.	28
Figure 2.2:	Yield curve normalized to Y_{max} for a thick target based on Equation 2.29 with a small beam energy spread $\delta = 0.005\%$	35
Figure 3.1:	The SECAR recoil separator layout in the ReA3 Hall at MSU. The beam enters the hall from the middle left into the JENSA gas jet target system, and the capture reaction recoils along with the unreacted projectiles enter the first section in SECAR that selects a single charge state. Two subsequent sections each including a velocity filter (WF1, WF2) serve to reject the remaining projectiles, and the final cleanup section features a final pair of dipoles before particles enter the focal plane detection system.	40
Figure 3.2:	SECAR in the ReA3 Hall showing B1 up to Hex3.	41
Figure 3.3:	SECAR in the ReA3 Hall showing B5 up to the final focal plane.	41
Figure 3.4:	The ion optics of SECAR for the layout explained in Section 3.3 corrected up to fourth order. The four sections are shown in different colors. Traces of rays in the horizontal (a) and vertical (b) planes are shown.	50
Figure 3.5:	Example COSY INFINITY ion optics calculation up to the first mass separation slits of a $^{65}\text{As}(p,\gamma)^{66}\text{Se}$ reaction in the x-plane. The Se recoils are shown in black, unreacted As beam of similar $B\rho$ is shown in blue, and a beam of a nearby charge state is shown in red ($\delta Q/Q = 1/21$).	51
Figure 3.6:	Diagnostics along the SECAR beamline.	54

Figure 3.7:	Faraday cup design for SECAR (left). Cup design in 3-in-1 device at FP1 (right).	55
Figure 3.8:	BCM design for SECAR shown on 3-in-1 device at FP1. Aluminum nitride (AlN) ceramic plate serves to electrically isolate the plates.	56
Figure 3.9:	CAD drawing of JENSA chamber and its differential pumping components. The distance from the target location to the end of the final downstream pumping stage is 73 cm. Beam direction is right to left.	59
Figure 3.10:	The JENSA nozzle and receiver installed in the ReA3 Hall. Beam direction is right to left.	60
Figure 3.11:	JENSA gas target assembly in the ReA3 Hall upstream of SECAR. SECAR elements up to Q5 shown. JENSA compressor shown in white on the left.	61
Figure 3.12:	Drawing of the extended gas cell designed for use with SECAR at the Colorado School of Mines. Scale is in mm.	62
Figure 3.13:	Current γ -array comprised of 19 BGO crystals for use with the JENSA gas jet (a,b), with a CAD showing the flange installed on the beamline left of the JENSA target looking downstream (c).	66
Figure 3.14:	Drawing of BGO array around the extended gas cell as designed at the Colorado School of Mines.	67
Figure 3.15:	Schematic of the focal plane detection system at FP4.	67
Figure 3.16:	One of the accelerating grids and foil after assembly (left) and the MCP detector installed in the beamline (right). Once installed, the foil sits at 45° relative to the beam axis and parallel to the MCP detector.	69
Figure 3.17:	The ΔE -Si detector showing the grids and DSSD assembled before installation on the beamline.	71
Figure 4.1:	The main global controls page for SECAR. Top left shows the magnet light that controls the ReA3 Hall SECAR light when the magnets are one, and to the right several buttons provide options to switch to other pages. The general menu tabs below show the magnet controls in this image.	74
Figure 4.2:	The vacuum summary page showing the controls and status of vacuum gauges and turbo pumps.	75

Figure 4.3:	The controls page for SECAR showing the tab for controls during tuning. This was developed for use during experiments.	75
Figure 4.4:	Dipole B1 magnetic field reproducibility measured with the NMR probe after 1 cycle with 30 s pause time. $N = 208$	78
Figure 4.5:	Quadrupole Q6 magnetic field reproducibility using two different cycling procedures, measured with a Group 3 Hall probe.	79
Figure 4.6:	Dipole B1 magnetic field long term stability test as measured with NMR (top) and Hall probe (bottom). The dot-dashed lines correspond to $\pm 0.01\%$ stability levels. The flat lines between July 26 and July 29 correspond to a control system connection drop.	80
Figure 4.7:	Dipole B1 magnetic field long term stability test as measured with NMR (top) and Hall probe (middle) in the presence of an external heating source from from 25 to 37°C. The dot-dashed lines correspond to $\pm 0.01\%$ stability levels and the black vertical line indicates the onset of heating. Bottom plot shows the Hall probe's temperature sensor readback.	82
Figure 4.8:	Dipole B5 magnetic field long term stability test as measured with a Hall probe. The dot-dashed lines correspond to $\pm 0.01\%$ stability levels.	83
Figure 4.9:	Quadrupole Q1 magnetic field long term stability test as measured with two Hall probes placed at different pole radii. The ambient temperature near the power supply rack (mezzanine) is shown in red. The overlaid dot-dashed lines correspond to $\pm 0.01\%$ of the mean of each reading.	84
Figure 4.10:	First beam spot on the FP1 viewer in SECAR on July 13, 2018.	85
Figure 4.11:	FC1 assembled in the clean room.	88
Figure 4.12:	The 3-in-1 diagnostic drive to be installed at FP1, assembled in the clean room. From left to right: BCM, Faraday cup, and viewer plate (uncoated).	88
Figure 4.13:	A P22 coat on the Viewer2 plate before installation.	89
Figure 4.14:	Viewer1 installed and inserted in the beamline.	89
Figure 4.15:	FC1 suppression voltage test.	90

Figure 4.16:	Viewer image analysis process. Left: CCD image of the image with light on to find scale from the 5 mm dot markings. Center: Raw TIFF image of the beam from CCD. Right: Background subtracted beam image with the red lines marking the beam spot center, and red dots indicating the center with 5 mm distance between each dot. In this image, each pixel corresponds to approximately 0.15 mm.	92
Figure 4.17:	Viewer image analysis at FP1: Red lines indicate beam center as calculated from the median of the distribution, blue dashed lines indicate the width in the x-direction defined as $\pm 1\sigma$. The locations are indicated in pixels, and the scale is 5 mm to 16 pixels.	93
Figure 4.18:	Top: Normalized currents on the left side (blue) and right side (orange) as a function of time. The point where they cross is the center region of the BCM. The uncertainty on the measurements is shown in the shaded region. Bottom: Ratio of left current to right current on the BCM. It should be equal to 1 when the beam crosses the center of the BCM.	95
Figure 4.19:	Final results showing the left side current (blue) and right side current (orange) as a function of dipole current. The shaded region of overlapping blue and orange between 110.67 and 110.71 A is the region when the beam was centered.	95
Figure 5.1:	(a): SECAR layout with notable diagnostics used for tuning, including the upstream ReA3 beamline with the two steerer sets used for correcting the incoming angle. The first set is 7.2 m away from the first SECAR quadrupole, and the two sets are 1.8 m apart. (b): JENSA viewer and slits used in the manual tuning procedure.	100
Figure 5.2:	B1 - B2 dipole scan in steps of 0.06 A on FP1 to minimize steering in Q3 - Q5. The steering does not reach zero in this case, and this may be due to small deviations of the beam from the center that are not corrected at FP1. Fine tuning downstream where sensitivity to such small deviations is increased is often needed.	105
Figure 5.3:	B1 - B2 dipole scan in steps of 0.02 A on FP1 to minimize steering in Q3/Q4.	106
Figure 5.4:	WF1 dipole magnet scan to minimize steering in Q8 and Q9 measured at D1688. The best field corresponding to the beam leaving the WF at the center is shown by the red dashed line.	107
Figure 5.5:	Conditional probability of x_2 given x_1	111

Figure 5.6:	The effect of the lengthscale hyperparameter on the SE kernel from Equation 5.8 for $\ell = 0.2, 1, 2$. For each hyperparameter value, the function $k_{SE} = (0, \mathbf{x})$ is shown on the left and random samples from the Gaussian process prior are shown on the right.	115
Figure 5.7:	Sampling of an observation at the viewer. Four images taken at different quadrupole tunes are shown with the beam center location with respect to the central red dot in mm. The mean steering distance between the four beam spots is 4.7 mm.	122
Figure 5.8:	The posterior mean (left), standard deviation of the mean (middle) and acquisition function (right) for three different 2D steerer optimization runs. The observations are shown in the first left and middle columns by dots shaded by time of observation, with the darkest shade of red being the most recent observation. The next sample point is shown in the right column by the white cross indicating the minimum of the acquisition function. The most recent mean value for lengthscale and noise variance priors are noted for each, as well as the exploration weight used.	127
Figure 5.9:	Best steering distance reached as a function of number of GP iterations, for 2D (vertical) and 4D optimizations during two different beam commissioning runs.	128
Figure 5.10:	Beam spot steering at FP1 before (a - d) and after (e - h) optimization of the beam angle for a 4D run with a ^{20}Ne beam. The steering decreased from an average of 7 mm to an average of 0.2 mm. All axes are in pixels, and 16 pixels correspond to 5 mm.	130
Figure 5.11:	(a) Nominal and (b) after the GP optimization at FP2 for the ^{133}Cs commissioning run. Red dots indicate 5 mm. X-axis scale is in pixels, where 31 pixels is 5 mm.	137
Figure 5.12:	Minimum of the objective function defined in Equation 5.23, reached as a function of number of GP iterations, for 8D and 9D optimizations.	138
Figure 5.13:	The ^{20}Ne beam $\pm 1\sigma$ widths within the energy acceptance. Scale is 31 pixels to 5 mm.	139
Figure 6.1:	Effect of the beam energy spread on the maximum yield and on the mid-point of the rise plotted for a resonance energy of 991.86 keV/u (left) and 1799.75 keV/u (right). The energy at the mid-point is shown in dashed lines at the different energy spreads.	145

Figure 6.2:	JENSA drive setup as used for the dipole calibration runs showing from left to right: Al target foil on 4×4 mm slit, empty 4×4 mm slit, empty 1.5×1.5 mm slit, viewer (slanted at a 45° angle). In this image, the drive is retracted out of the beam's path.	146
Figure 6.3:	Setup of the 14 BGO array used for the dipole calibration runs. The flange is mounted on the JENSA chamber.	147
Figure 6.4:	Scaling of two different target run beam currents using background current readings, within error bars.	153
Figure 6.5:	B1 - B2 dipole scan on FP1 to minimize steering in Q3 - Q5. The error on the steering distance is calculated from a 1.5 pixel error on each beam spot location measurement. The dashed line indicates the region where the best field value lies.	155
Figure 6.6:	BGO array spectra of all runs scanning the 1800 keV/u resonance with H_2 beam. The incoming beam energy E_p corresponds to the ReA3 energies reported. From left to right, the resonant contribution of $^{27}Al(p,p')^{27}Al$ at 844 and 1015 keV, the $^{27}Al(p,\alpha)^{24}Mg$ peak at 1369 keV, and the $^{27}Al(p,\gamma)^{28}Si$ peak at 1779 keV are seen.	156
Figure 6.7:	The 1779 keV peak at the $E_p = 1800$ keV/u resonance with a Gaussian (green) and a exponential (magenta) plus constant (cyan) background fits. On the left is the (p,α) peak with a Gaussian fit (blue).	157
Figure 6.8:	The $^{27}Al(p,\gamma)^{28}Si$ resonance at 992 keV/u with an H_2^+ beam. The solid curve is the theoretical yield fit to the data. The dark gray shaded area indicates the region of the magnetic field at E_R within the statistical error of the fit. The light gray shaded area is the total error.	161
Figure 6.9:	The $^{27}Al(p,\gamma)^{28}Si$ resonance at 992 keV/u with an H^+ beam.	162
Figure 6.10:	The $^{27}Al(p,\gamma)^{28}Si$ resonance at 1800 keV/u with an H_2^+ beam.	162
Figure 6.11:	The $^{27}Al(p,\gamma)^{28}Si$ resonance at 1800 keV/u with an H^+ beam.	163
Figure 6.12:	Calibration fit to the fields at the resonance energies and their corresponding errors and residuals. The slope is the dipole calibration factor k	165

Figure 6.13:	Projected energy of a $^{20}\text{Ne}^{8+}$ beam over the B range in keV (top) and its projected error in keV (middle) and percent (bottom). . . .	166
Figure 6.14:	The difference between the reported energy ($\Delta E/E \sim 0.25\%$) at the mid-point of each scanned curve and the known resonance energy. . .	167
Figure 6.15:	Relativistic calibration fit to the fields at the resonance energies and their corresponding errors and residuals.	169
Figure 6.16:	Projected E^* of a $^{20}\text{Ne}^{8+}$ beam over the B range (top), its projected error (middle), and percent error (bottom).	170
Figure 6.17:	The relativistic kinetic energy KE (top), the non-relativistic kinetic energy KE_0 (middle), and their ratio with its error shown with the shaded region (bottom) for a $^{20}\text{Ne}^{8+}$ beam over the B range. . . .	171

LIST OF ALGORITHMS

Algorithm 1: General Bayesian optimization algorithm for SECAR tuning. . . . 120

Chapter 1

Introduction

1.1 Motivation

The SEparator for CAPture Reactions (SECAR) [6] at the National Superconducting Cyclotron Laboratory (NSCL) and the Facility for Rare Isotope Beams (FRIB) was designed for precise and direct measurements of reaction rates relevant to the explosive synthesis of elements in astrophysical sites such as X-ray bursts and novae, namely proton and α -capture reactions on proton-rich radioactive nuclei. The present work focuses on the commissioning of the device, a first step to developing the experimental approach and establishing device operations to achieve the scientific goals.

As SECAR is a precision device, much of this work was dedicated to characterize the system and define operational approaches that ensure adequate performance. In the initial stages of the commissioning, a significant effort was made to define the beam properties and initial conditions that need to be met at the start of each experiment to optimize SECAR operations, and to implement the necessary diagnostics. To address challenges related to the complexity of the system, tuning procedures were developed and ultimately improved by implementing autonomous and machine learning (ML) based algorithms to achieve the necessary reproducibility and precision. At the same time this novel approach reduces setup and tuning time significantly enabling more efficient use of the system by future users. This work presents a working concept of an ML-based online tuning method that can be

improved as needed to further optimize the performance of SECAR. The approach will also be applicable to other ion optical devices and beamlines. Finally, the first two bending magnets were calibrated to facilitate independent measurements of the incoming beam energy in SECAR when measuring narrow resonant reactions that require precise knowledge of the beam energy.

Ultimately this work paves the way for SECAR to achieve its scientific goals. Crucial to understanding stellar explosions, accurate thermonuclear reaction rates will be determined with SECAR. These determinations will help address the origin of the elements, use X-ray bursts as probes of dense matter in neutron stars, and answer the many open questions related to nova explosions that occur on the surface of accreting white dwarfs.

In the following section, the astrophysical motivation behind the study of radiative capture reactions is presented. An introduction to the inverse kinematics method and to recoil separators employed in the direct measurement of radiative capture rates follows in Section 1.3. SECAR properties are introduced in Section 1.4, followed by an overview of the ML tuning optimization in Section 1.5.

In Chapter 2, an overview of stellar reaction rate theory and its application in direct resonant capture rate measurements is given. In Chapter 3, the SECAR recoil separator is presented in detail, including its beamline components and ion optical design. The commissioning and testing of its beamline devices, namely magnets and diagnostic devices, is presented in Chapter 4. Chapter 5 discusses the development of manual and autonomous ML-based tuning methods. Finally in Chapter 6, the energy calibration of the first two SECAR bending magnets is presented.

1.2 Importance of Radiative Capture Reactions

The many elements making up the universe were synthesized in various ways. The Big Bang is responsible for light elements such as hydrogen, helium and lithium [27]. After the Big Bang, a high abundance of hydrogen and helium was left over in the cosmos, enriching stellar environments. This led to the majority of the rest of the elements being formed through burning processes in stars, the latter harnessing their energy from such fusion reactions.

Most of hydrogen burning occurs inside stars during the hydrostatic equilibrium phase. Fusion of light isotopes into heavier isotopes generates the energy necessary to maintain the thermal pressure crucial to balancing the gravitational force. The two main processes that can dominate hydrogen fusion at this stage are the pp-chain (for lower mass stars such as the Sun), and the CNO-cycle (for higher mass stars that reach higher core temperatures). As a star evolves, helium accumulates from hydrogen burning, however initially the core does not reach a hot enough temperature to ignite helium fusion. Depending on the star's mass, He burning starts via the $3\text{-}\alpha$ -process either explosively with a flash as the star leaves the red giant branch, or as the core gradually reaches He burning temperature for heavier stars. The H and He nuclei present in the outer layers of a star remain abundant as the temperatures are not high enough to initiate burning even in massive stars during the final supernova explosion. However, many stars are in binary systems. Once one of the stars has ended its evolution and formed a compact remnant such as a white dwarf or a neutron star, these compact remnants can accrete the outer layers of a companion star. The accreted matter is compressed and heated on their surface, igniting explosive hydrogen and helium burning at much higher temperatures and densities than encountered during hydrostatic hydrogen or helium burning. These thermonuclear runaway events are observed as X-ray bursts and

novae in the case of neutron stars and white dwarfs, respectively, and constitute sites of hot and dense degenerate matter. In these high temperature and density environments, radiative capture reactions of proton and α nuclei involve proton-rich heavy nuclei away from stability.

These radiative capture processes are defined as two-body fusion reactions in stellar plasma where a proton or α particle captures a heavier nucleus to form a new nucleus. In a resonant capture, the nucleus and the captured particle form a compound nucleus in an excited state that subsequently emits γ -rays to finally end up in its ground or stable state. In the case of direct capture, a γ -ray is directly emitted in the capture process populating a final state. If the final state is an excited state, subsequent γ -rays are emitted as in the resonant capture. Stellar reaction rates typically have contributions from narrow and broad resonances as well as direct capture reactions.

To determine the isotopes created and understand the physics behind X-ray bursts and novae, these events must be modeled using reliable nuclear reaction data to enable valid comparisons to observations [76]. When reaction rates are known, comparisons between X-ray burst models and observations can be used as probes of neutron star properties such as mass and radius, e.g. see [38, 68, 100]. In addition to addressing questions regarding the outburst mechanism itself, novae studies can shed light on some Galactic chemical abundances that are believed to have some nova origins such as ${}^7\text{Li}$, the short-lived isotopes ${}^{22}\text{Na}$ and ${}^{26}\text{Al}$, and some CNO isotopes, particularly ${}^{15}\text{N}$ and ${}^{17}\text{O}$ [54].

1.2.1 Radiative Capture Reactions in X-ray bursts

The most frequently observable explosions in the galaxy, Type-I X-ray bursts, are flashes on the surface of accreting neutron stars in low mass binary systems, recurring on a scale

of hours to days. First discovered in 1976 [5, 41], they are among the brightest and most common thermonuclear explosions with about 60 galactic bursting systems known today. For a review of X-ray bursts and their observables, see [60, 61, 78]. X-ray bursts provide an excellent probing tool of compact neutron stars and the properties of matter under such extreme conditions. System parameters such as mass accretion rate, accreted abundances of hydrogen, helium, and CNO metals strongly affect the bursts' observable parameters providing an avenue to constrain these parameters through observations if the nuclear reactions are understood [8].

X-ray bursts are powered by three mechanisms, the $3\text{-}\alpha$ -process, the αp -process, and hydrogen burning via the rp-process until peak temperatures up to 2 GK are reached [85, 97]. The thermal runaway lasts between 10 s up to 100 s. The rp-process dominates energy generation at late times and plays a significant role in determining the light curve tail of the burst. The nucleosynthesis via the rp-process at these high temperatures goes up to ^{56}Ni and beyond within the timescale of the bursts and reaches an end point at the Sn-Sb-Te cycle [84]. Beyond Fe, waiting-points created by long-lived β -decays at ^{64}Ge , ^{68}Se , ^{72}Kr , and ^{104}Sn can slow the process down and extend the energy release of the burst, leading to a duration of 100 - 300 s. These findings were based on one-zone model calculations [84] that include the full rp-process network. Subsequent one-dimensional multi-zone calculations performed with the full rp-process have confirmed previous studies and provided new insight on ignition conditions and hydrogen burning between bursts [99]. The ultimate test for these models remains direct comparisons to observations [25] which demands accurate nuclear physics input.

Most of the nuclei participating in the rp-process are unstable. In addition to proton capture rates, their nuclear masses and β -decay half-lives are among the important nuclear

physics pieces that are crucial to building an accurate model. The instability of the isotopes involved makes experiments challenging. Nevertheless, advances in radioactive beam facilities have led to experimental determinations of the β -decay half-lives and most of the masses. Measurements of proton capture rates on unstable nuclei are particularly challenging, leading to the dependence of stellar models on theoretical models to provide astrophysical rates for key reactions. Methods such as Hauser-Feshbach and shell model calculations are widely used [35, 45], however uncertainties can be a factor of 2 - 3 up to many orders of magnitude for rates that depend on a few isolated resonances [20, 50, 80]. Experimental efforts involving indirect methods [2, 7] are important when the radioactive beam in need is not yet available, when the resonances are too weak, or when the resonance energies are too uncertain. These methods can reduce uncertainties by providing information about the properties of the nuclei involved, but in many cases the uncertainties are still too large. To obtain sufficiently accurate reaction rates for rp-process models, direct measurement are required. Given that the majority of the isotopes involved are radioactive, such measurements necessitate the use of inverse kinematics. This technique is employed in recoil separators such as SECAR, and will be explained in detail in Section 1.3.2.

Several sensitivity studies have identified the reactions that have the most effect on the light curve of X-ray bursts and should therefore be the focus of direct experimental efforts [26, 28, 36, 37, 55, 75, 93, 99]. In these studies, reaction rates are varied individually within their large uncertainties, and the subsequent effects on the light curve and the composition are examined to identify critical reactions. The first study to use fully self-consistent one-zone and multi-zone 1D models of X-ray bursts [26] highlighted reactions that impact the burst light curve and the ashes composition the most. The majority of those reactions are (α, γ) and (p, γ) radiative capture reactions, emphasizing the importance and necessity

of addressing these uncertainties with direct measurements at radioactive beam facilities. Some of the high impact reactions common for one-zone and multi-zone models that had changes in rates large enough to affect the interpretation of observational data themselves include $^{15}\text{O}(\alpha,\gamma)^{19}\text{Ne}$, $^{59}\text{Cu}(\text{p},\gamma)^{60}\text{Zn}$, $^{61}\text{Ga}(\text{p},\gamma)^{62}\text{Ge}$, and $^{23}\text{Al}(\text{p},\gamma)^{24}\text{Si}$. SECAR represents a targeted approach to reduce the uncertainties and enable direct measurements of these rates and arrive at a better understanding of the underlying physics of X-ray bursts and ultimately, of neutron stars.

1.2.2 Radiative Capture Reactions in Novae

Classical novae are stellar explosions that occur in interacting binary systems where a compact white dwarf star accretes proton rich matter from a low-mass main sequence companion [11]. The proton rich matter accumulates on top of the white dwarf and is gradually compressed up to degenerate conditions, eventually leading to a thermonuclear runaway with temperatures not exceeding 0.4 GK. This phenomena is the second most common type of thermonuclear explosion in the galaxy after X-ray bursts, and is recurrent with a period of $10^4 - 10^5$ years [98]. Observational properties of novae include the light curve showing the luminosity versus time in optical light, infrared radiation to study dust formation, and spectra in optical, ultraviolet and infrared reflecting the abundances of chemical species in the ejecta.

In this hydrogen rich environment, the most important reactions involve protons due to the comparably small Coulomb barriers to overcome. The predominant nuclear reactions that contribute to the runaway are (p,γ) or (p,α) operating within the mass region of $A < 40$. The runaway is initiated by pp-chain fusion and also involves the hot CNO cycle. Later stages of the explosion are partially powered by proton capture reactions on neon

that is mixed in from the white dwarf in some novae, and by the decay of the resulting radioactive isotopes. The nuclear reaction pathway lies between the line of stable nuclei and the proton drip line and involves stable and unstable nuclei. Masses, β -decay half lives and reaction rates of such isotopes are thus crucial to modeling these outbursts. Comprehensive sensitivity studies have been carried out [49] and important radiative capture reactions have been identified.

Recent experimental measurements have focused on many of the isotopes that were shown to play a significant role in the outburst. The remaining gaps in knowledge are mainly due to inadequate beam intensities, leaving critical rates still uncertain such as $^{30}\text{P}(p,\gamma)^{31}\text{S}$ and $^{25}\text{Al}(p,\gamma)^{26}\text{Si}$. The former rate is critical for the production of elements between mass 30 and 40, and determines the Si isotopic ratios that have been observed in presolar meteorite grains with a nova origin [49, 53]. The latter is one of the remaining critical rates with a large uncertainty that affects the synthesis of the ^{26}Al γ emitter [44]. Constraining these rates would answer some long-standing questions regarding novae nucleosynthesis and the elemental abundances observed.

Given that the critical reactions relevant to novae are closer to stability than in X-ray bursts, and thanks to the recent experimental effort at stable and radioactive beam facilities, novae are on track to being the only stellar explosions with nucleosynthesis models fully backed by experimental data [54]. Due to the scarcity of intense radioactive beams in the past, most of the effort was directed to reactions involving stable nuclei. Only recently have direct measurements of reactions involving radioactive isotopes relevant to novae been enabled by recoil separators at facilities such as TRIUMF and Oak Ridge National Laboratory [3, 9, 31, 40]. With recent advancements at radioactive beam facilities bringing high intensity ion beams to nuclear astrophysics, the remaining rates in need of direct measure-

ments such as $^{30}\text{P}(p,\gamma)$ and $^{25}\text{Al}(p,\gamma)$ are within reach.

1.3 Direct Measurement of Radiative Capture Reactions

While indirect methods are essential for the identification of resonances and the determination of their spins, parities, and energies, direct methods directly determine the quantity needed to calculate the astrophysical cross sections and reaction rates at astrophysical energies. The direct measurement of capture reactions via inverse kinematics is currently in use or proposed at radioactive facilities worldwide. This section presents an overview of the inverse kinematics approach, delineates typical recoil separator designs and performance metrics, and introduces the recoil separators that pioneered this method as well as those currently available.

1.3.1 Experimental Studies

Measurements of radiative capture reactions come with several experimental complexities. The cross sections tend to be very small at typical astrophysical energies of 0.3 - 3 MeV/u, making their rates difficult to measure with currently available intensity beams and traditional techniques. Additionally, the involvement of many radioactive isotopes in important radiative capture reactions make normal kinematics difficult to use as heavy radioactive isotopes made into a target might decay quicker than an experiment can gather sufficient data. Another challenge is the difficulty to detect the γ -ray signature of the capture reactions with high sensitivity due to efficiency limitations and background, including background from the

decay of stray radioactive beam.

As high luminosity radioactive beams become available, inverse kinematics experimental techniques are the method of choice to directly measure capture reaction rates. In addition to reducing beam induced background, the method allows the study of astrophysical reactions involving short-lived isotopes that would not be possible otherwise. Devices such as recoil separators can enable these direct measurements. SECAR at FRIB will facilitate the direct measurements of the radiative capture reactions that answer many of the open questions regarding the physics behind accreting neutron stars, white dwarfs, and other explosive scenarios.

1.3.2 Inverse Kinematics

There are two methods to experimentally study nuclear reactions. One is using normal (forward) kinematics, the other is using inverse kinematics. They simply reflect the two possible choices of which particles are the projectiles and which are the target. Normal kinematics is a popular configuration when proton and α -particle beams are readily available and the target nucleus is stable, and can be easily manufactured into a suitable target. In this configuration, a lighter beam impinges on a heavy target, resulting in heavy recoils that stay mainly within the target while the lighter ejectiles pass through onto the detector system. In radiative capture reactions, the ejectile is the γ -ray emitted from the capture. For capture reactions on unstable nuclei with too short half-lives to form a target, an inverse kinematics configuration using a light target such as proton or helium with a radioactive beam impinging on such a gas target is the only choice. In the center of mass reference frame, the light particle is impinging onto the heavy nucleus against the beam direction. The main ejectile collected is the heavy recoil, and for radiative capture, the γ -ray can also

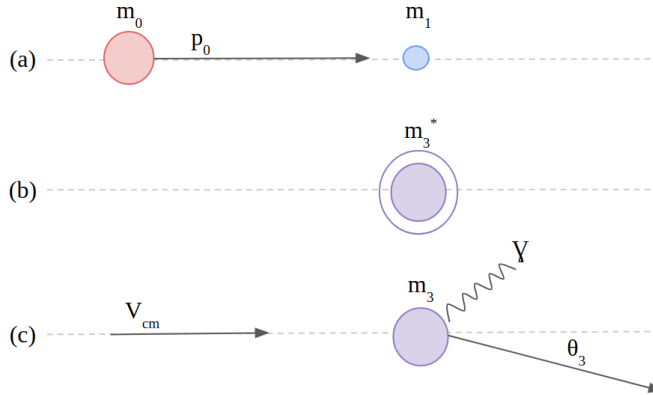


Figure 1.1: Simplified illustration of resonant radiative capture in the laboratory frame.

be detected in coincidence with the heavy recoils, reducing background in the measurement. Even for stable beams, an inverse kinematics approach can be beneficial when the isotope abundance is small, the target has high impurities, is difficult to fabricate, or is unstable under intense beams. Inverse kinematics with stable beams can also be used to increase sensitivity and reduce background, as recoil detection can produce a much cleaner signal, especially in coincidence with reaction γ -rays.

Taking a projectile with mass m_0 and momentum p_0 impinging on a target with mass m_1 at rest as shown in Figure 1.1 (a), a target nuclei captures a projectile nuclei and forms a nucleus with mass m_3 in an excited state (b). The recoil can be the compound nucleus in a resonant reaction, or the final de-excited state of a direct capture. An excited recoil decays via emission of additional γ -rays each at some angle with respect to the beam direction. The γ -rays carry away little momentum leaving the recoil with a momentum similar to the incident projectile but slightly changing the recoil angle. The recoil thus emerges from the target in a narrow cone centered on the beam direction with an opening angle that generally depends on the beam energy and the energies of the emitted γ -rays. Figure 1.1 (c) shows the case for a resonant capture with a single γ -ray emission with the recoil emerging at an

angle θ_3 from the beam axis. Angular straggling in the target and the angular divergence of the incoming beam can further broaden the angular distribution of the recoils. A recoil separator's purpose is to spatially separate these ions by mass with a high rejection rate for unreacted beam particles that would otherwise overwhelm detectors and make recoil detection impossible. The separator has to let through the full recoil cone, and ideally has to have full transmission for recoils of a selected charge state to avoid systematic uncertainties.

The angle of the recoils is maximized when a single photon is emitted to the ground state and is defined by the excitation energy of the compound nucleus state. Given a single photon emitted perpendicularly to the beam direction, the maximum lab angle of the recoil θ_{max} and the magnitude of the momentum spread of the recoils about their central momentum $\Delta p/p$ are given in the non-relativistic approximation [83] by

$$\frac{\Delta p}{p} = \tan(\theta_{max}) \approx \frac{E_{\gamma,max}}{p_0} \approx \frac{Q_m + E_{lab}}{\sqrt{2m_0 E_{lab}}} \approx \frac{Q_m + E}{\sqrt{2\frac{m_0}{m_1}(m_0 + m_1)E}} \quad (1.1)$$

where Q_m is the reaction Q-value, $E_{\gamma,max}$ is the maximum energy of the emitted γ -ray, m_0 is the projectile mass, m_1 is the target mass, and E is the center of mass energy. At energies typical for astrophysical studies, the beam velocities are typically low enough that relativistic effects can be neglected. Figure 1.2 shows the maximum recoil lab angle for several radiative capture reactions that are of astrophysical interest for X-ray bursts, novae and supernovae studies. Differentiating Equation 1.1 with respect to E , it is found that it has a minimum at $E = Q_m$. Moreover, the smaller the Q-value and the larger the ratio m_0/m_1 , the smaller the recoil cone, leading to smaller demands on recoil separator angular (and energy) acceptance requirements. Taking for example a separator that is able to measure α -capture on ^{15}O at $E_{\text{CM}} = 0.2$ MeV, an angular acceptance of at least ± 23 mrad is needed. In practice,

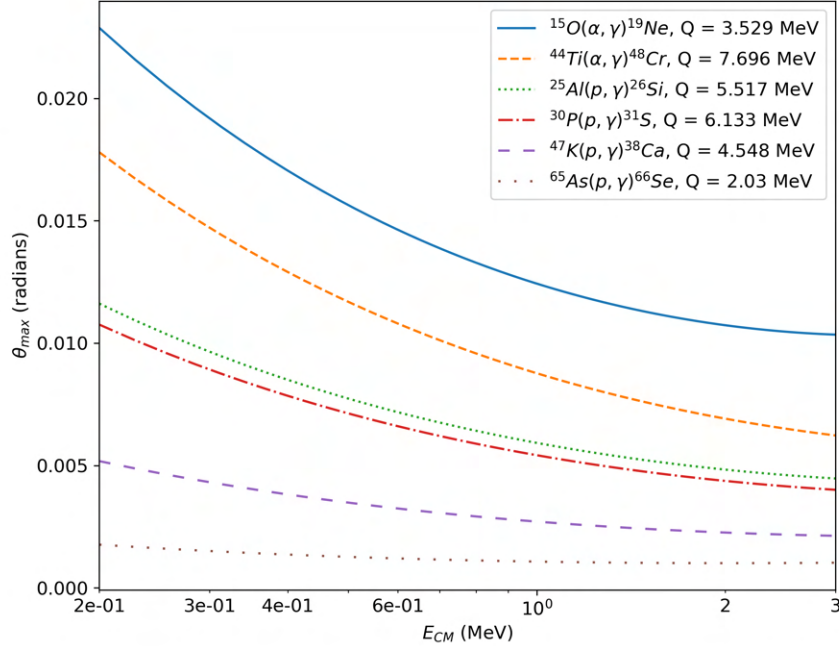


Figure 1.2: Maximum recoil half-angle in the laboratory frame as a function of the center of mass energy for a number of reactions of astrophysical interest.

the angular straggling in the target and the incoming beam angular divergence will broaden the recoil angular distribution and a slightly larger acceptance is needed. If more than one γ -ray is emitted, each photon is emitted in some direction resulting in a recoil angle less than θ_{max} . The resulting recoil angle distribution for the reaction then has a mean angle less than θ_{max} .

1.3.3 Recoil Separator Design Principles

A beam impinging on a gas target undergoes atomic charge exchange reactions and capture reactions. After the target, most of the beam emerges, together with a typically very low rate of reaction recoils, both species with some charge state and momentum distribution.

A recoil separator aims at separating the unreacted beam and transporting the recoils for a selected charge state to a detector station at the end of the beamline. When assessing

recoil separator performance, the beam suppression, defined as the ratio of the number of projectiles incident on the target to the number reaching the final detector station, is an important quantity. A high beam suppression allows for the utilization of more intense beams and offers more protection for sensitive detectors. Typical suppression needed for capture reactions is 10^{12} , and the highest reported for radiative capture surpassed 10^{14} at the 90% confidence level [90].

As seen in Section 1.3.2, a recoil separator has certain geometrical acceptance requirements to allow through the full recoil cone of reactions that are of interest. Moreover, the separator needs to accommodate the momentum and energy distributions of the recoils determined by the energies and properties of the reactions that the device aims to study. The design requirements then include angular, energy and momentum acceptances that are needed to directly measure those reaction rates. An ideal separator is able to transmit 100% of the recoils for a selected charge state within those specified acceptances to avoid systematic errors, while ensuring a high unreacted beam suppression.

To achieve an adequate amount of beam suppression, a recoil separator system combines a separator based on ion optical elements with one or more detectors systems. The separator itself serves to create a spacial separation between the unreacted beam particles and the recoils, and does so through a series of charge and mass separation stages. As both recoils and unreacted beam enter the separator with a charge state distribution, a single charge state needs to be selected in the separator. In SECAR, this charge selection stage is performed immediately after the target, preceding any mass selection, to reduce unreacted beam leaking due to scattering when hitting inner chamber surfaces downstream. Movable slits are employed at the charge focus to transmit one charge state and block the rest. Moreover, a mass separation stage with a mass dispersive focus is required to create separation

between the recoils and the unreacted beam of similar momentum. Slits are utilized at the mass focus as well to block the beam and transmit the recoils. In SECAR, a second mass separation stage is added to suppress any unreacted beam leaking through the first stage. Along the entire separator system, focusing elements such as magnetic quadrupoles are used to transmit the recoils and the beam and bring them to a focus.

Charge State Separation

The motion of a charged particle with charge Q in an external electric and magnetic field \mathbf{E} and \mathbf{B} , respectively, is given by the non-relativistic Lorentz force equation

$$\mathbf{F} = Q (\mathbf{E} + \mathbf{v} \times \mathbf{B}) \quad (1.2)$$

where v is the particle velocity. The magnetic rigidity of a charged particle, which quantifies how difficult it is to bend the particle and change its trajectory in a uniform magnetic field, is defined as

$$B\rho = \frac{p}{Q} \quad (1.3)$$

where ρ is the radius of the particle's circular trajectory, and p is the particle momentum. By fixing the momentum p , separation by charge Q can be attained for a given field B . Therefore creating momentum dispersion via magnetic dipole magnets at a focal plane where slits are installed along the separator facilitates the selection of one charge state of the recoils. However due to momentum conservation in a capture reaction, the recoil and the beam have similar momentum but different velocities, making magnetic rigidity dispersion no longer sufficient to separate all the beam from the recoils. Given the very large number of unreacted beam leaving the target mixed with the recoils, separation by velocity is therefore critical to suppress the beam with similar momentum and charge and achieve mass separation.

Mass Separation

A combination of magnetic and electric fields is necessary to achieve a mass dispersive plane. Similarly to the magnetic rigidity, the electric rigidity is defined using Equation 1.2 given a constant electric field E

$$E\rho = \frac{pv}{Q}. \quad (1.4)$$

Thus for a given charge state Q , electric dipoles bend according to kinetic energy. The mass dispersion can therefore be achieved by employing electric and magnetic bending dipole magnets in such a way to provide zero energy dispersion at one or more foci where slits are installed to separate out the recoils from the unreacted beam with a different mass. Electrostatic dipoles can be used to generate electric fields, or a device combining electric and magnetic dipoles, called a Wien filter (WF) or velocity filter, can be used instead. A WF is a device with magnetic and electric fields perpendicular to each other on the ion optical axis. The values of the fields are set in such a way to let particles with the selected velocity v_z equal to E_x/B_y pass through along the axis without deflection. This property is derived from Equation 1.2 when the force felt by a particle with velocity v is zero. The combination of magnetic fields and electric fields is necessary to achieve an achromatic (no energy dispersion) focus where slits are installed to separate out the recoils from the unreacted beam with a different mass.

Wien Filters

Several advantages come with the use of a WF instead of separate electric and magnetic bending dipole magnets. In a WF, the ratio of electric and magnetic fields selects the velocity, making it possible to operate with reduced field strengths to accommodate higher rigidities, or if less rejection is required for example. This offers flexibility in the ion optics that is

not possible in a system with separate magnetic and electric bending dipoles where the field strengths are fixed by the bending radii and recoil momentum. Another advantage is that WFs can achieve high separation of particles without any bend, while separate electric and magnetic bending dipoles require a higher bend for higher separation. It follows that beam can be transported through a WF with the device turned off (e.g. if in a multistage system only one mass separation stage is needed), while electric bending dipoles have to provide the appropriate electric fields from the beam to pass through. In SECAR, two WFs are employed in sequential mass separation stages to achieve a higher mass separation. In both WFs, the electric dipole is embedded in a magnetic dipole, resulting in a compact design. To achieve the desired mass separation with a single WF, it would have to be significantly larger in width and length. This poses multiple concerns with the space available in the experimental hall, and other technical difficulties such as requiring an increased high voltage on the electrodes. While both separate electric dipoles and WFs require high voltage conditioning, a disadvantage is introduced with WFs due to the magnetic field deflecting electrons emitted during conditioning. This can lead to a more challenging conditioning process. Moreover, a WF poses greater design problems. Careful shaping of both the electrodes and the magnet poles, ensuring that the field ratio E/B remains uniform, and matching the electric and magnetic fringe field regions are ways to minimize the design challenges that come with WFs.

Focusing Elements

To achieve a focus at locations where slits are used for separation, and to transport the beam through the system despite of its initial angular divergence as it exits the target, magnetic quadrupole lenses are utilized. Ion optical designs often set up quadrupoles in doublets or triplets to achieve a net focusing force in the horizontal and vertical direction.

Since a perfect focus is difficult to achieve with only quadrupoles, additional higher-order elements are needed. Quadrupoles can introduce spherical aberrations and coma aberrations where the beam spot may be sharp in the center but become increasingly blurred toward the edges. These can be corrected by insertion of hexapole and octupole magnets at defined locations based on the ion optical design.

An ion optical design forming a proper combination of all these optical elements to provide adequate mass separation is combined with recoils detectors at a final focal plane to count the recoils transported to the end of the separator. The detectors can also be used to identify and separate recoils from unsuppressed beam, e.g. by energy loss, energy, and time-of-flight measurements. Additionally, γ -ray detectors can be placed at the target to detect γ -ray emissions from the capture reactions in coincidence with the recoil counting to further suppress background. The final beam suppression of the system is a combination of the separator suppression from the mass separation and the suppression provided from the detector systems. A recoil separator is characterized by its beam suppression capability, its energy, angular and rigidity acceptances, as well as its mass resolving power, a concept that will be introduced in Chapter 3 where the ion optics of such a device is explained in more detail.

1.3.4 Previous Recoil Separators

In this section, an overview of early recoil separators and current separators at stable beam and radioactive beam facilities is presented with a focus on systems designed or re-purposed for studying reactions relevant to nuclear astrophysics. The different separators have unique designs in how electromagnetic elements are combined, and the choice of targets, γ -array detectors and focal plane detectors. Such choices are made based on the precision, and

the angular and energy acceptances required for the reactions planned for each scientific program. Although beam suppression reported varied with beam energies and conditions, the descriptions below offer a general comparison of the overall performance and achievements of the different systems and highlights the novel opportunities that SECAR will bring to the community as the first recoil separator to be optimized for high masses.

Caltech Recoil Separator

The concept of a recoil separator for astrophysical reaction rate measurements was first realized at the California Institute of Technology (Caltech) in the 1980's. The pioneering experiment by Kremer et al. [58] measuring the cross section of $^{12}\text{C}(\alpha, \gamma)^{16}\text{O}$ at low energies served as proof of concept of the inverse kinematics technique to reduce background by employing coincidences between γ -ray emissions and recoil particles. The effectiveness of a recoil separator for direct measurements at radioactive beam facilities was further explored a few years later by Smith et al. [91]. The system used a heavy ion beam with a windowless differentially pumped gas target, and utilized a quadrupole to focus the beam after the target. A WF served to separate the recoils with slits stopping the beam particles. A charge state was subsequently selected by a magnetic dipole, leading the recoils and remaining leaky beam particles into the focal plane detector system. An array of four large NaI scintillators was detecting γ -rays at the target in coincidence. Beam suppression with this system was shown to be up to 10^{10} .

ERNA at Bochum

The European Recoil separator for Nuclear Astrophysics (ERNA) was installed at the Bochum Dynamitron Tandem accelerator laboratory to measure low energy reactions with stable beams in inverse kinematics. It has been used to measure $^{12}\text{C}(\alpha, \gamma)^{16}\text{O}$ [29] and other astrophysically relevant reactions at low energies. ERNA was built using components from

the Caltech separator with additional quadrupoles and an extra WF. The separator uses a WF to create a mass separation, then selects a single charge state using a single magnetic dipole, followed by a second WF before transporting the recoils to the focal plane. It is combined with an extended gas target. The full system has shown beam suppression of 10^{10} - 10^{12} , surpassing the Caltech separator due to the early selection of a single charge state before the use of the second WF that is set up directly upstream of the focal plane [81].

ARES at Louvain-la-Neuve

The Astrophysics Recoil Separator (ARES) was designed for proton and α -capture measurements in inverse kinematics at the Cyclotron Research Center at Louvain-la-Neuve in Belgium. It utilized a CH_2 plastic foil hydrogen target instead of a gas target, and followed previous improvements shown in ERNA by creating a charge separation first using a magnetic dipole then using a WF to separate the recoils by velocity. The facility's beam properties included a large emittance that prevented the quantification of the separator's acceptance [1]. The system was used to measure $^{19}\text{F}(\text{p}, \gamma)^{20}\text{Ne}$ in inverse kinematics and resulted in a beam suppression of 10^7 due to the use of a foil target and to the beam quality [22]. Another measurement was attempted, of a $^{19}\text{Ne}(\text{p}, \gamma)^{20}\text{Na}$ resonance at 448 keV, however no recoils were detected and an upper limit on the resonance was established [21]. No further ARES measurements were done.

DRS at ORNL

The Daresbury Recoil Separator (DRS), initially designed for measurements of fusion evaporation reactions in nuclear structure research, was re-purposed to study capture reactions relevant to the explosive hot CNO cycles upon moving from the UK to Oak Ridge National Lab (ORNL) and the Holifield Radioactive Ion Beam Facility. The system followed the Caltech design with a supplemental WF added before the charge selection stage. The

separator had a single dipole magnet, three quadrupole triplets, and two magnetic hexapoles to provide higher-order corrections to the ion optics. It employed a windowless hydrogen gas target, and the focal plane detectors included position detection and an ionization chamber for recoil identification. The DRS was tested using stable beams and measured $^{17}\text{F}(p, \gamma)^{18}\text{Ne}$ and $^7\text{Be}(p, \gamma)^8\text{B}$ [4, 15]. The beam suppression was of order $10^9 - 10^{11}$.

DRAGON at TRIUMF

The Detector for Recoils And Gammas Of Nuclear reactions (DRAGON) was designed to study proton and α -capture reactions relevant to classical novae and type-I X-ray bursts using radioactive beams at the ISAC facility at TRIUMF. The device uses two magnetic dipoles and two electrostatic dipoles for its momentum and energy selection, with an extended windowless proton or He gas target. The system is optimized for isotopes up to mass 30. The design was chosen to accommodate the measurement of $^{15}\text{O}(\alpha, \gamma)^{19}\text{Ne}$ at $E_{\text{CM}} = 0.5$ MeV which requires a minimum acceptance of ~ 16 mrad (see Figure 1.2). DRAGON was thus designed with a moderately large angular acceptance of ± 21 mrad to account for a slightly broader angular distribution and with an energy acceptance of $\pm 4\%$ [47]. The first experiment was a direct measurement of the $^{21}\text{Na}(p, \gamma)^{22}\text{Mg}$ reaction [31, 34]. The suppression of the separator alone is on the order $10^9 - 10^{13}$ [90]. A γ -array comprised of bismuth germanate (BGO) crystals coupled with the recoil detection in coincidence increases the suppression by up to 3 orders of magnitude. DRAGON has been successfully measuring reactions with stable and radioactive beam, including high mass measurements such as $^{58}\text{Ni}(p, \gamma)^{59}\text{Cr}$ demonstrating its capabilities beyond its initial design limits [89].

St. George at the University of Notre Dame

The Strong Gradient Electromagnetic Online Recoil separator for capture Gamma-ray Experiments (St. George) is a recoil separator at the Institute for Structure and Nuclear

Astrophysics at the University of Notre Dame designed for the study of astrophysical low energy (α , γ) reactions for stable beams with mass up to $A = 40$ [23]. The separator has design acceptance values of ± 40 mrad in angle and $\pm 7.5\%$ in energy [69], and consists of six dipole magnets, eleven quadrupole magnets, and one WF. It utilizes the HIPPO (High-Pressure Point-like target) supersonic gas jet target [57]. The system was designed to provide a beam suppression of at least 10^{15} . A first detection of ^{18}F recoils from the $^{14}\text{N}(\alpha, \gamma)^{18}\text{F}$ was recently made with the St. George separator [72].

1.4 SECAR at FRIB and NSCL

SECAR is optimized for proton- and α -capture reactions for explosive nucleosynthesis using radioactive beams up $A = 65$. The device's design is based on the St. George separator with an additional Wien filter [6]. The JENSA gas jet target [17] is used with SECAR combined with an array of BGO crystals for γ -ray coincidence measurements with focal plane detectors that include time-of-flight, silicon and ionization chamber detectors. An additional extended proton or He gas windowless gas target will be available when resonance energies are not precisely known. SECAR will operate in the 0.2 - 3 MeV center of mass energy range and is designed to have an energy acceptance of $\pm 3.1\%$ and an angular acceptance of ± 25 mrad to accommodate for large recoil cones as seen in the case of $^{15}\text{O}(\alpha, \gamma)^{19}\text{Ne}$ (Figure 1.2). It is designed to provide a separator beam suppression of 10^{13} with an additional 10^4 contribution from the recoil detector system.

1.5 Machine Learning for Tuning Optimization

To achieve precision measurements, SECAR creates separation between unreacted beam and recoil particle of different mass but similar momentum by bringing the latter to a focus in two mass-dispersed planes along the separator. The separation goals require a carefully tuned recoil beam that is centered along the separator's ion optical axis, and finely tuned quadrupole fields to maximize the mass resolution and unreacted beam suppression of the device. This is achieved by tuning and establishing precise beam optics of a pilot beam prior to scaling to the recoil rigidity settings.

As the pilot beam is transported along the accelerator facility to the recoil separator, beam parameters such as energy spread, angular deviation, and size of the beam impinging on the target can be adjusted. Precise beam characteristics need to be achieved to fulfill the initial conditions required to ensure a centered and focused beam at the target. Obtaining a centered beam (< 1 mrad deviation from the central axis) has proven to be difficult and time consuming, as is discussed in detail in Chapter 5. Additionally within SECAR, quadrupole settings need to be tuned to obtain an optimized separation at the mass-dispersive plane thereby maximizing SECAR's performance. The process of manual adjustments and iterations to achieve such beam properties can significantly increase the device's setup and tuning time. Tasks such as visual checks of tune quality can be operator dependent, introducing subjectivity and bias to the process and leaving the device below optimal performance and in a possibly irreproducible state. A more robust solution is achieved with an automated tune optimizer that enhances reproducibility, ensures objectivity when assessing tune quality, and operates with an efficiency that surpasses the speed of manual tuning when searching for the optimal parameters to achieve SECAR performance targets for each experiment.

Machine learning model-dependent optimization methods have been successfully applied in other facilities to automate the tuning and controls of complex accelerators, for example at the Linac Coherent Light Source free-electron laser at SLAC to tune quadrupole settings [30, 67] and at the Central Laser Facility to create the first autonomous laser wakefield accelerator [87]. The use of Bayesian optimization [13, 86] in the tuning of a complex beamline is in some cases motivated by the assumption that the function f being minimized or maximized (e.g. beam size or transmission as a function of machine settings) is expensive to evaluate due to computational limits of beam simulation codes, or due to the time consuming task of operator-dependent machine adjustments until a suitable tune is found or until the changes take effect. In the case of SECAR, beam physics simulations incorporating the accelerator beamline upstream cannot be expected to have the required accuracy to provide an optimized experimental system, and manually tuning the beam to achieve precise beam properties has proven to be time consuming and unreliable. Given the high dimensionality of the system, a robust optimization of the experimental system is needed to validate and improve on the theoretical tune parameters obtained from beam simulations. With a proper model of the beam response in SECAR to changes in beamline parameters (magnet settings in SECAR and upstream), a Bayesian approach presents a good choice for addressing these issues while decreasing the time spent tuning and providing reproducible results.

In this work, a first application of a Bayesian optimization with a Gaussian process model [79] to the online beam tuning and ion optics optimization of a nuclear astrophysics recoil separator is reported. The stringent requirements defined as the optimal beam conditions for SECAR operation are guided by the ion optical design discussed in Chapter 3. Manual and Bayesian tuning methods are presented in detail in Chapter 5 and the ML algorithm's ability to achieve those requirements while improving on traditional methods is examined.

Chapter 2

Experimental Determination of Astrophysical Stellar Rates

2.1 Stellar Reaction Rates

In astrophysical models of stellar environments, one needs to provide the rate r of a nuclear reaction between two particles

$$r = \frac{N_t N_p v \sigma(v)}{(1 + \delta_{tp})}, \quad (2.1)$$

where N_t and N_p are the number densities of the target (t) and the projectile (p) particles, respectively, v is the relative velocity of the two particles, $\sigma(v)$ is the nuclear cross section, and δ_{tp} is the Kronecker symbol. This rate represents the number of reactions per second per volume of stellar plasma. When the plasma is at thermodynamic equilibrium, the relative velocity v is not constant, rather there is a broad distribution of relative velocities. It can be shown that the relative velocity between two particles in stellar plasma can be generally described by the Maxwell-Boltzmann formalism [19, 48], and its probability distribution for a certain temperature T can be written as

$$P(v)dv = \left(\frac{\mu_{tp}}{2\pi k_b T}\right)^{3/2} e^{-\mu_{tp} v^2 / (2k_b T)} 4\pi v^2 dv, \quad (2.2)$$

where μ_{tp} is the reduced mass, k_b is the Boltzmann constant, and T is the temperature. Folding the cross section with the velocity distribution of the reacting particles and generalizing, one obtains

$$r = \frac{N_t N_p \langle \sigma v \rangle}{(1 + \delta_{tp})} \quad (2.3)$$

with

$$\langle \sigma v \rangle = \int_0^\infty P(v) v \sigma(v) dv. \quad (2.4)$$

With $E = \mu_{tp} v^2/2$ and $dE = \mu_{tp} v dv$, the velocity distribution can be written as an energy distribution

$$P(E) dE = \frac{2}{\sqrt{\pi} (k_b T)^{3/2}} \sqrt{E} e^{-E/k_b T} dE. \quad (2.5)$$

The broad energy distribution in stellar plasma plays into the reaction rate by introducing an energy-temperature dependence term. The reaction rate in stellar environments is then defined in terms of the energy dependent cross section as follows

$$\langle \sigma v \rangle = \sqrt{\frac{8}{\pi \mu_{tp}}} \frac{1}{(k_b T)^{3/2}} \int_0^\infty E \sigma(E) e^{-E/k_b T} dE. \quad (2.6)$$

The reaction rate describes the number of reactions within a given volume per unit time in terms of the cross section $\sigma(E)$. As charged particles are interacting, this cross section drops off by orders of magnitude as the energy decreases due to the repulsion from the Coulomb barrier. Describing the cross section only in terms of its energy-dependent component and removing the trivial contribution from the Coulomb repulsion, the astrophysical S-factor

$S(E)$ can be defined as

$$\sigma(E) \equiv \frac{1}{E} e^{-2\pi\eta} S(E), \quad (2.7)$$

with the Sommerfeld parameter η defined as

$$\eta = \frac{Z_p Z_t e^2}{\hbar} \sqrt{\frac{\mu_{tp}}{2E}}, \quad (2.8)$$

where Z_t and Z_p as the charge states of the interacting particles. The Gamow factor $e^{-2\pi\eta}$ is an approximation for the s-wave transmission probability at energies below the height of the Coulomb barrier. Consequently the S-factor is smooth-varying and has a much reduced energy dependence compared to the cross section. To obtain the reaction rate, one must experimentally obtain $S(E)$, and therefore $\sigma(E)$, over the relevant energy range defined by the temperature in stellar interiors.

The reaction rate is most sensitive to the cross section at energies that are within the Gamow energy distribution. This energy distribution at a certain temperature T can be approximated by a Gaussian peak, with the peak central energy, the Gamow energy, given by

$$E_{Gamow} = \left[\left(\frac{\pi}{\hbar} \right)^2 (Z_t Z_p e^2)^2 \left(\frac{\mu_{tp}}{2} \right) (k_b T)^2 \right]^{1/3}, \quad (2.9)$$

and Gamow peak width, called the Gamow window, given by

$$\Delta_{Gamow} = \frac{4}{\sqrt{3}} \sqrt{E_{Gamow} k_b T}. \quad (2.10)$$

Figure 2.1 illustrates the Gamow window for an arbitrary reaction. For non-resonant reactions, the direct capture reaction rate can be obtained by extrapolation of the experimentally

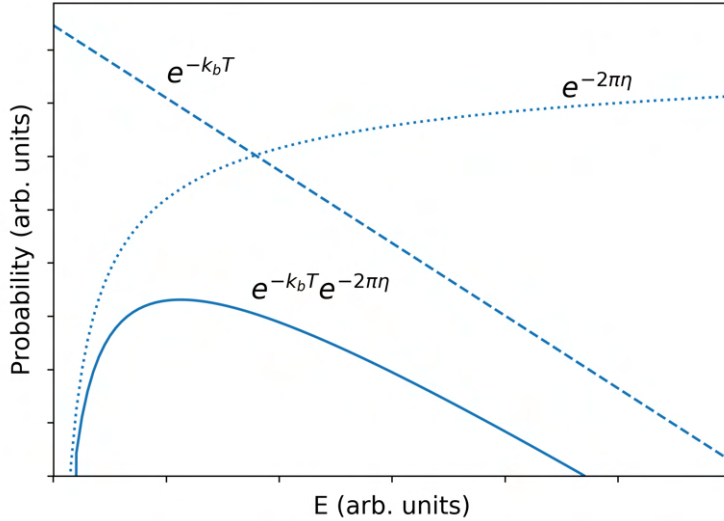


Figure 2.1: Maxwell-Boltzmann factor (dashed line) and Gamow factor (dotted line) versus energy for an arbitrary temperature T . The product $e^{-k_b T} e^{-2\pi\eta}$, representing the Gamow peak, is shown with the solid line.

determined S-factor $S(E)$ to lower energy ranges guided by the Gamow window.

The S-factor, and therefore the cross section, typically have contributions from narrow and broad resonances and non-resonant reactions. Resonances can dominate the astrophysical reaction rate due to their higher cross section even when the resonance energy falls outside of the Gamow window. Isolated and narrow resonances, defined in more detail in Section 2.2 are the focus of this work. The reaction rate can be simplified when narrow resonant contributions dominate, and can be obtained by determining the experimental yield and consequently, the strength of the resonance, as is detailed in the following sections.

2.2 Narrow Resonances

In explosive astrophysical sites, reaction rates are often dominated by resonant contributions.

When two nuclei undergo a resonant capture reaction, the compound nucleus is formed at

a specific excitation energy that is the sum of the beam energy and reaction Q-value Q_m . If this energy matches the energy of an excited state with excitation energy E_x within its energy width, the cross section can be significantly enhanced. This resonant enhancement occurs when

$$E_x \sim E_{cm} + Q_m \quad (2.11)$$

where Q_m is the mass excess and E_{cm} is the relative energy, which can be written as the resonance energy E_R . An isolated resonance implies a small enough level density in the compound nucleus to avoid significant overlap between resonances. A narrow resonance is defined as a resonance whose width is approximately constant over the total resonance width. The single-level Breit-Wigner formalism can be used to describe with a semi-classical approach the resonant behavior between two particles [10], and the cross section for a given isolated resonance can be expressed as [48]

$$\sigma_{BW}(E) = \frac{\lambda^2}{4\pi} \frac{\Gamma_{in}\Gamma_{out}}{(E_R - E)^2 + \Gamma^2/4} \omega \quad (2.12)$$

where the Broglie wavelength is $\lambda = 2\pi\hbar/\sqrt{2\mu_{tp}E}$. The second term is dependent on the partial widths of the entrance Γ_{in} and exit Γ_{out} channels and gives the cross section its Lorentzian shape with a FWHM of the total width of the resonance Γ and a maximum at E_R . The statistical factor ω accounts for the number of possible states in the compound nucleus compared to the number of states in the entrance channel. This factor can be expressed as

$$\omega = \frac{2J + 1}{(2J_p + 1)(2J_t + 1)} (1 + \delta_{p,t}), \quad (2.13)$$

where J_p and J_t are the incoming spins of the projectile and target, respectively, and J is the angular momentum of the excited state E_x . An additional term containing the Kronecker delta is included to avoid the double counting of identical particles in the entrance channel. Therefore the probability of finding the compound nucleus in a state E_x with a specific J out of $2J+1$ possibilities and finding the projectile and target in specific J_p and J_t out of all the possibilities allowed in the entrance channel is given by this spin statistical factor ω .

Quantum mechanical selection rules govern the the resonant behavior for different channels. The spin and parity of the nuclear states allowed are determined by the selection rules involving the spin and angular momentum

$$|\ell_p - J_p - J_t| \leq J \leq |\ell_p + J_p + J_t| \quad (2.14)$$

and the parity

$$\pi(J) = \pi(J_p)\pi(J_t)(-1)^{\ell_p} \quad (2.15)$$

where ℓ_p is the orbital angular momentum of the projectile and $\pi(J)$, $\pi(J_p)$, and $\pi(J_t)$ are the parities of the resonant state, the projectile, and the target, respectively. In the single-level Breit-Wigner formalism, it is assumed that the resonance levels of a given angular momentum J and parity $\pi(J)$ are widely spaced compared to their total widths.

In explosive hydrogen burning, proton- and α -capture reactions are often dominated by narrow resonances. It is assumed that for a sufficiently narrow resonance, the Maxwell-Boltzmann factor $e^{-E/kT}$ and the partial widths of the entrance and exit channels Γ_{in} and Γ_{out} are approximately constant over the total width of the resonance Γ . Taking these quantities as their constant values at the resonance energy E_R , the resulting integral over the cross section can then be carried out analytically to get the astrophysical reaction rate

and one obtains for a single narrow resonance

$$\begin{aligned}
\langle \sigma v \rangle &= \frac{\sqrt{2\pi}\hbar^2}{(\mu_{tp}k_bT)^{3/2}} \omega \int_0^\infty \frac{\Gamma_{in}\Gamma_{out}}{(E_R - E)^2 + \Gamma^2/4} e^{-E/k_bT} dE \\
&= \frac{\sqrt{2\pi}\hbar^2}{(\mu_{tp}k_bT)^{3/2}} e^{-E_R/k_bT} \omega 2\pi \frac{\Gamma_{in}\Gamma_{out}}{\Gamma} \\
&= \left(\frac{2\pi}{\mu_{tp}k_bT} \right)^{3/2} \hbar^2 e^{-E_R/k_bT} \omega \gamma.
\end{aligned} \tag{2.16}$$

The resonance strength is defined as

$$\omega \gamma \equiv \omega \frac{\Gamma_{in}\Gamma_{out}}{\Gamma}. \tag{2.17}$$

It can be seen from Equation 2.16 that once the resonance strength is known, the astrophysical reaction rate can be determined. If several narrow and isolated resonances contribute to the cross section, Equation 2.16 can be modified to incoherently sum over the individual states with different resonance energies and strengths.

2.3 Narrow Resonance Yields

The astrophysical thermonuclear reaction rate from narrow resonances is solely determined by the resonance strengths. The resonance strength of an individual resonance can be directly determined with a single experimental measurement using a target that is thick enough to allow for an energy loss that is much greater than the width of the resonance, while still being low enough to avoid contributions from any lower lying resonances. Using this method, the experimentally determined yield Y_{exp} can be directly related to the resonance strength. The yield is defined as the ratio of the total number of nuclear reactions that occurred \mathcal{N}_r

and the total number of incident beam particles \mathcal{N}_p ,

$$Y_{exp} \equiv \frac{\mathcal{N}_r}{\mathcal{N}_p}. \quad (2.18)$$

To relate this yield to the cross section, two quantities need to be defined. The stopping power describes the energy loss dE of the beam per distance dx travelled in the target per target nucleus

$$\epsilon(E) \equiv -\frac{1}{N} \frac{dE}{dx} \quad (2.19)$$

where N is the number density of the target and is related to the concentration of the target nuclei by

$$n \equiv Nd = \frac{\mathcal{N}_t}{A}. \quad (2.20)$$

Here \mathcal{N}_t denotes the total number of target nuclei in atoms per unit volume, d is the target thickness in units of length, and n is the number target nuclei per unit area. The stopping power is in units of eV cm²/atom, and all quantities are assumed to be determined in the center of mass system.

Consider a beam of energy E_0 is incident on a target that can be divided into slices of thickness Δx_i . The energy lost by the beam in each slice is then ΔE_i and is assumed to be small. The cross section σ_i and the stopping power ϵ_i are then taken to be constant over Δx_i . The partial yield over Δx_i can then be written as

$$\Delta Y_i = \sigma_i N_i \Delta x_i. \quad (2.21)$$

Integrating over the entire target and using the stopping power definition from Equation

2.19, the total yield is expressed as

$$Y(E_0) = \int_{E_0 - \Delta E}^{E_0} \frac{\sigma(E)}{\epsilon(E)} dE \quad (2.22)$$

where ΔE is the total energy loss in the target. For narrow resonances, the Breit-Wigner resonance σ , the stopping power ϵ , the de Broglie wavelength λ , and the partial widths Γ_i are all assumed to be independent of energy and therefore constant over the resonance width. Substituting Equation 2.12 for the cross section in Equation 2.22, taking the constant terms out and integrating, an expression for the yield for a narrow isolated resonance is obtained

$$\begin{aligned} Y(E_0) &= \int_{E_0 - \Delta E}^{E_0} \frac{1}{\epsilon(E)} \frac{\lambda^2}{4\pi} \omega \frac{\Gamma_{in}\Gamma_{out}}{(E_R - E)^2 + \Gamma^2/4} dE \\ &= \frac{\lambda_R^2}{2\pi} \frac{\omega\gamma}{\epsilon_R} \frac{\Gamma}{2} \int_{E_0 - \Delta E}^{E_0} \frac{dE}{(E_R - E)^2 + \Gamma^2/4} \\ &= \frac{\lambda_R^2}{2\pi} \frac{\omega\gamma}{\epsilon_R} \left[\text{atan}\left(\frac{E_0 - E_R}{\Gamma/2}\right) - \text{atan}\left(\frac{E_0 - E_R - \Delta E}{\Gamma/2}\right) \right]. \end{aligned} \quad (2.23)$$

The quantities λ_R and ϵ_R denote the de Broglie wavelength and the stopping power at the resonance energy E_R , respectively. From this expression, it can be deduced [48] that the value of the maximum of the yield is

$$Y_{max} = \frac{\lambda_R^2}{\pi} \frac{\omega\gamma}{\epsilon_R} \text{atan}\left(\frac{\Delta E}{\Gamma}\right) \quad (2.24)$$

and the FWHM of the resonance yield curve is

$$FWHM = \sqrt{\Gamma^2 + \Delta E^2}. \quad (2.25)$$

The beam energy at the maximum yield $E_{0,max}$ and at one half of the maximum yield $E_{0,50\%}$ are

$$E_{0,max} = E_R + \frac{\Delta E}{2} \quad (2.26)$$

and

$$E_{0,50\%} = E_R + \frac{\Delta E}{2} \pm \frac{1}{2} \sqrt{\Gamma^2 + \Delta E^2}. \quad (2.27)$$

For a thin target where $\Delta E \ll \Gamma$, the shape of the yield curve is Lorentzian following the cross section, and the maximum is located approximately at the resonance energy $E_{0,max} \sim E_R$ and the FWHM $\approx \Gamma$. If the target thickness is much larger than the total resonance width, $\Delta E \gg \Gamma$, the yield curve takes on an atan function shape as the atan term dominates. A flat top is seen where the energy is $E_{0,max} = E_R + \Delta E/2$ and the FWHM $\approx \Delta E$. As ΔE increases, Y_{max} and the FWHM increase as the cross section is integrated over a larger region. For an infinitely thick target where $\Delta E \rightarrow \infty$, the atan term in Equation 2.24 is equal to $\pi/2$, and the beam energy at 50% yield is then simply equal to the resonance energy E_R .

For a thick target, the energy loss ΔE will be much greater than the width Γ of the narrow resonance, and the FWHM of the yield curve will simply be equivalent to ΔE , namely the width of the target in energy units. The thicker the target, the closer the yield becomes that of an infinitely thick target. For instance, a target thickness that is equal to the total resonance width $\Delta E/\Gamma = 1$ reaches 50% of the maximum yield of an infinitely thick target and $\text{FWHM}/\Delta \approx 0.5$. Increasing that thickness to 10 times larger than the total resonance width $\Delta E/\Gamma = 10$ brings it up to 94% with a $\text{FWHM} \approx \Delta E$ within 0.5% [48].

In addition to the target thickness, the beam energy spread and straggling can influence the general shape of the resonance yield curve [48]. To take these effects into account, a

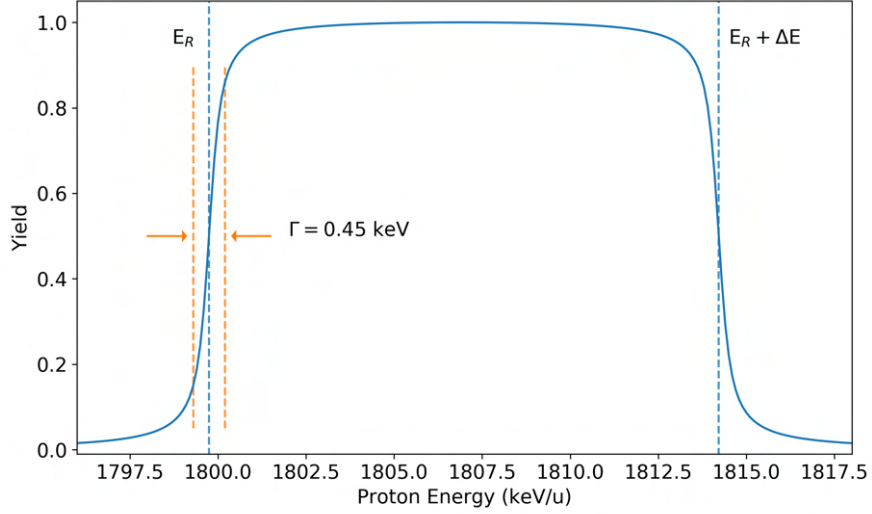


Figure 2.2: Yield curve normalized to Y_{max} for a thick target based on Equation 2.29 with a small beam energy spread $\delta = 0.005\%$.

Gaussian term of the form

$$g(E - E_0) = \frac{1}{\sqrt{2\pi}\delta} e^{-\frac{(E-E_0)^2}{2\delta^2}} \quad (2.28)$$

where E_0 is the mean energy of the incoming beam and δ is the beam energy spread is defined. It follows that the final form of the yield over the entire target is

$$Y(E_0) = \frac{\lambda_R^2}{2\pi} \frac{\omega\gamma}{\epsilon_R} \int_0^\infty \left[\text{atan}\left(\frac{E - E_R}{\Gamma/2}\right) - \text{atan}\left(\frac{E - E_R - \Delta E}{\Gamma/2}\right) \right] g(E - E_0) dE. \quad (2.29)$$

Figure 2.2 shows a typical yield curve for a target that is sufficiently thick to include the narrow resonance. The maximum yield is determined from differentiating Equation 2.29 and can be directly related to the resonance strength. For an infinitely thick target, it is no longer affected by the total resonance width and matches Equation 2.24 with the atan term

equal to $\pi/2$:

$$Y_{max} = \frac{\lambda_R^2}{2} \frac{\omega\gamma}{\epsilon_R}. \quad (2.30)$$

Therefore, a single measurement of the yield at an energy within the plateau region of the yield curve allows the determination of the resonance strength and therefore the determination of the astrophysical reaction rate contribution of the resonance.

Given a direct measurement, e.g. from a recoil separator, the total experimental yield is given by

$$Y_{exp} = \frac{\mathcal{N}_r}{\mathcal{N}_p} = \frac{\mathcal{N}}{\mathcal{N}_p \eta \nu \tau} \quad (2.31)$$

where \mathcal{N} is the total number of detected recoils, η is the detection efficiency, ν is the selected recoil charge state fraction for transmission, and τ is the transmission efficiency. For γ -coincidence detection, the γ -detection efficiency will depend on γ -ray branching and angular distributions. All measurements of resonance strengths require knowledge of the number of beam particles incident on the target, N_p . This quantity is typically determined by measuring and integrating the incoming ion beam current continuously when no significant losses are expected at the target as such

$$\mathcal{N}_p = \int \frac{I}{Qe} dt, \quad (2.32)$$

where I is the electrical beam current (e.g. as measured by a Faraday cup), Q is the charge state of the beam ions delivered by the accelerator facility, and e is the elementary charge. In inverse kinematics, as recoil separators are designed to transmit only recoils, elastic scattering of beam ions on the gas target can be used to achieve beam normalization. Elastic scattering monitors in the target chamber are planned for SECAR. In this case, the normalization factor

can be determined by taking the ratio of the beam current reading upstream of the target chamber and the number of elastically scattered target particles detected. To measure the charge state fraction transmitted in the recoil separator, a comparison of the absolute beam current readings between a Faraday cup upstream of the target and a cup located just after the charge selection in the recoil separator must be made.

Using the maximum yield Y_{max} given in Equation 2.30 for an infinitely thick target, the resonance strength is calculated as

$$\omega\gamma_{exp} = \frac{2\epsilon_R}{\lambda_R^2} \frac{\mathcal{N}_{max}}{\mathcal{N}_p\eta v\tau}. \quad (2.33)$$

Chapter 3

SECAR Design and Experimental Setup

3.1 The NSCL and ReA3 Facility

The NSCL, located on MSU's campus, is a facility dedicated to the production of rare isotope beams via projectile fragmentation to investigate the properties of nuclei and nuclear reactions. Stable beams are accelerated to 80 - 160 MeV/u by two coupled superconducting cyclotrons (K500 and K1200), also known as the Coupled Cyclotron Facility (CCF), and fragmented on a solid target. The resulting cocktail of rare isotopes gets separated in the A1900 achromatic fragment separator, and the fragments of interest are delivered to any of the multiple experimental halls for nuclear physics research. While these fast rare isotope beams can be used to investigate nuclear structure and some reaction properties, the study of reactions relevant to astrophysical scenarios require low energy beams. To achieve that, the fast beams are stopped in a He gas cell, re-extracted, and transported to the electron beam ion trap (EBIT) for charge state breeding. Subsequently, the charged ions are extracted from the breeder and transported into an achromatic charge state (Q/A) separator where the desired charge state is selected before the beam enters the accelerator section. The re-accelerator includes a room temperature RFQ and a superconducting LINAC. The combination of the gas-stopper cell and the re-accelerator (ReA3) is unique to the NSCL

and provides energies ranging from 300 keV/u to up to 6 MeV/u depending on the charge-to-mass ratio. The ReA3 facility includes beam distribution lines that consist of two high resolution achromatic sections with slit systems that can be used to limit the beam energy spread. The beam can be transported from the accelerator to one of three target stations in the ReA3 experimental hall, one of which is a dedicated SECAR experimental line.

The CCF was shut down on November 15 2020 preceding the reconfiguration of the A1900 in anticipation of the completion of FRIB. In this work, only stable beams produced at the ReA3 facility were utilized for the purpose of the commissioning of SECAR.

3.2 The FRIB Facility

FRIB, currently under construction on MSU campus, will be the world's leading rare isotope and low energy nuclear science facility when it becomes operational in 2022. FRIB will replace the CCF facility with a new 200 MeV/u LINAC, significantly increasing the variety and intensity of rare isotope beams available. The short-lived species are produced by fragmentation in a new high power target station, separated in a new fragment separator, and then fed into the existing NSCL beam transport system, including the existing gas stopper and ReA3 re-accelerator.

The beam species anticipated at FRIB overlap well with the proton-rich unstable nuclei that play a major role in thermonuclear runaways occurring at astrophysical sites such as novae and X-ray bursts. Once the facility is completed, the ReA3 facility will stop and re-accelerate the fast beams produced by FRIB and transport them to the different end-stations in the ReA3 Hall for low energy nuclear structure and reaction studies, including scientific experiments with SECAR. SECAR was designed to utilize the high intensity radioactive

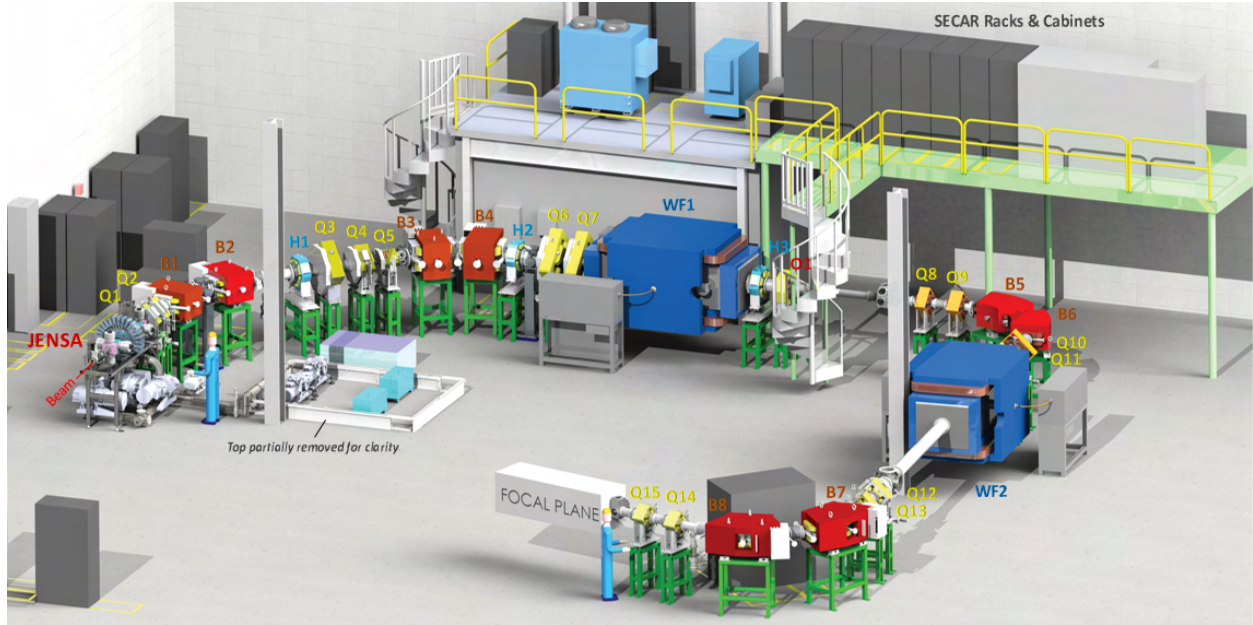


Figure 3.1: The SECAR recoil separator layout in the ReA3 Hall at MSU. The beam enters the hall from the middle left into the JENSA gas jet target system, and the capture reaction recoils along with the unreacted projectiles enter the first section in SECAR that selects a single charge state. Two subsequent sections each including a velocity filter (WF1, WF2) serve to reject the remaining projectiles, and the final cleanup section features a final pair of dipoles before particles enter the focal plane detection system.

beams available at ReA3 and FRIB by providing direct measurements of capture reactions that such isotopes undergo at low astrophysical energies.

3.3 The SECAR Design

SECAR was designed to simultaneously achieve high transmission of capture reaction recoils and a high rejection of unreacted projectiles. The design consists of eight dipole magnets, 15 quadrupole magnets, three hexapole magnets, one octupole magnet and two WFs. The complete layout of the system in the ReA3 Hall is shown in Figure 3.1, and Figures 3.2 and 3.3 show the beamline after installation. The ion optical design consists of four sections with a focal plane at the end of each. The sections are described below.



Figure 3.2: SECAR in the ReA3 Hall showing B1 up to Hex3.



Figure 3.3: SECAR in the ReA3 Hall showing B5 up to the final focal plane.

Section 1: Charge State Selection

This section starts at the target up to the first focal plane (FP1) that is located immediately downstream of Q5. The beam projectiles arriving at the target have a single charge state. As the beam particles pass through the gaseous target, charge changing processes such as ionization, excitation, and radiative and non-radiative electron capture take place and cause multiple charge states to be produced. The variation of charge state fractions versus charge state is called the charge state distribution of the beam. In this section, a single charge state (the most abundant) is selected for the recoils and unreacted beam. The quadrupoles in the first section of SECAR serve to refocus the diverging trajectories of particles exiting the target back towards the optical axis of the SECAR beamline. The first two dipoles B1 and B2 provide the momentum dispersion required to select a charge state. Separation by magnetic rigidity (refer to Equation 6.1) using the magnetic field generated by B1 and B2 leads to the recoils and beam of different charge states to be focused at different positions at FP1. The dipoles are used to center the desired charge state on the magnetic axis, and the slits at FP1 are moved to create a gap width that transmits the recoils and unreacted beam at that charge state while suppressing the remainder of the beam and recoils, eliminating about half of the unreacted projectiles. Higher order aberrations are corrected by specially designed shapes of the entrance and exit pole faces of the dipole magnets. An adjustable hexapole magnet in the first quadrupole (Q1Hex) along with a separate hexapole magnet (Hex1) were included for flexible corrections of second order terms that might result from imprecision in the higher order corrections from the dipoles. The Q1 magnet has a combined design where the quadrupole (Q1), hexapole (Q1Hex), and a correcting dipole (Q1Dipole) component can be set separately via independent power supplies. After setting Q1Hex for second order corrections, Q1Dipole is set accordingly to compensate for the dipole

effect introduced.

Section 2: Mass Separation and Projectile Rejection

The section from FP1 to first mass dispersive focus (FP2, located right before Q8) serves to separate the unreacted beam from the recoils that have similar momentum to charge ratios. In capture reactions, the emitted γ -rays carry off little momentum, leaving the recoils and beam particles with very similar momenta. The recoil will have a greater mass (by 1 amu for proton capture, 4 amu for α capture) and therefore a slightly lower velocity than the unreacted beam. The velocity filter WF1 in this section serves to separate these recoils from the beam. The values of the E and B fields in the WF are set in such a way to let recoils with the selected velocity v be equal to E/B pass through along the axis. Due to the momentum spread of the beam, the combination of magnetic dipoles and the WF creates an achromatic (no energy dispersion) focus at FP2 and is crucial to separate the particles by mass. The movable slits installed at this location are closed around the mass focused recoil to selectively stop the deflected beam. The magnets before and after WF1, quadrupoles Q6 and Q7 and hexapoles Hex2 and Hex3 along with the octupole Oct1, serve to optimize the mass separation in WF1, correct for higher order aberrations, and provide focus at FP2.

Section 3: Second Mass Separation and Projectile Rejection

This section extends from FP2 to the second mass dispersive focus (FP3, located right before Q12). It has a similar setup and function as Section 2, adding another two magnetic bending dipoles along with a second velocity filter (WF2) that is identical to WF1 with a mass focus at FP3 where movable slits serve to suppress the beam and only transmit the recoils with the desired mass. This second WF separation section provides an improvement on the unreacted beam suppression by increasing the mass resolution. It also provides additional suppression of the leaky beam that could arise from scattering and charge-changing reactions

along the beamline and especially within WF1.

Section 4: Cleanup and Recoil Detection

The section between FP3 up to the final detector station (FP4) provides a momentum analysis through B7 and B8 to clean up any remaining projectiles that have undergone one or multiple scattering reactions and no longer have the same momentum as the recoils. With that background reduced, the remaining particles are transported through the final detection area where a time-of-flight measurement is used to identify them. The final stopping detectors will further identify and count the particles making it to FP4, adding a suppression of 10^4 against background particles. The particles can also be detected in coincidence with γ -ray detection at the target. More details describing these detectors is provided in Sections 3.6.1 and 3.6.2.

3.3.1 Design Properties

The properties of the SECAR recoil separator as designed for a broad range of capture reactions [6] are summarized in Table 3.1. The design limits were chosen to provide optimal measurements of the extreme cases of reactions of interest that are relevant to novae and X-ray bursts which involve isotopes with masses up to $A = 65$ and atomic numbers up to $Z = 33$. The center of mass energy range of interest is determined by the temperature of the astrophysical environment, around 0.1 - 0.4 GK for novae and 0.2 - 3 GK for X-ray bursts. The peak and width of the Gamow energy distributions corresponding to these temperatures can be obtained using Equations 2.9 and 2.10, respectively, for proton capture on targets with $Z = 8 - 33$ to find that the range of interest spans 0.2 to 3 MeV. This range dictated the SECAR system's design parameters, including the magnetic and electric rigidity limits and the maximum high voltage needed in the WFs, using a number of reactions of astrophysical

Property	Value for Optimal Separator Function
Mass Range	15 - 65 amu
CM Energy Range	0.2 - 3 MeV
Rejection by Separator	10^{-13}
Rejection by Detectors	10^{-4}
Angular Acceptance	± 25 mrad
Energy Acceptance	± 3.1 %
Magnetic Rigidity Range	0.14 - 0.8 Tm
Electric Rigidity Range	1.25 - 19 MV

Table 3.1: SECAR separator properties for optimized direct measurements of p- and α -capture reactions on unstable proton-heavy nuclei.

interest and assuming a probable optimal charge state. In particular, the $^{15}\text{O}(\alpha, \gamma)^{19}\text{Ne}$ reaction at $E_{\text{CM}} = 0.5$ MeV with a recoil charge $Q = 3$ established the lower limits on magnetic and electric rigidity, while $^{65}\text{As}(p, \gamma)^{66}\text{Se}$ reaction at $E_{\text{CM}} = 3$ MeV with a recoil charge $Q = 21$ determined the upper limits. For a background free measurement during a two week experiment at maximum beam intensity of 10^{11} , the rejection requirement for SECAR is 10^{-13} with an additional rejection of about 10^{-4} from the detection system for a total of 10^{-17} . The recoil energy spread is typically small for most of measurements, and is designed to be up to $\pm 3.1\%$ based on the extreme case of $^{15}\text{O}(\alpha, \gamma)^{19}\text{Ne}$. The maximum angular acceptance of ± 25 mrad was adapted from the $^{15}\text{O}(\alpha, \gamma)$ at $E_{\text{CM}} = 0.5$ MeV as well, as it presents the largest scattering angle of the sampled reactions of interest (see Figure 1.2), with additional consideration to account for broadening of the angular range from beam spot effects.

3.3.2 Ion Optical Design

Beam optics describe the effect of electric and magnetic fields on moving charged particles. These particles can be focused and directed by these fields produced by different electromagnetic elements such as dipoles and quadrupoles. The trajectory and behavior of such particles

moving through a system of these elements can be modeled and optimized to transport a beam of particles with certain properties to a desired point along the beamline. SECAR is the result of an ion optical design that was developed to meet the design requirements listed in Table 3.1. In a recoil separator, the beam spot at different focal planes is important for the beam suppression of the device. For SECAR, these are FP1 for charge state separation, and FP2 and FP3 for mass separation. The ion optical code COSY INFINITY (v. 9.1) [64] was used to define the foci characteristics and design the separator [6].

In this thesis, the standard coordinate system defined in COSY will be used: the x-axis is perpendicular to the left and the y-axis is perpendicular up with respect to the beam axis. The distance measurements in COSY are in meters. The parameters a and b are defined as the angles of the ion velocity towards the x and y axis, respectively, in radian. The t , d , g , and z parameters are the fractional time, energy, mass and charge difference compared to a reference particle's mean value, respectively. A transfer matrix can be written to describe these beam parameters in first order at a given focal plane j , given the parameters at an initial plane i as such

$$\begin{pmatrix} x \\ a \\ y \\ b \\ t \\ d \\ g \\ z \end{pmatrix}_j = \begin{pmatrix} (x|x) & (x|a) & (x|y) & (x|b) & (x|t) & (x|d) & (x|g) & (x|z) \\ (a|x) & (a|a) & (a|y) & (a|b) & (a|t) & (a|d) & (a|g) & (a|z) \\ (y|x) & (y|a) & (y|y) & (y|b) & (y|t) & (y|d) & (y|g) & (y|z) \\ (b|x) & (b|a) & (b|y) & (b|b) & (b|t) & (b|d) & (b|g) & (b|z) \\ (t|x) & (t|a) & (t|y) & (t|b) & (t|t) & (t|d) & (t|g) & (t|z) \\ (d|x) & (d|a) & (d|y) & (d|b) & (d|t) & (d|d) & (d|g) & (d|z) \\ (g|x) & (g|a) & (g|y) & (g|b) & (g|t) & (g|d) & (g|g) & (g|z) \\ (z|x) & (z|a) & (z|y) & (z|b) & (z|t) & (z|d) & (z|g) & (z|z) \end{pmatrix}_j \begin{pmatrix} x \\ a \\ y \\ b \\ t \\ d \\ g \\ z \end{pmatrix}_i . \quad (3.1)$$

Each matrix element $(m|n)$ refers to the effect on m given the value of n at the initial location. For example, the first element is the linear magnification denoted as $(x|x)$ and signifies the position x at location j given the initial value of x at i . Similarly, $(x|z)$ describes the particle's distance x from the beam center at location j depending on its initial relative charge $z = dQ/Q$ at the plane i . Therefore given the initial beam parameters at the target, the deflection of the unreacted beam from the central heavy recoils can be calculated to first order at any plane by

$$x = (x|x)x_0 + (x|a)a_0 + (x|d)d + (x|g)g \quad (3.2)$$

where x_0 is the initial beam position, a_0 is the initial angular deviation in x , d is the energy dispersion and g is the mass dispersion.

In a recoil separator, a mass dispersive focus is necessary in at least one location to separate the unreacted beam from the recoils. The former is then suppressed using movable slits. At a mass dispersive plane, the mass dispersion element $(x|g)$ can not be equal to zero, while the energy dispersion $(x|d)$ is required to be zero, and $(x|x)$ and $(x|a)$ should be as small as possible. Ideally, $(x|a)$ is zero for a focus in the x-direction. The magnification term $(x|x)$ is always a constant, and a magnification greater than 1 indicates a spot larger than the spot at the target. The mass separation properties of the separator are determined by the mass dispersion $(x|g)$, and a large value leads to a large separation between unreacted particles and the recoils. The first order mass resolving power is defined as

$$R_m = \frac{(x|g)}{2x_0(x|x)} \quad (3.3)$$

where $2x_0$ is the full object size (spot size at the target). The mass resolution of the device is defined similarly by replacing the first order image size $2x_0(x|x)$ by the real object size calculated by including the higher order aberrations.

To determine the best design for SECAR, ion optical calculations up to fourth order were included in the design of the transport matrix, and from that the electromagnetic elements, their properties and their specific order in the beamline were determined. For that calculation, the following initialization of the beam properties at the target were set:

$$x_0 = \pm 0.75 \text{ mm}$$

$$a_0 = \pm 25 \text{ mrad}$$

$$y_0 = \pm 0.75 \text{ mm}$$

$$b_0 = \pm 25 \text{ mrad}$$

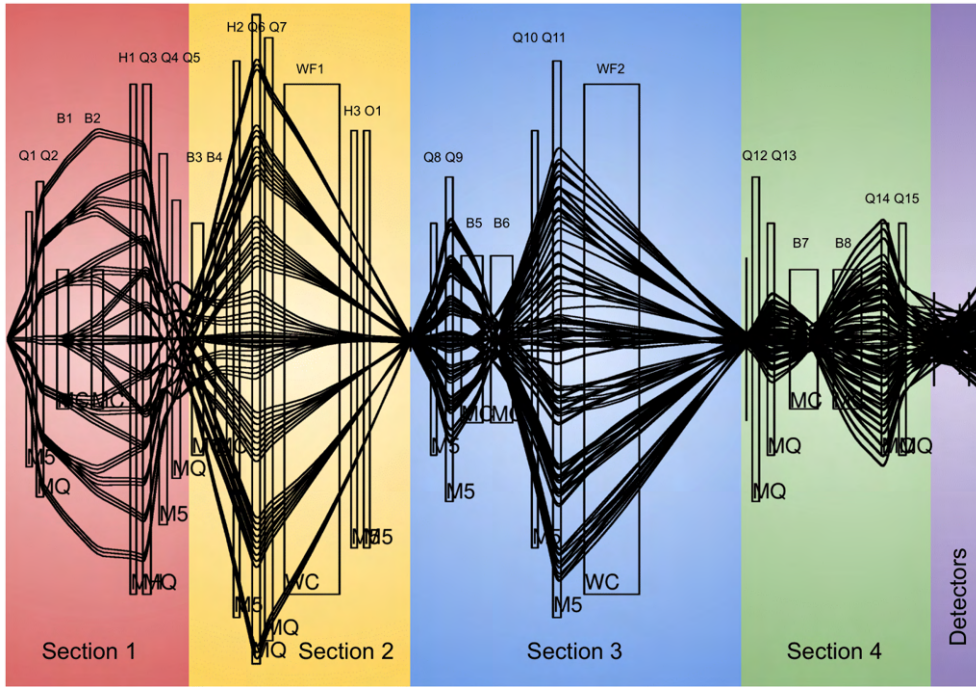
$$d_0 = \pm 3.1 \text{ \%},$$

where the x and y spot sizes correspond to the anticipated 1.5 mm beam diameter size delivered at the target from the ReA3 accelerator. The design of the elements and the beamline followed from this optimization [6]. Figure 3.4 displays 99 characteristic rays in the horizontal and vertical planes in the upper and lower panel, respectively, outlining the full SECAR ion optical profile from a COSY calculation for the edge case of a $^{65}\text{As}(p,\gamma)^{66}\text{Se}$ reaction at $B\rho = 0.8 \text{ Tm}$. The characteristic rays were defined within an ellipsoid of phase space given by the SECAR properties of maximum angular acceptance in the x- and y-direction of $\pm 25 \text{ mrad}$, and a maximum energy deviation from the recoil energy of the central ray of $\pm 3.1 \text{ \%}$. Each section described in Section 3.3 is marked with a different color and the foci can be seen at the end of each. Looking at the charge state selection (section 1) and the first mass selection (section 2) only, Figure 3.5 shows additional rays to further clarify the design separation properties. The red rays represent a case of an adjacent

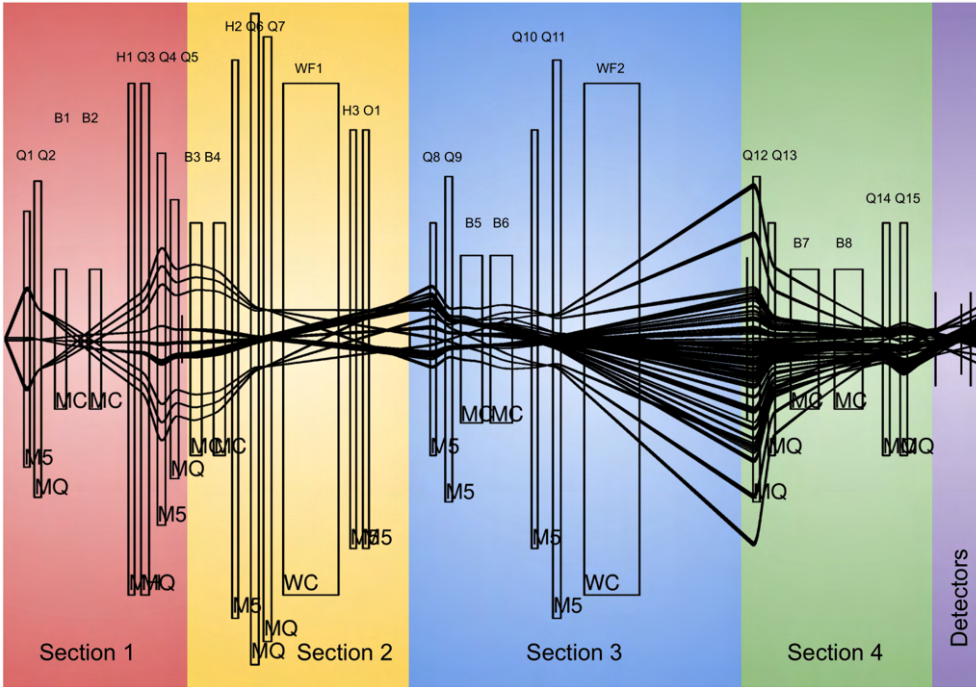
charge state ($\delta Q/Q = 1/21$) that is well separated at FP1. The blue rays correspond to the unreacted beam of similar rigidity as the recoils that gets separated by mass. The system has an achromatic focus where $(x|d) = 0$, $(a|d) = 0$ and $(x|a) = 0$ at FP2 and a zero dispersion focus $(x|d) = 0$ at FP3. It is estimated to have a mass resolving power at the first mass separation section FP2 of $R_m = 740$ and a resolution of 508. The second mass separation section at FP3 provides a mass resolving power of $R_m = 1300$ and a resolution of 767. It should be noted that the final detector plane FP4 is not a real ion optical focus (i.e. $(x|a)$ is not zero), but rather a location with a narrowed beam envelope where the beam size is reduced sufficiently in horizontal and vertical direction to match the size of the focal plane detectors along the entire length of the focal plane setup.

The dispersive elements, dipoles and WFs, serve to achieve the charge and mass dispersion at the focal planes. The dipole magnets all are designed to have a bending radius of 1.25 m and a maximum field in the good field region (GFR) of 0.64 T. The bending angle varies for each section and is 22.5 degrees for B1 - B4, 42.5 degrees for B5 and B6, and 55 degrees for B7 and B8. The WFs are identical and have a GFR horizontal electrode gap of 22 cm, a GFR vertical gap of 7 cm, a bending radius of 7 m, and the high voltage applied to the electrodes can reach ± 300 kV for a maximum electric field of 2.73 kV/mm between the two electrodes.

The COSY tune determined from these calculations was used in this work as the starting point for all SECAR commissioning runs. The pole tip fields for all of the quadrupoles, hexapoles and the octupole for a $B\rho = 0.8$ Tm is given in Table 3.2. The field settings for the beams used in all runs in this work were determined by appropriately scaling the optimized settings by the ratio of magnetic rigidities. Note that Q1 is a magnet with 3 components: a quadrupole component Q1, a hexapole component Q1Hex, and a dipole com-



(a)



(b)

Figure 3.4: The ion optics of SECAR for the layout explained in Section 3.3 corrected up to fourth order. The four sections are shown in different colors. Traces of rays in the horizontal (a) and vertical (b) planes are shown.

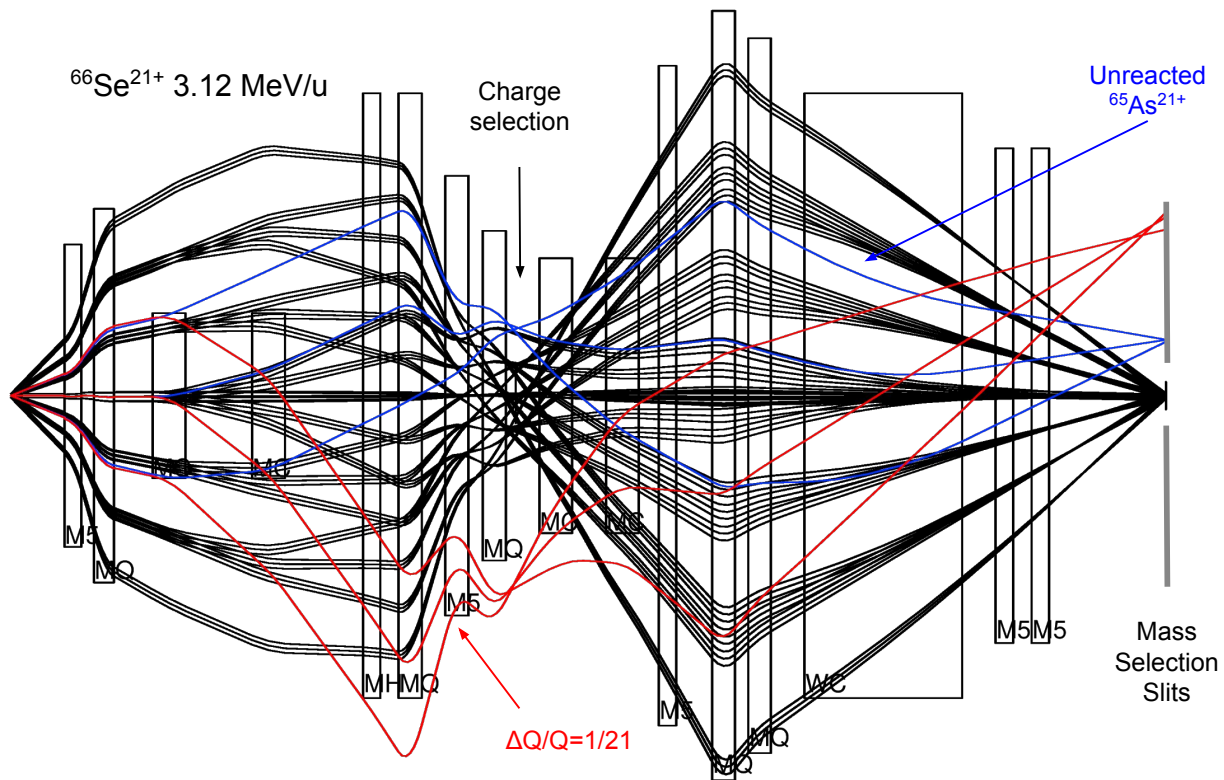


Figure 3.5: Example COSY INFINITY ion optics calculation up to the first mass separation slits of a $^{65}\text{As}(p,\gamma)^{66}\text{Se}$ reaction in the x-plane. The Se recoils are shown in black, unreacted As beam of similar $B\rho$ is shown in blue, and a beam of a nearby charge state is shown in red ($\delta Q/Q = 1/21$).

ponent Q1Dipole. The Q1Hex strength is determined and scaled from the COSY simulation value, while the Q1Dipole field is set as 28% of the scaled Q1Hex field strength. This stems from the fact that activation of the hexapole will produce a steering of the beam owing to the intrinsic dipole component of the forces. The dipole component is a result of the magnet design and needs to be compensated. Since the COSY command defining the Q1 magnet only includes higher order corrections such as the Q1Hex component, Q1Dipole is scaled directly from that and does not go into the COSY definition of Q1. Higher order corrections for other quadrupoles are not included in this table. In this theoretically optimized setup at the maximum design rigidity of 0.8 Tm, the dipole magnets with bending radius of 1.25 m require fields of 0.64 T (the design maximum field of these magnets), and the optimum settings of the WFs are 0.1143 T for the magnetic field and ± 308.3 kV for the high voltage on the electrodes ($E = 2.80$ kV/mm).

To practically achieve a separation close to the COSY predictions, the experimental beam parameters need to be as close as possible to the theoretical beam parameters set in the COSY simulation. To that end, a set of stringent requirements, summarized in Table 3.3, were established as the optimal beam conditions for all SECAR beam runs in this work. In Chapter 5, tuning procedures developed to achieve these requirement are discussed in detail.

3.4 Beam Diagnostics

Tuning a complex system such as SECAR would not be possible without diagnostic equipment installed along the beamline. In addition to aiding in tuning, devices such as slits serve to suppress unwanted beam when positioned correctly. Figure 3.6 presents all diagnostic

Magnet	B (T)
Q1	-0.39773
Q1Hex	0.00468
Q1Dipole	0.00131
Q2	0.21935
Hex1	0.01031
Q3	0.24287
Q4	-0.24756
Q5	0.11239
Hex2	0.01051
Q6	0.18163
Q7	-0.03002
Hex3	-0.00837
Oct1	0.031283
Q8	-0.14822
Q9	0.23438
Q10	-0.03367
Q11	0.16158
Q12	-0.18200
Q13	0.19100
Q14	0.12900
Q15	-0.13800

Table 3.2: Pole tip magnetic fields for COSY INFINITY nominal tune at 0.8 Tm used in this work.

Property	Requirement
Beam size at target	1.5×1.5 mm
Beam angular deviation	0 - 2.5 mrad
Beam width at mass slits	minimized
Transmission to final focus	100%

Table 3.3: Beam requirements for optimal recoil separation in SECAR.

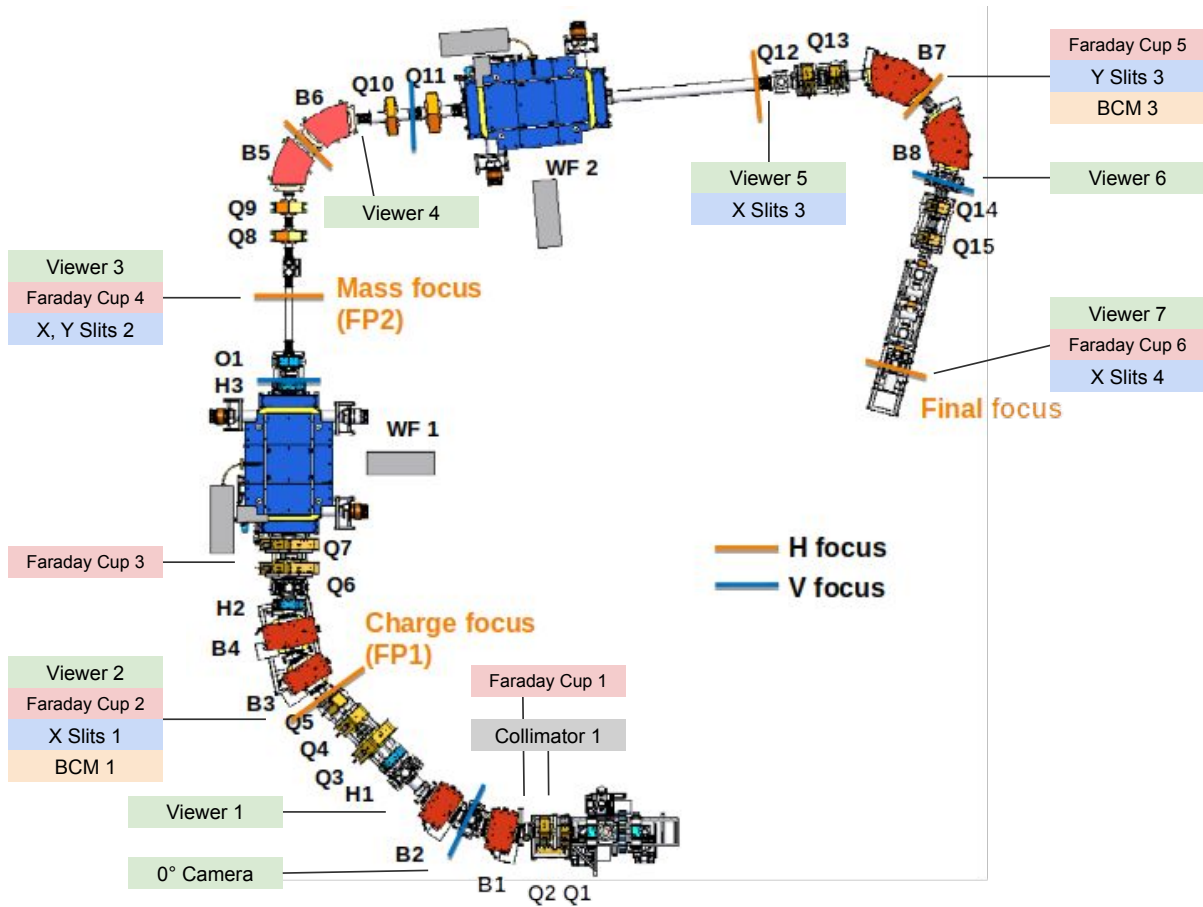


Figure 3.6: Diagnostics along the SECAR beamline.

devices installed or planned to be installed in SECAR. All these devices are mounted on isolated linear motor drives and thus can be positioned in or out of the beam's path. Some devices are mounted on the same drive for convenience, such as the 3-in-1 device at FP1 which includes the Faraday cup FC2, the viewer Viewer2 and the beam centering monitor BCM1.

Faraday cups (FCs) are common diagnostic devices that consist of a voltage suppressed beam stop that delivers a full absolute current measurement. They are the main current measurement tool used to evaluate beam transmission along the beamline. All SECAR cups consist of three electrically isolated parts: the cup itself, the suppression plate, and an unsuppressed aperture, as seen in Figure 3.7. A high voltage bias is applied to the

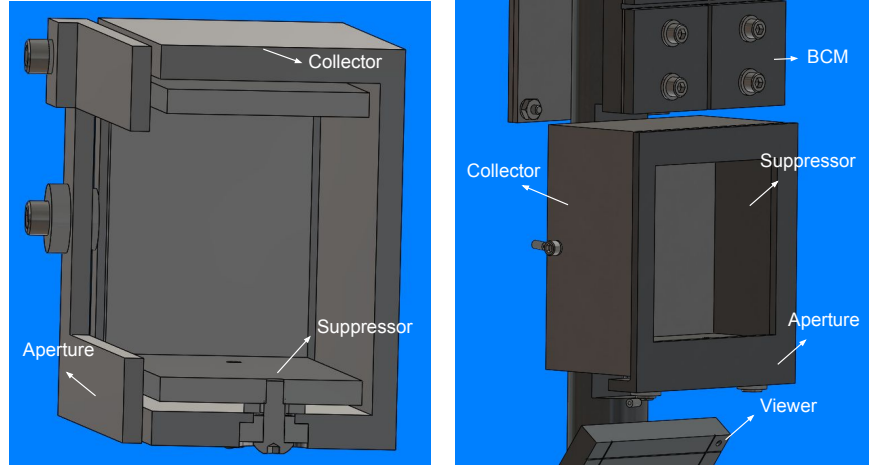


Figure 3.7: Faraday cup design for SECAR (left). Cup design in 3-in-1 device at FP1 (right).

suppression plate to suppress secondary electron emissions induced by the collision of beam particles with the collector that can cause inaccurate measurements. The cups are designed to have a 1 pA sensitivity ($\sim 10^6$ pps) and an electron suppression that provides a 1% current reading accuracy. Each cup is connected to a CAEN TetrAMM picoammeter device dedicated to accurate and fast low current measurements. The TetrAMMs are 4-channel 24 bit with an internal sampling rate of 100 kHz per channel. A configurable averaging rate of the sampled data can be set to reduce the transmission data rate, reduce high frequency noise and increase the signal-to-noise ratio. This rate must set to be a multiple of the EBIT beam pulse period for accurate measurements. The device provides two standard measuring ranges, ± 120 nA (15 fA resolution) or ± 120 μ A (15 pA resolution). It also includes a low-noise integrated bias voltage source (up to -500 V) that is used to provide the bias voltage for the FCs and is generally set to -200 V.

While the FC serves to provide a complete measurement of the beam current hitting it, the beam centering monitor (BCM) was designed to use current measurements as a tool to center the beam. Since 100% transmission of a selected recoil charge state is necessary, the centering of the pilot beam is crucial as any small misalignment will be magnified significantly

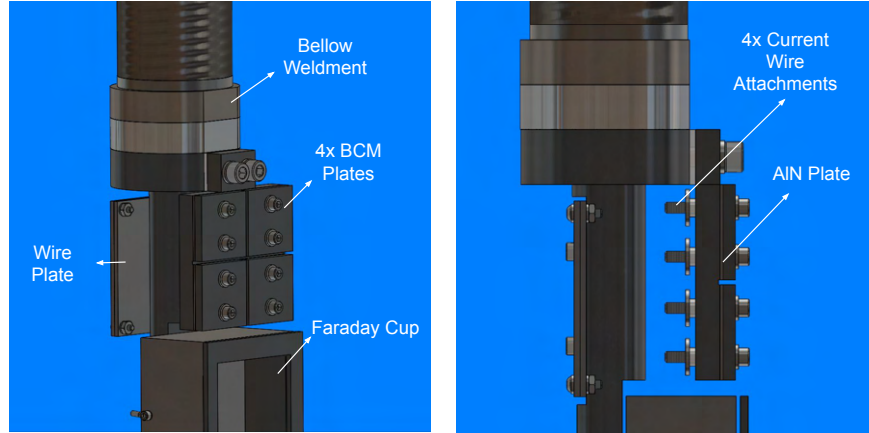


Figure 3.8: BCM design for SECAR shown on 3-in-1 device at FP1. Aluminum nitride (AlN) ceramic plate serves to electrically isolate the plates.

at the final focal plane 40 m downstream. Made up of four identical electrically isolated square plates as shown in Figure 3.8, the BCM reads four currents proportionally equal to the amount of beam hitting each plate. The BCM current readings are sampled by a TetrAMM device as well (described above). In order to center the beam, operators move the beam in such a way to equalize the current readings over all four plates. For accurate centering, the BCM must be well aligned with the ion optical axis of SECAR.

The slits offer an additional way to center the beam. When set to a small opening around the center position, the beam can be centered in the direction perpendicular to the gap by maximizing transmission. In addition, current is read from the slit blades, and balancing the current provides an alternative approach for centering provided the beam is larger than the slit gap. Monitoring transmission and blade currents while changing the gap size can provide information on the shape of the beam spot. The slits, similarly to the BCM, are unsuppressed and therefore are limited in their sensitivity compared to the Faraday cups. All slit systems installed in SECAR are movable across the center, and each plate is independently controlled providing the ability to create an asymmetric gap. Each system consists of two plates that are slightly offset, allowing a small overlap to be able to completely block the beam without

the plates colliding.

Some form of imaging diagnostic is often added to beamlines at different positions to aid in tuning. In SECAR, viewers consisting of a copper plate coated with fluorescent phosphorus (P22) inserted at 45° in the beamline, along with a CCD camera installed perpendicular to it, are used to image the beam location and shape at seven locations. The fluorescence is dependent on the beam intensity, and beam attenuation is often necessary to avoid destruction of the coating material. The attenuation strength is adjusted based on the beam intensity to reach currents that the viewer can withstand, typically in the 0.1 - 1 pA range.

The installation, testing and commissioning of the BCM, viewer and Faraday cup devices are described in Chapter 4 (Subsection 4.3.1). The 0-degree camera and the collimator were not yet installed during the commissioning presented in this work. The camera will be mounted in a zero degree port of the first dipole to provide images of the beam at the target, and the collimator will be installed between Q1 and Q2. Once available, they will be integrated into the tuning procedures discussed in Chapter 5, and will serve to aid in the centering of the beam along the optical axis of the beamline.

3.5 Gas Target Systems

To measure (p,γ) and (α,γ) capture reactions in inverse kinematics with SECAR, a hydrogen or helium target is needed. Solid targets come with several disadvantages, such as degradation over time due to beam exposure, contamination buildup, and background from reactions on other target components. Gas targets can eliminate some of these problems while introducing others. For example, a gas cell's thin windows can affect angular straggling and energy resolution, which can be detrimental for low energy capture measurements,

and static gas targets can degrade with beam exposure. For these reasons, SECAR was designed to employ a windowless gas target system. In the following subsections, the two main windowless gas targets to be used with SECAR are introduced: a gas jet and an extended gas cell.

3.5.1 JENSA Target System

The Jet Experiments in Nuclear Structure and Astrophysics (JENSA) is a windowless, differentially-pumped recirculating gas jet target system that was initially constructed and commissioned at ORNL [17]. It has an areal density up to 9×10^{18} atoms/cm², a narrow jet diameter of around 4 mm, and provides high purity and high stability gas jets. This target is sufficiently thick to provide a yield curve with a plateau for narrow resonance measurements as discussed in Chapter 2. Additionally since the target is localized, it provides a precise location for reactions and effectively creates a point source along the ion optical axis for the recoils entering SECAR, matching the requirements of the ion optical design. Along with being immune to beam degradation, the gas is recycled in the system further minimizing gas use and losses.

JENSA's design involves a de Laval nozzle (or convergent-divergent nozzle) to create the supersonic jet. A de Laval nozzle is a tube that is pinched in the middle, making an asymmetrical hourglass shape, used as a means of accelerating the flow of gas passing through it. Below the nozzle, two closely matched concentric cone-shaped receivers collect the expanding gas flowing out of the nozzle. The receivers are pumped by a series of high-throughput roots blowers and multi-stage roots pumps to generate constant air compression and exhaust into a high-throughput diaphragm compressor. The compressor operates with an inlet pressure as low as 1 atm and can maintain a maximum pressure up to 30 atm

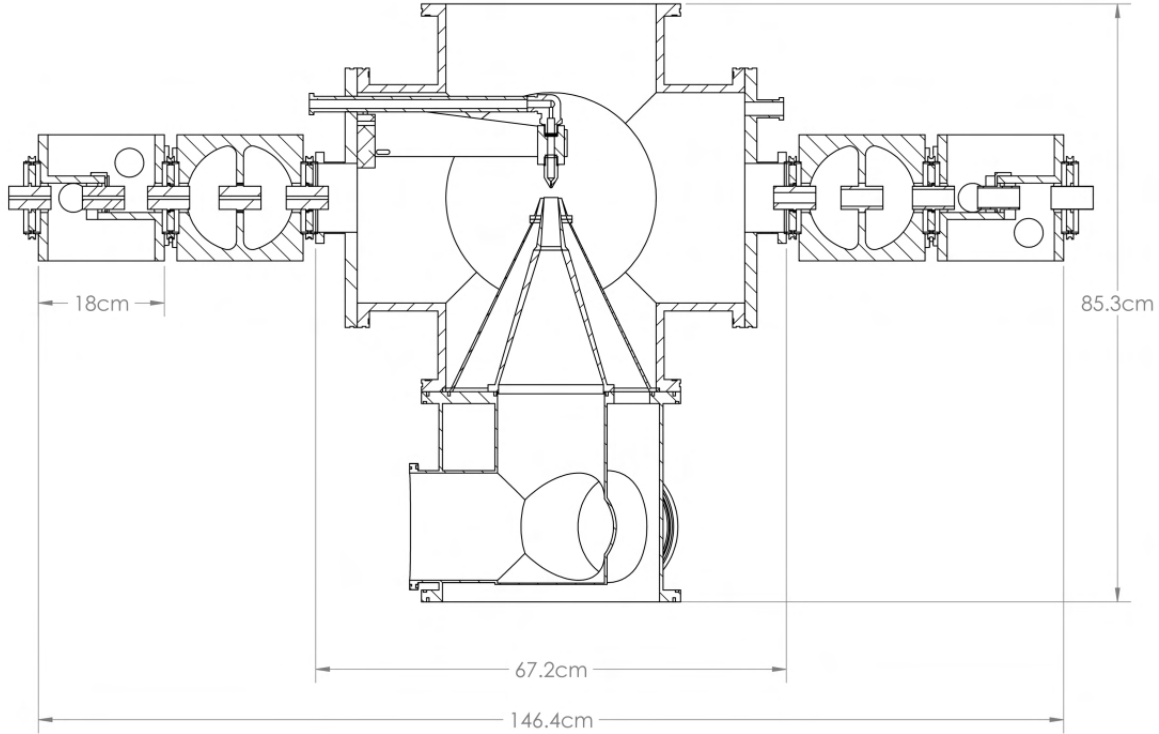


Figure 3.9: CAD drawing of JENSA chamber and its differential pumping components. The distance from the target location to the end of the final downstream pumping stage is 73 cm. Beam direction is right to left.

to produce the jet. Figure 3.9 shows a CAD drawing of the differential pumping system. There are four pumping stages upstream of the central chamber and four downstream, each separated by a gas-flow limiting aperture and equipped with a turbomolecular pump. The central chamber shows the nozzle and receivers. Any gas escaping from the receiver through the aperture is pumped by the turbo pumps.

Different de Laval nozzle designs with varying internal diameters can be used along with varying opening diameters of the receivers to control the amount of gas that is not collected by the system and escapes into the rest of the chamber. The installation of one of those nozzles along with the receivers in the ReA3 Hall is shown in Figure 3.10, and Figure 3.11



Figure 3.10: The JENSA nozzle and receiver installed in the ReA3 Hall. Beam direction is right to left.

shows a drawing of the installation upstream of SECAR, including the JENSA compressor and its pumping system.

A reduction in the pressure to the order of 10^{-6} Torr is achieved over the gas flow limiting apertures and pumping stages upstream and downstream of the jet. On the ReA3 side, the aperture dimensions are large enough to accommodate the beam. The smallest aperture, located directly upstream of the target, has a 6 mm diameter and a ± 3.4 mrad acceptance. On the separator side, the apertures are large enough to accommodate the recoil cone. The smallest one, installed directly downstream of the target, has a 4.5 mm diameter and a ± 32 mrad acceptance, while the aperture furthest downstream of the target (directly before Q1) has a diameter of 33 mm and a limiting acceptance of ± 25.4 mrad, large enough to accommodate SECAR's ± 25 mrad design acceptance.

In this work, all experimental runs were conducted with no gas in the JENSA target.

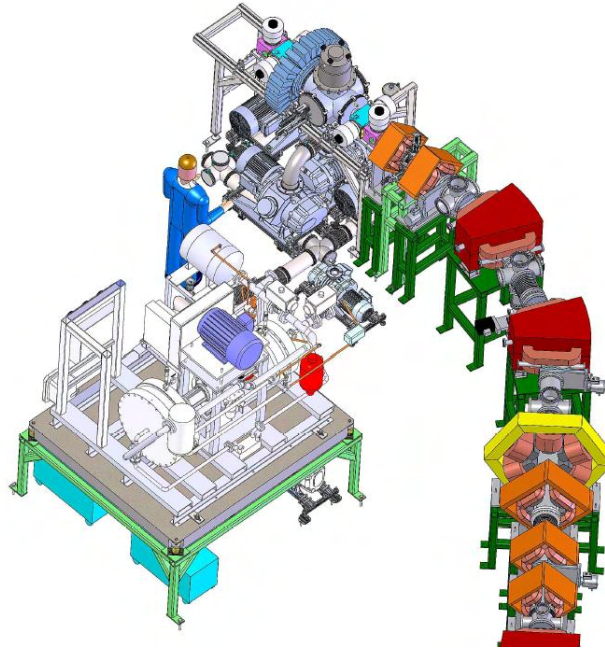


Figure 3.11: JENSA gas target assembly in the ReA3 Hall upstream of SECAR. SECAR elements up to Q5 shown. JENSA compressor shown in white on the left.

3.5.2 Extended Gas Target System

In the case of reaction measurements where the resonance energy is uncertain, it would be difficult to ensure the resonant reaction occurs well within the target thickness. An extended target with a length of 10 - 15 cm, combined with γ -ray detectors, is then ideal to locate the resonant reaction and ensure it occurs fully inside the target. The exact location of the resonance in the extended cell determines the location of where the capture reaction recoils are generated, which will then be the ion optical object for the device.

An extended gas target system with a gas cell length of 10 cm is being designed at the Colorado School of Mines to be used with SECAR. A drawing of the gas cell is shown in Figure 3.12. To minimize the effect of the extended target on the mass resolution of SECAR, the main target volume will be centered on the gas jet target location as determined by ion optics calculations. Scintillator crystals will be installed along the length of the target to

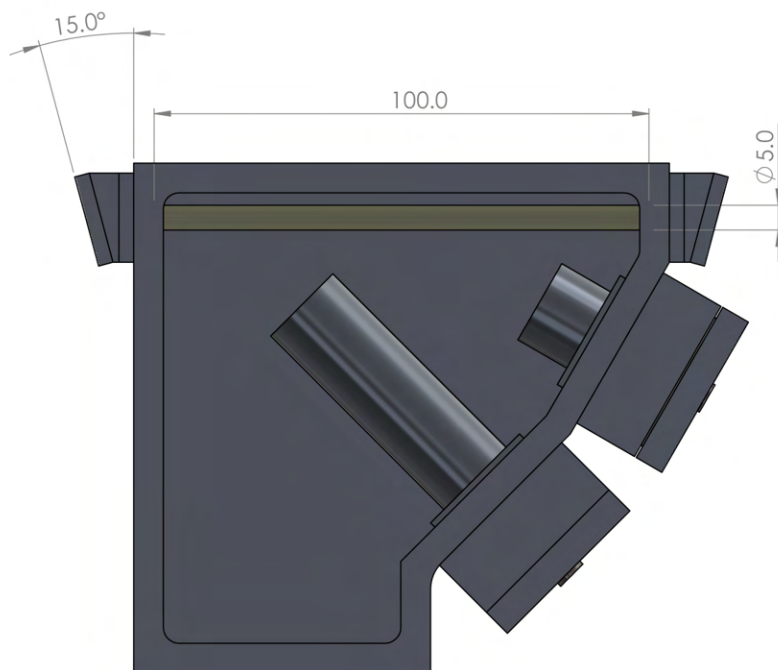


Figure 3.12: Drawing of the extended gas cell designed for use with SECAR at the Colorado School of Mines. Scale is in mm.

enable the locating and centering of a resonance with uncertain energy. More information about the scintillator array is given in Subsection 3.6.1. The extended target will operate with up to 10 Torr of hydrogen or helium gas. To achieve good vacuum, the setup will use a portion of the JENSA setup such as all the upstream and downstream differential pumping stages, and several of the roots blowers, the turbomolecular pumps and the multistage roots backing pumps.

3.6 Detectors and Data Acquisition

To detect the various particles taking part in the reactions happening at the target, the SECAR system employs two detector stations. The first consists of an array of scintillator detectors installed around the target chamber to detect the emitted γ -rays from radiative

capture. Additionally, silicon detectors can be used in the chamber for elastic scattering measurements, however that system is beyond the scope of this work. The second is a system of focal plane detectors used to identify and count the various recoils and projectiles reaching the end of the system at FP4. Together the two systems can be used in coincidence mode to further suppress background. In this section, the two stations are described, along with the data acquisition system used to process the signals from the detectors.

3.6.1 Gamma-Ray Detection

Due to the low number of reactions per second at astrophysical energies of interest, a highly efficient detector system is required. To achieve that, the proper detection material must be employed. Photon interactions with matter are fundamentally different than charged particle interactions, and the mechanisms vary with particle energy. A γ -ray can interact through three possible processes: the photoelectric effect dominates for low-energy γ -rays (up to several hundred keV), Compton scattering dominates for γ -rays with more than several hundred keV but less than 5 - 10 MeV, and pair production dominates for higher energy rays (above 5 - 10 MeV). All of these processes may partially or fully transfer the photon energy to an electron in the absorbing matter in a single or in multiple interactions. The cross sections of each process is different and depends on the atomic number Z of the interaction medium. The photoelectric effect varies with $Z^{4.5}$, the Compton scattering is proportional to Z , and the probability for pair production follows Z^2 . If an incident γ -ray is below the value at which pair production is significant, the resulting spectrum is the combined effects of Compton scattering and photoelectric absorption, and two prominent features are distinguished: a Compton continuum of energies corresponding to the Compton scattered electrons, and a narrow peak corresponding to photoelectrons (designated as the photopeak).

To maximize the efficiency, high- Z materials are required along with a reasonable efficiency at high energies (around 10 MeV). While the energy resolution is important, it is a secondary requirement to the efficiency especially since the recoils provide a clean identification of the reaction. In most cases, the room and beam-induced background are the main sources of background.

The SECAR γ -array for the target system utilizes bismuth germanate ($\text{Bi}_4\text{Ge}_3\text{O}_{12}$ or BGO) scintillation detectors placed around the target. BGO is a purely inorganic scintillation material with a high intrinsic efficiency due to the material's high density of 7.13 g/cm^3 . The very high atomic number ($Z = 83$) of Bi leads to a high detection efficiency of γ -rays including those at 10 MeV and above. Signals from the BGO arrays can be used in coincidence with a focal plane detector to improve background suppression. It can also serve as a start signal to measure the time-of-flight of a recoil ion through the separator. All of the BGO crystals are hexagonal shaped with a 35 mm face-to-face diameter and are 75 mm long. The signal from each detector is read out by a fast photomultiplier tube (1 -2 ns rise time) and each is equipped with a high voltage source. The energy resolution is at least 15% FWHM at 662 keV [14].

In the present jet target chamber design, one side of the chamber is occupied by a diagnostic drive comprised of a viewer and slits that are necessary for tuning the beam into JENSA, leaving only one side available for a γ -array installation. Figure 3.13 shows the array assembled in its rectangular flange, and an additional CAD image of the flange installation on the left side of the chamber in the downstream direction. This aluminum flange is 14 cm wide and 15.1 cm long, with a depth of 14.3 cm and a 0.5 cm thickness. The setup provides a geometrical efficiency on the order of 5% and assuming an intrinsic efficiency of 70% at 662 keV [74], provides a detection efficiency of 3.5% at 662 keV. Tests with a ^{137}Cs source

confirmed these calculations.

Another circular flange manufactured at the University of Notre Dame for the SECAR dipole calibration measurement is able to bring 15 BGO detectors closer to the target location, increasing the total efficiency of by about 2.5 times compared to the rectangular array described above. This flange has a 18.4 cm diameter and a depth of about 22.4 cm (Figure 6.3). The reader is referred to Chapter 6 for additional details about this setup.

A different BGO arrangement is planned for the JENSA extended gas target. This design includes 26 detectors as drawn in Figure 3.14, and is simulated to be 63% efficient at 662 keV, 49% at 1.274 MeV line, and at 27% at 5 MeV [14]. As this target configuration will be used when the energy of a resonance has sufficient uncertainty to make it difficult to reliably position inside the gas jet, the BGO crystals placed along the extended target provide position information that enables the locating and centering of the resonant reaction in the target.

3.6.2 Recoil Detection

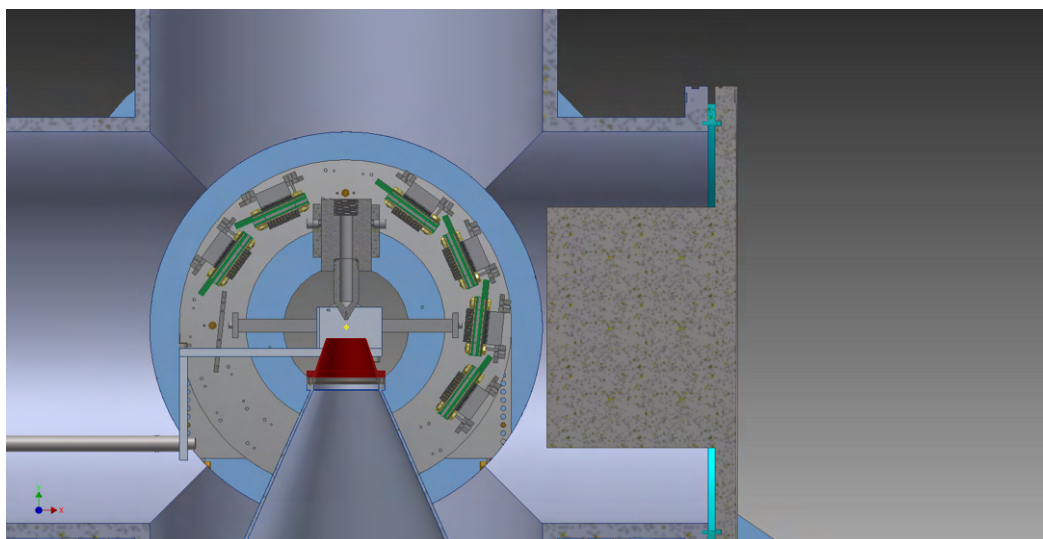
At the final focal plane, two microchannel plate detectors (MCP) for time-of-flight (TOF) measurements are installed, along with a gas ionization counter (IC) or a double-sided silicon strip detector (DSSD) as stopping detectors. Figure 3.15 shows a schematic of the focal plane detection system along the end of the SECAR beamline. The initial design and testing of this detector system was carried out at Louisiana State University (LSU) [46]. In the summer of 2019, the system was moved to MSU and installed in the SECAR beamline. The installation and testing of this system were completed as a part of the commissioning of SECAR, however they are beyond the scope of this work.



(a)



(b)



(c)

Figure 3.13: Current γ -array comprised of 19 BGO crystals for use with the JENSA gas jet (a,b), with a CAD showing the flange installed on the beamline left of the JENSA target looking downstream (c).

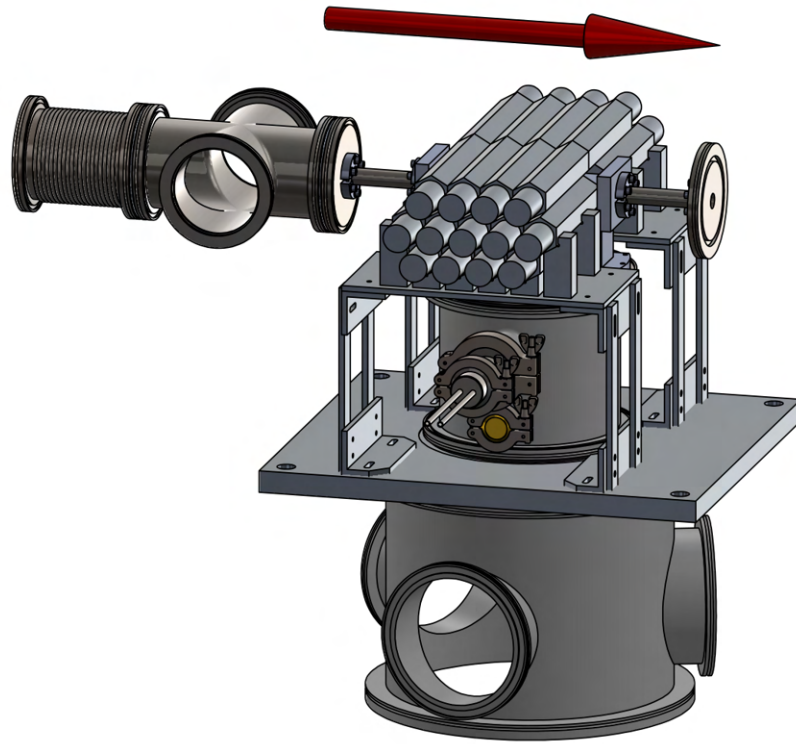


Figure 3.14: Drawing of BGO array around the extended gas cell as designed at the Colorado School of Mines.

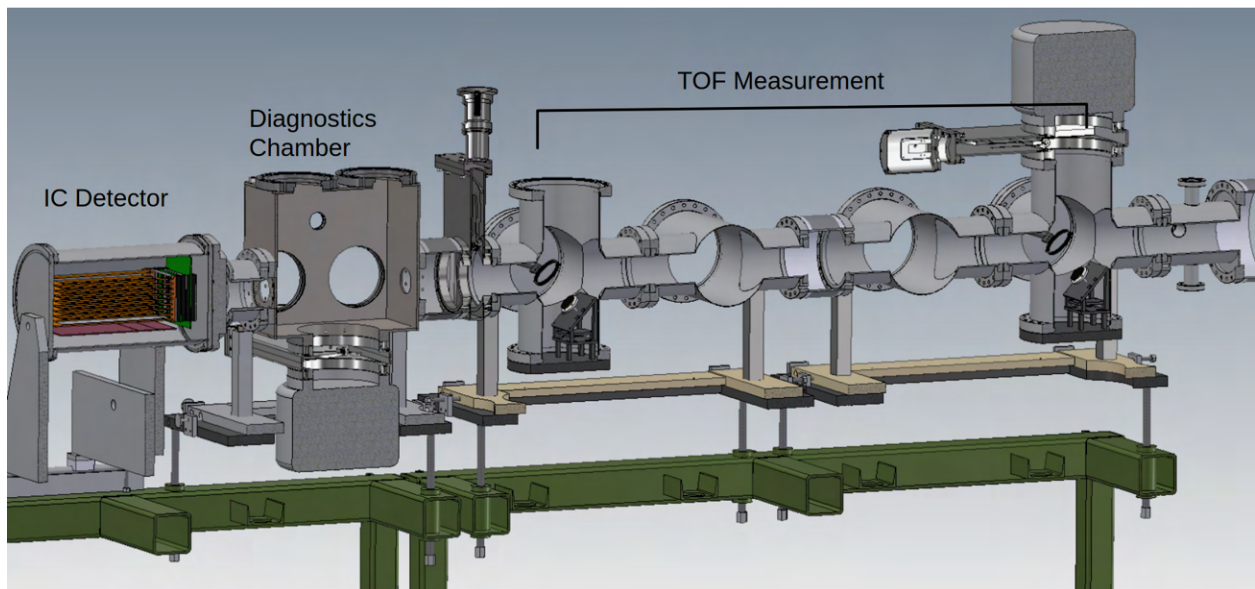


Figure 3.15: Schematic of the focal plane detection system at FP4.

Position-Sensitive Timing Detectors

The recoils first encounter the two MCP detectors as they arrive to the final focal plane section of SECAR. The MCP detectors are high resolution position-sensitive timing detectors that provide non-destructive measurements suitable for low-energy heavy ions. As the heavy ions pass through a metal foil, electrons are emitted and accelerated towards the MCP detector where a signal can be read. Given the small velocity difference between recoils and unreacted beam arriving at the focal plane, the time of flight of the particles between the two MCP detectors that are 1.39 m apart is accurately measured to identify each species. A magnet-focusing MCP design is adopted from [88] for use in the SECAR focal plane. This system has been used in experiments at the HRIBF [56] and the NSCL [66], and was shown to provide excellent position and timing resolution (around 1 mm and 1 ns, respectively) and to tolerate high instantaneous rates (up to 10^6 pps).

As can be seen from Figure 3.4, the beam size at the detectors station (purple shade) is dispersed in the horizontal direction. For that reason, a single tilted metal foil (mylar with aluminum coating) at 45° from the horizontal beam axis is utilized to maximize the acceptance in that direction. As ions pass through the foil, secondary electrons emitted are accelerated through a potential difference of around 550 V by a grid of thin high voltage gold-plated tungsten wires, located 3 mm from the foil, towards the MCP detector installed in alignment with the foil in the y-axis. One of the accelerating grid and metal foil systems and one of the installed MCP detectors are shown in Figure 3.16. A strong NdFeB permanent magnet is placed behind the MCP detector, forcing the electrons, which start out with some transverse momentum, into a helical motion along the magnetic field lines into the MCP detector. The MCP detector consists of two thin ceramic electron-multiplying microchannel plates stacked on top of each other. Each plate is made up of an array of tubes (channel

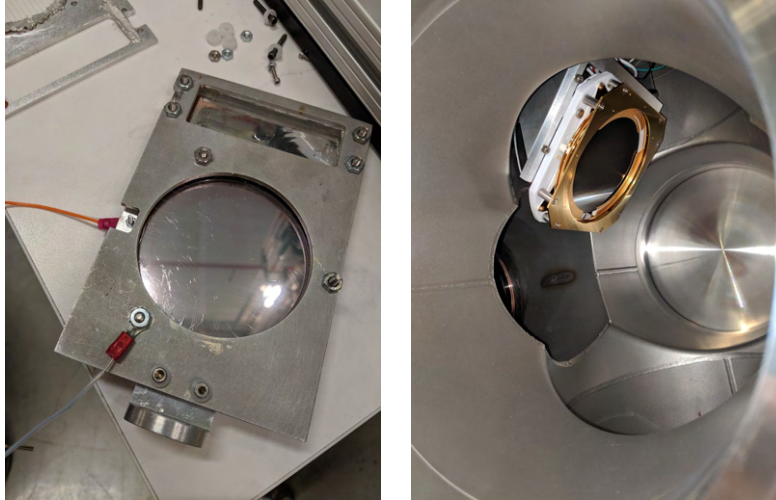


Figure 3.16: One of the accelerating grids and foil after assembly (left) and the MCP detector installed in the beamline (right). Once installed, the foil sits at 45° relative to the beam axis and parallel to the MCP detector.

multipliers) with a $12 \mu\text{m}$ diameter each acting as independent electron multipliers. The pulse from an initial electron entering a channel gets multiplied and strikes a resistive anode plate with four electrical contacts at each edge of the plate. Comparing the magnitude of the signals from the four contacts determines the position. The total electron transit time through a channel is a few nanoseconds, leading to the excellent timing properties of these detectors.

Final Stopping Detectors

After passing through the MCP detectors, the ions are stopped by a gas ionization chamber (e.g. for high energy measurements) or a silicon strip detector (e.g. at low energies). In the case of the former, the ions enter the IC through a thin window and lose energy in the gas filling the chamber, typically 50 - 500 Torr of isobutane due to its low ionization potential (10.8 eV) and mean energy for electron pair creation (23 eV). As the ions pass through the isobutane gas, they lose energy and slow down, ionizing the gas molecules along their paths. The ionized charged particles created are accelerated towards an anode and a cathode, and

the electrons resulting from the ionization drift due to the applied the electric field. The voltage induced is then measured on two collecting anodes and related to the initial energy of the ionizing particle. A relative energy loss ΔE measurement between the two sections provides particle identification to discriminate between the unreacted beam and recoils and any possible beam contaminants.

The design of the IC uses a standard cross-field ΔE -E design similar to the one in DRS [16] with added x-y position sensitivity using an electric field parallel to the motion of the heavy ions. The position measurement happens as the ions enter the IC where they pass through a series of five equipotential surfaces of thin gold-plated tungsten wires (25 μm diameter) layered in alternating cathode (wires 2 mm apart) and anode (wires 3 mm apart) planes and generating a uniform electric field parallel to the direction of motion. As the electrons are produced by ionization, they are accelerated and collected on the horizontal or vertical wires. The resulting signals as a function of position provide an x-y position measurement with a resolution of 3 mm or less. The energy measurements follow the position measurement section, utilizing a uniform electric field perpendicular to the direction of motion of the ions. The transverse field is created by 10 field shaping electrodes supplied by a 10-stage PMT tube voltage divider. As the ions pass through this section, the electrons drift to two anode plates while the positive ions drift towards the cathode in the opposite direction. The current collected on each anode depends on the amount of energy lost by the ion in that section. The first anode (7.5 cm length) provides a ΔE measurement followed by the second anode (22 cm length) that provides the full residual energy E. Compared to lower Z ions, heavier ions lose more energy in the first anode for the same total energy. Using this ΔE -E method, particles passing through the gas can be identified through a ΔE vs. E plot. Given the SECAR rejection and the expected radioactive beam intensities, the IC is expected to operate at

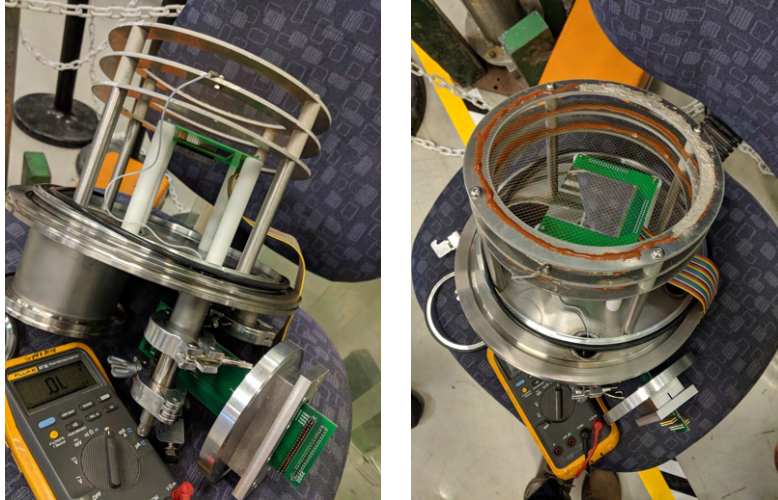


Figure 3.17: The ΔE -Si detector showing the grids and DSSD assembled before installation on the beamline.

rates greater than 10^4 pps without significant pileup.

A silicon strip detector can instead be used to stop the ions when a better total energy resolution is desired than what the IC can provide at the same energy. Silicon detectors are compact detectors with good energy resolution in charged particle detection, and good timing resolution due to a pulse rise time of around 10 ns. Additionally, by using a DSSD, 2D position resolution can be achieved by reading out the perpendicular strips on the front and back of the detector. A Micron Semiconductor BB7 detector can be installed as the final stopping detector. The BB7 DSSD design has 32 strips on each face with 2 mm pitch resulting in a full reactive area of $64 \text{ mm} \times 64 \text{ mm}$, covering the expected beam spot size at that plane.

While an IC is not required to be used with the silicon detector, a hybrid Si-gas stopping detector was implemented that can be used to measure ΔE in the gas and stop the ions in the DSSD. The assembled ΔE -Si detector is shown in Figure 3.17 before installation at MSU on the SECAR beamline.

3.6.3 Digital Data Acquisition System

The NSCL Digital Data Acquisition System (DDAS) is used to process the signals from all SECAR detectors [77]. The DDAS is a modular system composed of Pixie-16 (digital gamma finder) modules manufactured by XIA LLC distributed across up to eight compact PXI/PCI crates. Each Pixie-16 module has 16 channels that provide the signals from the detectors. That signal is then digitized via Analog Devices ADCs which can be either 14 or 16-bit, and 100, 250 or 500 Mega-Samples Per Second (MSPS). The modules have two hardware gain settings with 0.52 V and 1.2 V full-scale input ranges. A crate holds up to 13 of these modules, including a computer module, and the clocks can be synchronized between crates when multiple are in use. Each DDAS crate is typically read out by a computer through which the NSCL Data Acquisition software suite (NSCLDAQ) handles the data flow produced by the particles going through the detectors. The ReadoutGUI is the main interface with the NSCLDAQ where all experiment controls are generally handled.

For the SECAR system, a total of five Pixie-16 16-bit PXI Spectrometer with 250 MSPS ADCs are installed for the BGO and the focal plane detectors over two crates (one at the target and one at FP4). The two crates will have synchronized clocks when running the system in coincidence mode, and the data streams can be merged on one main DAQ computer to facilitate event building.

A subset of the BGO detectors presented in this chapter was used with the DDAS system in the dipole energy calibration experiment described in Chapter 6.

Chapter 4

Beamline Commissioning

4.1 Separator Control System

The NSCL and FRIB have a large distributed control system based on the Experimental Physics and Industrial Control System (EPICS) framework, integrating accelerator and experimental areas. EPICS is a set of software tools and applications that enable the use of distributed control systems to operate devices such as beamlines, including vacuum, power supplies, diagnostic support etc. As part of this thesis, this system was extended to SECAR following FRIB procedures and conventions.

In the past five years, the NSCL has adopted Control System Studio (CS-Studio) as the main graphical user interface tool for ReA3 controls to communicate with EPICS channels. CS-Studio is a set of control system interface tools that include real-time monitoring and controls for large scale systems such as accelerators. This includes high level applications such as making use of live data or of data stored in databases in history plots, an alarm handler, and save/restore options for device statuses, and more. In order to integrate SECAR with the ReA3 beamline, the control system pages for SECAR were built in CS-Studio, and customized based on current and future SECAR controls needs. Figures 4.1 and 4.2 show the interface designed for the main magnet controls page (which is also the main page of the SECAR controls), and the vacuum controls page in a separate tab, respectively. Figure 4.3 shows the tab that resulted from creating a shortcut to commands and overviews needed



Figure 4.1: The main global controls page for SECAR. Top left shows the magnet light that controls the ReA3 Hall SECAR light when the magnets are one, and to the right several buttons provide options to switch to other pages. The general menu tabs below show the magnet controls in this image.

for tuning during experiments, which were determined from experience and updated after each commissioning beam run. Clustering controls by type, task, or beamline section was deemed helpful to save time during monitoring and tuning, and to minimize confusion when operating the device.

As commissioning tasks evolved and tuning methods became more complex, Python scripts were written to handle tuning tasks and algorithms that were not possible through CS-Studio, such as dipole field matching and a Bayesian optimization of the beamline as described in detail in Chapter 5. These tuning tasks were automated once procedures were established and are handled through the command line. For such applications or other user-specific tasks that may be useful in the future, scripts and applications can be embedded into the user interface on CS-Studio to make them more accessible for scientific users.

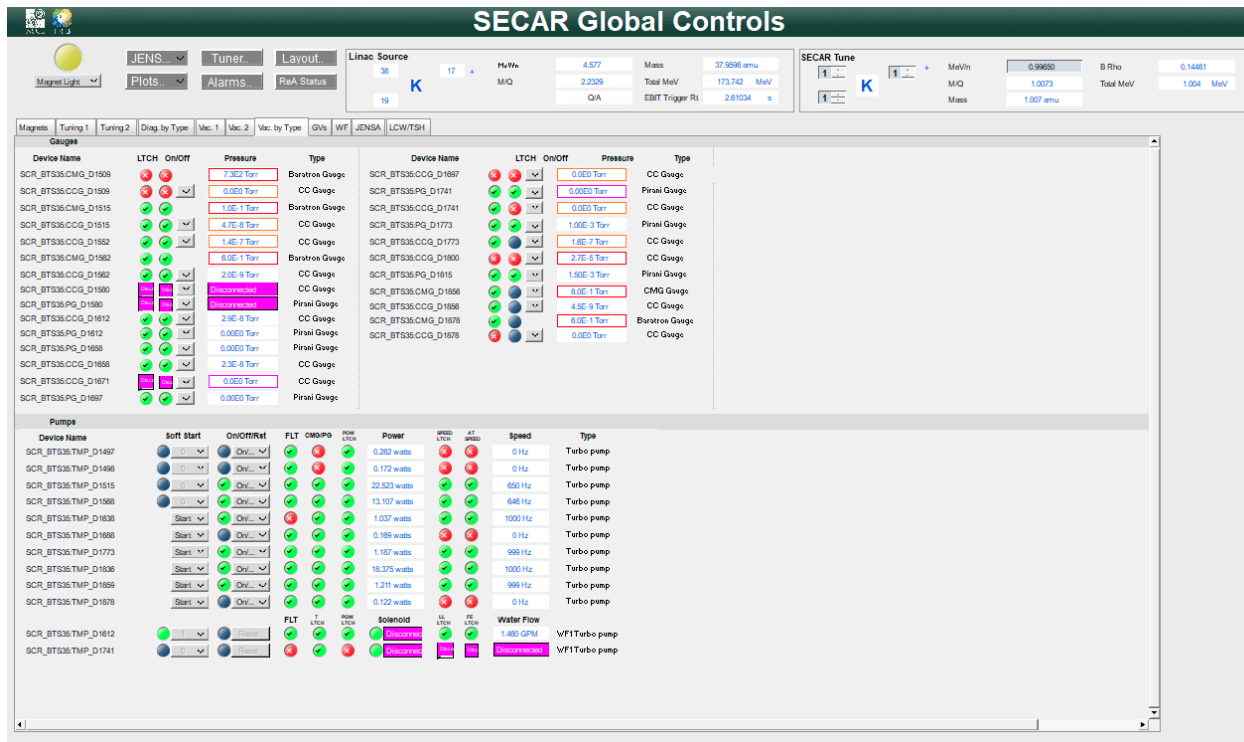


Figure 4.2: The vacuum summary page showing the controls and status of vacuum gauges and turbo pumps.

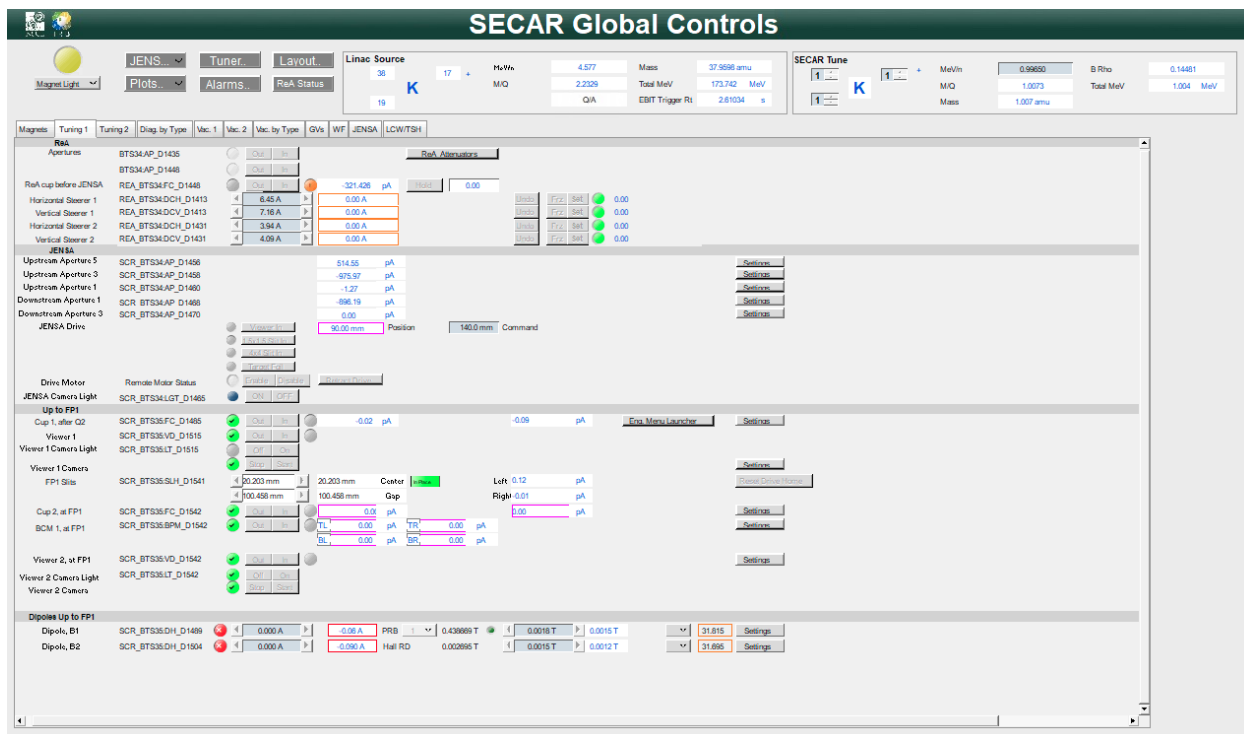


Figure 4.3: The controls page for SECAR showing the tab for controls during tuning. This was developed for use during experiments.

4.2 Magnet Stability and Reproducibility

SECAR consists of 10 dipole magnets (including two Wien filter magnets), 15 quadrupole magnets, and four higher order multipole magnets that need to be maintained within their specified field tolerances in order to achieve the desired SECAR mass resolution. Additionally, all of the SECAR magnets include an iron yoke to increase the magnetic field, making the resulting fields strongly dependent on their hysteresis history. Proper procedures to ensure a stable and reproducible magnetic field in all devices are needed.

The first two SECAR dipoles B1 and B2 are equipped with four Caylar NMR probes attached to a NMR20 Gaussmeter. These were used to run the tests presented in this section. One high range and one low range probe are each installed in B1 and B2, the former covering 0.16 to 0.8 T and the latter 0.037 to 0.18 T. The absolute precision of the field measurement of the NMR probes is in the order of 10^{-6} . These enable accurate absolute magnetic field measurements as these magnets will be used to define the beam energy during tuning (refer to Chapter 6 for the energy calibration). The remaining dipoles and the Wien filter magnets are each equipped with a Group 3 Hall probe connected to a DTM-151 Group 3 teslameter. These Hall probes also provide a temperature reading which was advantageous when studying temperature effects on the probes and magnets. Since the quadrupoles were not equipped with any magnetic field measuring devices, several of the Hall probes were removed from the dipoles and temporarily installed in the quadrupoles for the purposes of the tests presented in this work.

4.2.1 Magnet Cycling and Hysteresis

To reduce the uncertainty in the magnet strength caused by the iron core hysteresis effects and achieve adequately reproducible fields for scientific measurements, a standard procedure for cycling, or "degaussing", of the magnets was devised. The procedure allows for setting the magnet through setting the current on its hysteresis curve to reach its corresponding magnetic field on the excitation curve in a reproducible manner independently of the starting conditions, preventing differential hysteresis effects. Since magnets may need to be cycled several times during an experiment, several cycling procedures were tested and compared to balance the trade off between speed and performance.

The cycling procedures were developed to meet reproducibility specifications. To derive these, beam physics simulations with COSY were performed to study the impact of magnetic field variations on SECAR performance, setting a maximum limit of 2% on mass resolution change at FP2 from a single magnetic element's field variations. This resulted in a 0.01% tolerance specification on the magnetic fields of the quadrupoles, and Q3 and Q6 turned out to be the most critical, affecting the mass resolution by at least 2% when their fields vary by 0.01%. Q5 was shown to be the least critical, allowing up to 0.16% variance for mass resolution changes under 2%. From those results, a requirement of 0.01% was set for reproducibility and long term stability. This requirement was applied to dipoles as well to optimize the transmission for recoils. Figure 4.4 shows the reproducibility of B1 when cycled once with a 30 second pause time at maximum excitation. The measurements were recorded with the NMR probe set up in B1 using the following cycling procedure: The current is increased from zero to its maximum recommended value and kept at that value for 30 seconds. The current is then decreased to its final desired value. If a new lower

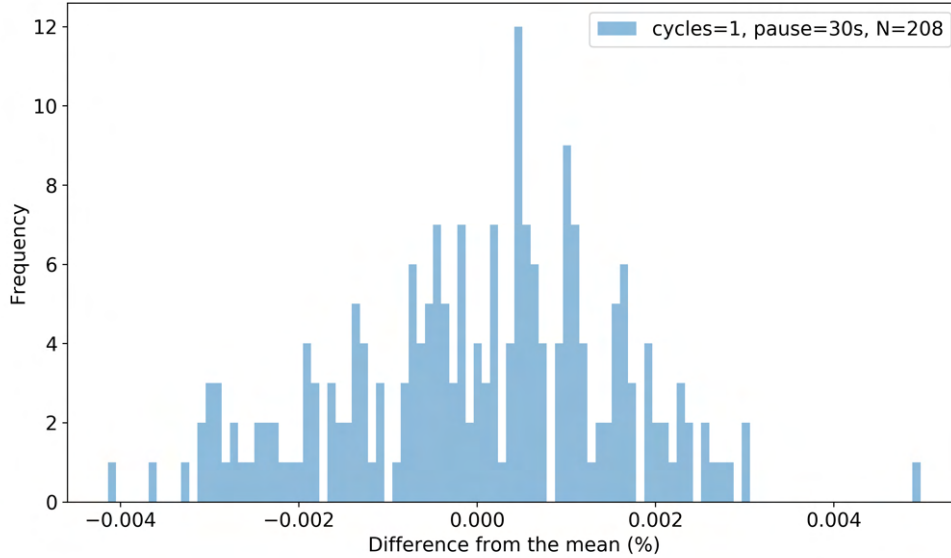


Figure 4.4: Dipole B1 magnetic field reproducibility measured with the NMR probe after 1 cycle with 30 s pause time. $N = 208$.

magnetic field needs to be set, the current is decreased to its appropriate value. If the new magnetic value is higher, the cycling procedure is repeated. For the test shown in Figure 4.4, B1 was set to 25% excitation (45 A) following the described cycling procedure for different randomly chosen starting points at 0%, 50% or 100% excitation. As shown, the magnetic field is reproducible for all 208 tests well within $\pm 0.01\%$. Similar results were found for B2.

The same test was run for Q6. Since the quadrupoles do not have a permanent field measuring device installed, a Hall probe was placed on one of its pole tips to perform these measurements. Figure 4.5 shows the results of 208 cycling tests using the same cycling procedure as described for B1 (blue histogram data), as well as 164 runs of a modified procedure that included 3 full cycles to maximum excitation with a 60 second wait time at each of the maximum and minimum excitation levels (orange histogram data). When cycling once, approximately 11% of time the final current falls outside of the $\pm 0.01\%$ of the

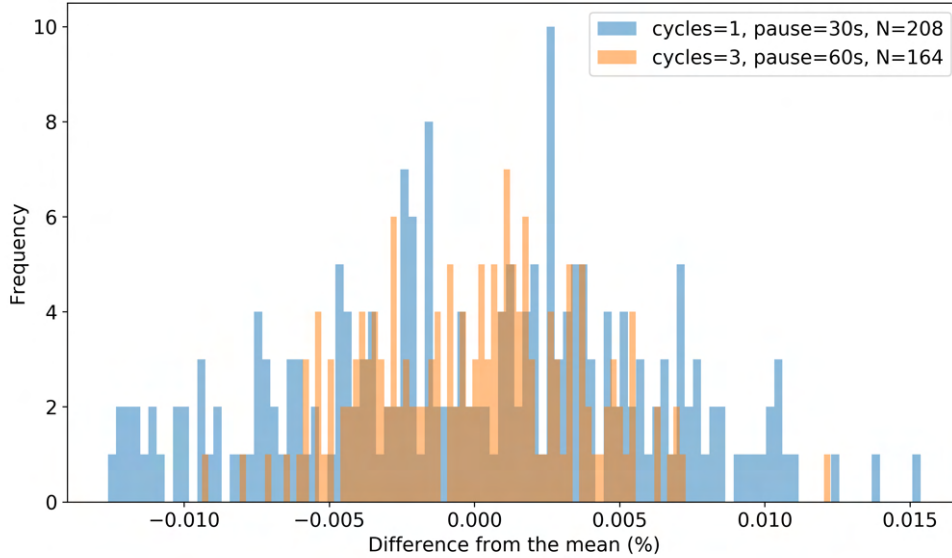


Figure 4.5: Quadrupole Q6 magnetic field reproducibility using two different cycling procedures, measured with a Group 3 Hall probe.

mean magnetic field, compared to 0.6% when cycling 3 times with a wait time twice as long. These results indicate that when running quadrupoles with mass resolution optimization as a priority, cycling 3 times with a 60 second wait time is critical.

4.2.2 Long Term Stability Tests

Magnetic field stability in each of the magnets is primarily achieved by controlling the exciting current. However, the magnetic field may be affected by additional effects such as changes in the magnetization of the magnet material, or temperature effects affecting the magnet. To be able to monitor the field stability to the accuracy required, sufficiently accurate measuring devices are needed. B1 and B2's magnetic fields are monitored by two Caylor NMR probes while the rest (B3 - B8) are equipped with Group 3 Hall probes. The absolute precision of the measurement of the magnetic field with the NMR probes is of the order of 10^{-6} . The Group 3 Hall probes are specified to have $\pm 0.01\%$ precision at 25°C . This is of



Figure 4.6: Dipole B1 magnetic field long term stability test as measured with NMR (top) and Hall probe (bottom). The dot-dashed lines correspond to $\pm 0.01\%$ stability levels. The flat lines between July 26 and July 29 correspond to a control system connection drop.

the order of the required stability. Tests of the performance of the Hall probes and their sensitivity to the environment in the ReA3 Hall were therefore necessary.

Group 3 Hall Probe Accuracy and Specifications

A performance test for the Hall probe was done by temporarily installing one of the probes along with the permanently installed NMR probe in B1. Figure 4.6 shows the results. The flat lines between July 26 and July 29 correspond to a control system connection drop. It can be seen that the B1 magnetic field is well within the specified 0.01% stability level as measured by the NMR probe. The Hall probe measurement shows significantly larger variations that can be attributed to the Hall probe precision. The measurement confirms the manufacturer's precision claim of 0.01%.

Due to air vents situated right above the SECAR beam line and to the proximity to the

rolling door in the ReA3 Hall that occasionally is open to the cold outside Michigan air, a study of the dependence of the Group 3 Hall probe on temperature was conducted using the same setup as the NMR-Hall stability test. Using an external heat source, the aluminum holder of the probes was heated by convection gradually from 25° to around 37°C and kept at that temperature for several days with B1 set to an arbitrary current. Figure 4.7, where the onset of heating is indicated with the black vertical line, shows that the NMR probe readings were not affected by the temperature rise and remained within $\pm 0.01\%$. The Hall probe shows a sharp drop at the onset of heating, most likely due to the movement of the system as it is very sensitive to any vibrations, then displays a slowly increasing magnetic field reading until surpasses the $\pm 0.01\%$ range four days later, right before the heating source was turned off as indicated by the sharp drop-off in temperature in the bottom plot. These tests confirmed the specifications of the device that state that under normal operating conditions (typical room temperature $\sim 25^\circ$) the Hall probe provides the 0.01% accuracy needed for monitoring magnetic field drifts, but that large temperature variations in excess of typical room temperature for long periods of time need to be avoided. It would be prudent to monitor the behavior of the probes on hot summer days or seasons with high average temperatures.

Dipole Field Long Term Stability

Similarly to the tests discussed in the previous section, magnetic field stability tests of dipoles B1, B2 and B5 have been performed by keeping their respective magnet current set for extended periods of time. For B1 and B2, the field was measured with the NMR probes, while the Hall probes were used for the other magnets. The magnet current stability is maintained by each magnet's power supply internal feedback loops using the read back current in the control system. Dipole tests for B2 and B5 showed similar results to B1

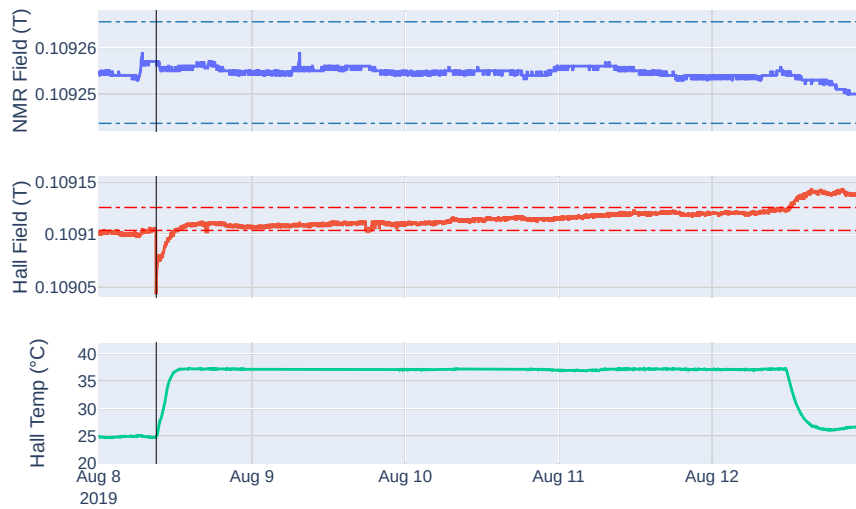


Figure 4.7: Dipole B1 magnetic field long term stability test as measured with NMR (top) and Hall probe (middle) in the presence of an external heating source from from 25 to 37°C. The dot-dashed lines correspond to $\pm 0.01\%$ stability levels and the black vertical line indicates the onset of heating. Bottom plot shows the Hall probe's temperature sensor readback.

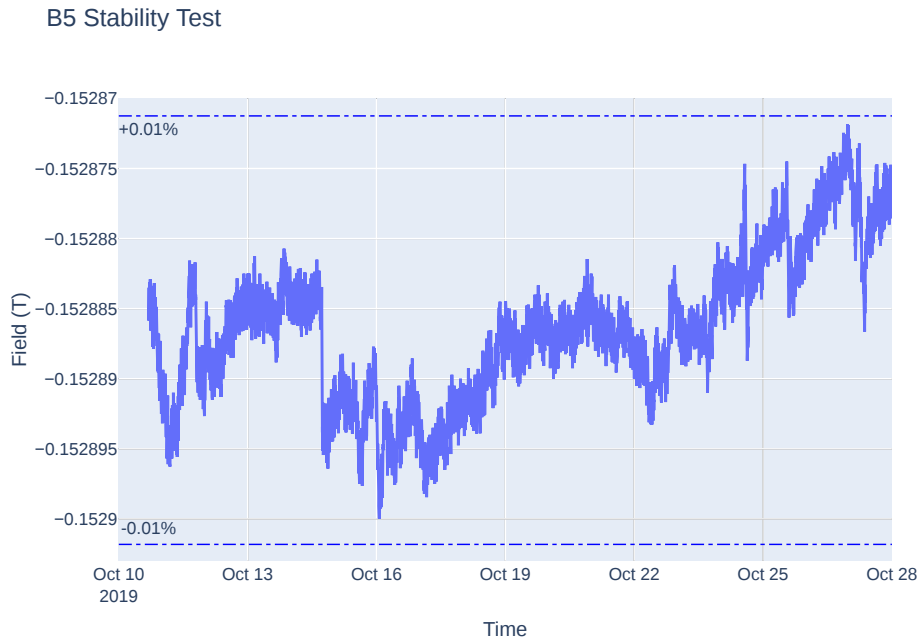


Figure 4.8: Dipole B5 magnetic field long term stability test as measured with a Hall probe. The dot-dashed lines correspond to $\pm 0.01\%$ stability levels.

shown in Figures 4.6. Figure 4.8 displays results from an 18 day stability test of B5, a duration equivalent to a long SECAR reaction rate measurement at a single beam energy. The magnetic field is stable within specification as indicated by the dot-dashed lines.

Quadrupole Field Long Term Stability

A similar setup used for the reproducibility tests with Q6 was also used in Q1 to study the field stability. A Hall probe was installed in Q1 and the magnetic field, along with the ambient temperature near the power supply rack and the temperatures of the inlet and the outlet cooling water of Q1, were monitored for about 84 hours. The Hall field and the ambient temperature are plotted over time in Figure 4.9. The magnetic field varied by at least $\pm 0.05\%$ during the test. Additionally, the Hall probe temperatures and the cooling water outlet temperature showed a fluctuation similar to the ambient temperature (data not included in this plot). While the cooling water warmed up to 27°C , the Hall probe experienced a temperature high of 33°C as it was placed directly on the warm magnet.

The most likely explanation of the field measurement variations that coincide with sudden

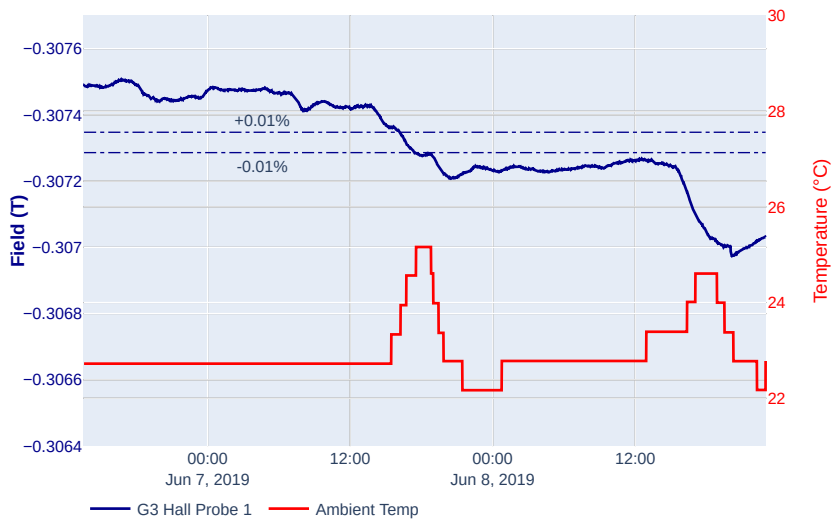


Figure 4.9: Quadrupole Q1 magnetic field long term stability test as measured with two Hall probes placed at different pole radii. The ambient temperature near the power supply rack (mezzanine) is shown in red. The overlaid dot-dashed lines correspond to $\pm 0.01\%$ of the mean of each reading.

changes in temperature (such as around 6 pm on both days in Figure 4.9) is the temperature sensitivity of the probe when the conditions surpassed typical room temperatures. However, the overall slow drift over time past the stability requirements when the room temperature was stable is attributed to the magnet itself. In order to address any slow drifts in the future, a plan to install Hall probes in quadrupoles is being set in place. This will allow the SECAR operators to identify and easily correct any magnetic field drift outside of the specifications or any other issues that could arise with the magnetic field that could affect the ion optics during experiments.

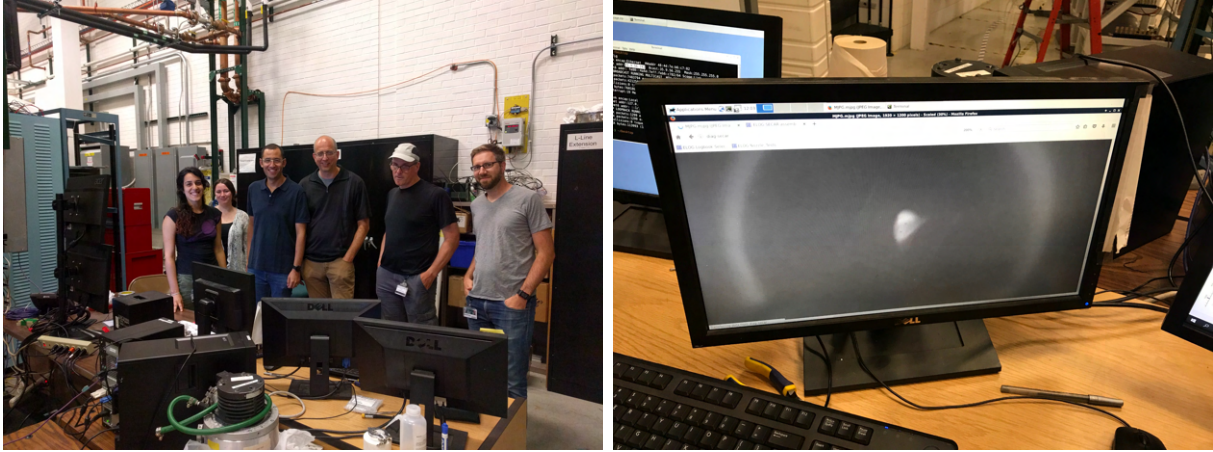


Figure 4.10: First beam spot on the FP1 viewer in SECAR on July 13, 2018.

4.3 Initial Tests with Beam

In July 2018, a proton beam was transmitted through SECAR up to FP1 for the first time. The first image of a beam spot in SECAR is shown in Figure 4.10, along with some of the SECAR team members that were present for that milestone. Since then, several test beams have been transported through the system. Table 4.1 provides a list of beam times discussed in this work with a summary of the main goal achieved during each run. A shutdown due to COVID-19 "stay-in-place" order by Michigan's Governor interrupted the commissioning schedule briefly. Nevertheless, experiments resumed in June 2020. These test beams were selected by beam particle, energy, and charge state, which determine the magnetic rigidity. A variety was chosen to test transmission and tuning of SECAR over its rigidity range (0.14 - 0.8 Tm). The energy uncertainty and energy spread of the ReA3 beams were approximately 0.5% (FWHM).

During the diagnostic tests detailed in Subsection 4.3.1 where the change in x-position at FP1 as a function of the B1 and B2 magnetic fields was measured, a dispersion of 1363 ± 68 (5%) $\text{mm}/\frac{dB}{B}$ was obtained for the dipoles. This is $\sim 8\%$ lower than COSY predictions.

Date	Beam	E (MeV/u)	$B\rho$ (Tm)	Goal
Jul. 13 2018	H_2^+	2.97	0.5000	First Beam
Jul. 19 2018	H_2^+	2.97	0.5000	Tuning to FP1, Ion Optics Studies
Jul. 25 - 27 2018	H_2^+	2.97	0.5000	Diagnostics Testing, Automated Tuning Tests
Feb. 12 - 14 2019	$^{40}\text{Ar}^{14+}$	2.86	0.6954	Tuning to FP1, Ion Optics Studies
Feb. 21 - 23 2019	$^{40}\text{Ar}^{14+}$	2.81	0.6893	Tuning to FP1, Energy Scaling
Mar. 10 - 12 2019	$^{40}\text{Ar}^{14+}$	2.86	0.6954	Tuning to FP1, Energy Scaling
Mar. 25 - 28 2019	$^{23}\text{Na}^{8+}$	0.30	0.2266	Tuning to FP1, Energy Scaling
Apr. 4 - 5 2019	$^{23}\text{Na}^{8+}$	2.50	0.6545	Diagnostics Testing and Troubleshooting
Aug. 26 - 29 2019	$^{14}\text{N}^{6+}$	4.08	0.6799	Tuning to FP2 with WF1
Sep. 3 - 12 2019	H_2^+	0.99	0.2888	Dipole Energy Calibration
Mar. 2 - 9 2020	$\text{H}_2^+, ^1\text{H}^+$	0.99, 1.80	0.1444 - 0.3891	Dipole Energy Calibration, Automated Tuning Tests
Jun. 8 - 11 2020	$^{133}\text{Cs}^{41+}$	0.96	0.4573	Tuning to FP2 with WF1, Quad Optimization
Jun. 15 - 20 2020	$^{133}\text{Cs}^{41+}$	1.00	0.4667	Tuning to FP3 with WF1
Jun. 20 - Jul. 2 2020	$^{133}\text{Cs}^{41+}$	1.00	0.4667	Tuning to FP4 with WF1
Jul. 20 - 24 2020	$^{20}\text{Ne}^{8+}$	1.12, 1.16	0.3809, 0.3887	Tuning to FP4 with WF1 with He Jet
Jul. 27 - 30 2020	$^{20}\text{Ne}^{8+}$	1.18	0.3911	Tuning to FP4 with WF1 with He Jet

Table 4.1: SECAR commissioning runs.

4.3.1 Diagnostic Devices Tests

In Chapter 3, the SECAR beamline was described including a detailed map of the diagnostic devices installed along the instrument as shown in Figure 3.6. During the commissioning discussed in this work, the collimator and the zero-degree camera were not yet installed, and the beamline up to FP2 was the main focus of the work. In this section, the installation and testing of the Faraday cups, viewers and BCMs are discussed as they pertain to the commissioning of SECAR up to FP2.

Assembly and Installation

In June 2018, the diagnostic devices for the SECAR beamline up to FP1 were assembled and installed, except for the slits which were installed the following year. The remainder of the diagnostics up to FP2 were installed in 2019. Figure 4.11 shows the first Faraday cup (FC1) installed in SECAR (located before the first set of dipoles) assembled in the clean room. This is the main cup used when centering through JENSA into SECAR, and it is one of the larger cups installed in this beamline. As described in Chapter 3, all Faraday cups in SECAR are composed of a collector and an aperture that are electrically isolated from each other and that independently read current. Only the collector is voltage suppressed, and that is achieved by an isolated plate installed in front of the inner sides of the collector.

Throughout the beamline, some diagnostic devices were designed to share a drive as shown for the 3-in-1 device at FP1 in Chapter 3. Figure 4.12 shows the 3-in-1 diagnostic drive after assembly and before installation at FP1. From left to right, BCM1, FC2 and Viewer2 are shown. The five dot markings in the center of the viewer plate indicate a 5 mm distance between each two dots. All viewers in SECAR have similar marks in their center. In this image, the viewer had not yet been coated with the phosphorus. Figure 4.13 shows

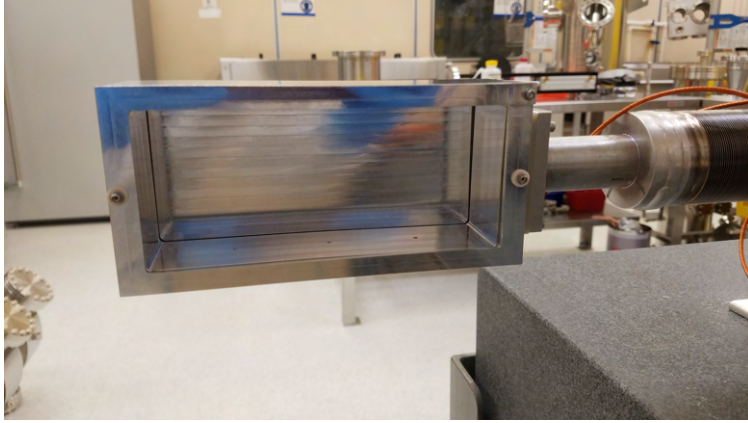


Figure 4.11: FC1 assembled in the clean room.

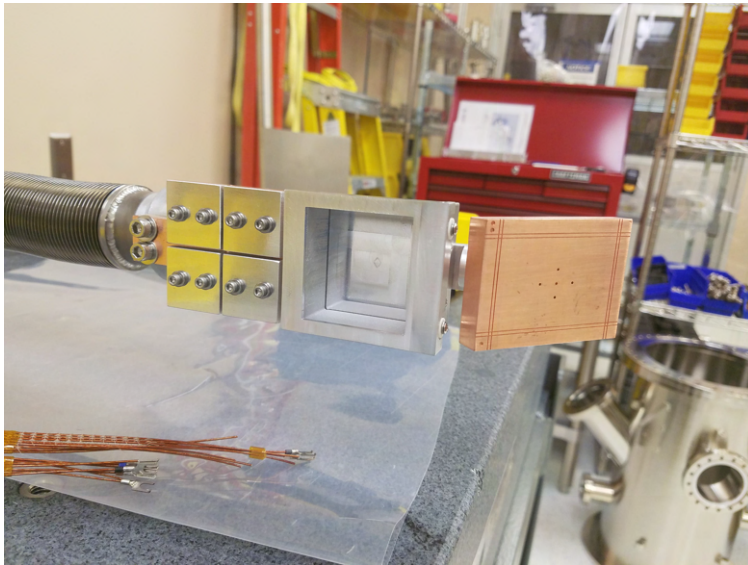


Figure 4.12: The 3-in-1 diagnostic drive to be installed at FP1, assembled in the clean room. From left to right: BCM, Faraday cup, and viewer plate (uncoated).

Viewer2 after being coated, and Figure 4.14 shows Viewer1 after installation on its actuator drive downstream of B2, inserted into position along the beamline.

Faraday Cup Beam Tests

The suppression voltage needed for the cups was determined during one of the July 2018 runs with an H_2^+ beam impinging on FC1. The suppression was slowly increased and the current readback of the collector was recorded. The results are shown in Figure 4.15. Following that, the operating suppression voltage was established as -200 V for all SECAR

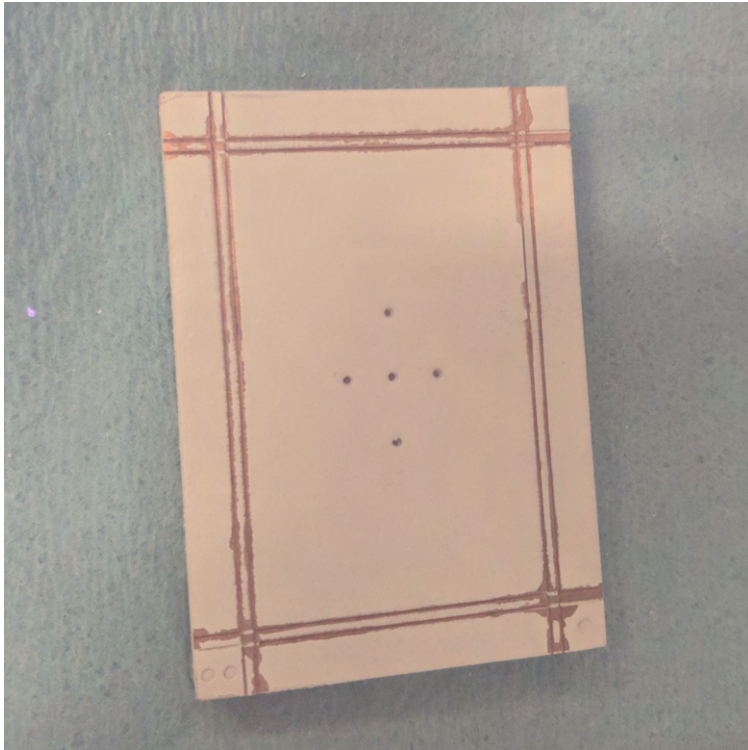


Figure 4.13: A P22 coat on the Viewer2 plate before installation.

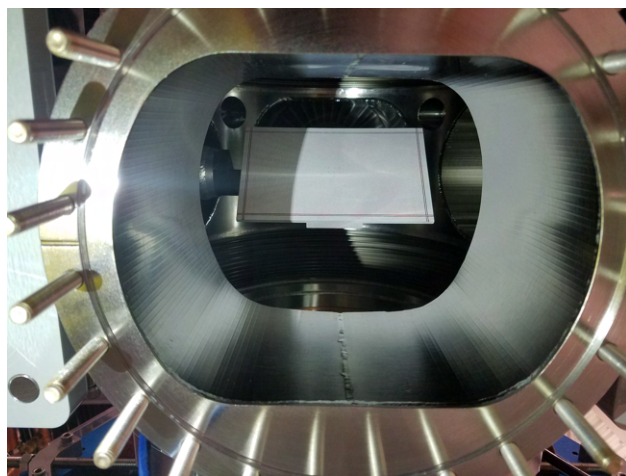


Figure 4.14: Viewer1 installed and inserted in the beamline.

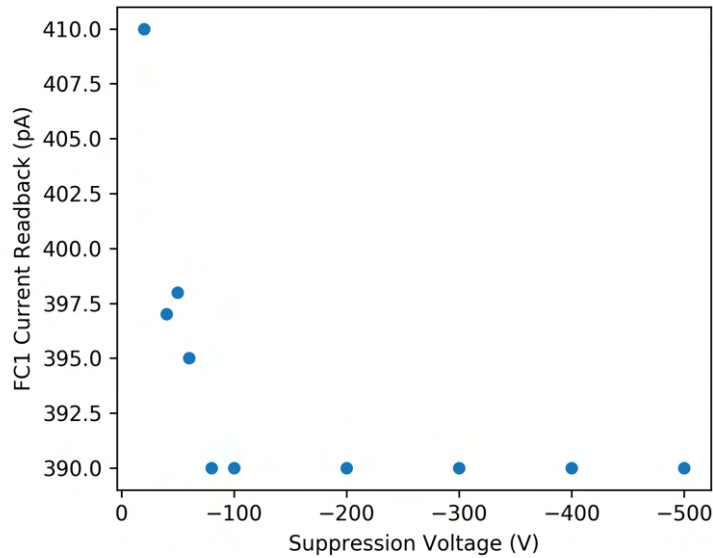


Figure 4.15: FC1 suppression voltage test.

cups. In later commissioning runs, a 10% to 25% discrepancy was occasionally observed in some of the readings, notably with FC3 (BTS35:D1563, before WF1) when compared to the ReA3 cup upstream of JENSA (BTS34:D1448) and to FC1. Table 4.2 displays the readings from all cups up to FC2 with their ratio to the ReA3 cup before JENSA. The discrepancy in most of the cups was occasional and did not exceed 10%, except for FC3 which did not improve even with an increased the suppression voltage past -200 V. This may be explained by the fact that FC3 is the largest of the cups to accommodate the large and unfocused beam spot size at that location. The beam may be hitting the suppression plates or the aperture and causing secondary electrons. This minor issue did not affect transmission estimates during early commissioning, however it may be necessary in the future to address the issue if it introduces any tuning problems.

Viewer Image Analysis

Each viewer plate along the beamline is paired with an adjustable CCD camera and a manual light. From the viewer camera data stream, images can be saved in TIFF format.

Cup/Location	Current (pA)	Ratio to ReA3 Cup
ReA/BTS34:D1448	62	1
FC1/BTS35:D1485	60	0.97
FC2/BTS35:D1542	65	1.04
FC3/BTS35:D1563	75	1.21
FC4/BTS35:D1638	66	1.06

Table 4.2: Faraday cup collector current readbacks up to FP2 after tuning the $^{20}\text{Ne}^{8+}$ beam in July 2020.

For beam centering and tuning, it was advantageous to create a way to objectively analyze the viewer images and quantify the different beam spot parameters, as doing it by eye was not sufficiently accurate especially with weak beams. To facilitate obtaining a scale for the images, an image with the light on where the dots detailing the center region of the viewer are visible was taken for each viewer. The dots are used to scale the beam position and movements during experiments. Figure 4.16 shows an example of a processed image of a beam spot. To achieve the final results, a Python program was written to subtract a background image taken without beam on the viewer, and detect the center dots in the image of the viewer with the light on to provide the scale in mm. The red vertical and horizontal lines indicate the center of the beam spot. This image processing became a key component in the automated tuning methods discussed in Chapter 5.

To achieve these results, the TIFF images were imported as a 2D array of numbers, and the background image was subtracted element by element from the beam image. The data was subsequently integrated column by column for each of the x and y axes resulting in a 1D beam profile in each axis. These distributions were then used to find the location and the width of the beam spot. In this work, the center location was calculated by finding the median of the beam profile distribution in each dimension. The median was defined as the first point (pixel location) where the ratio of the cumulative integration of the beam profile

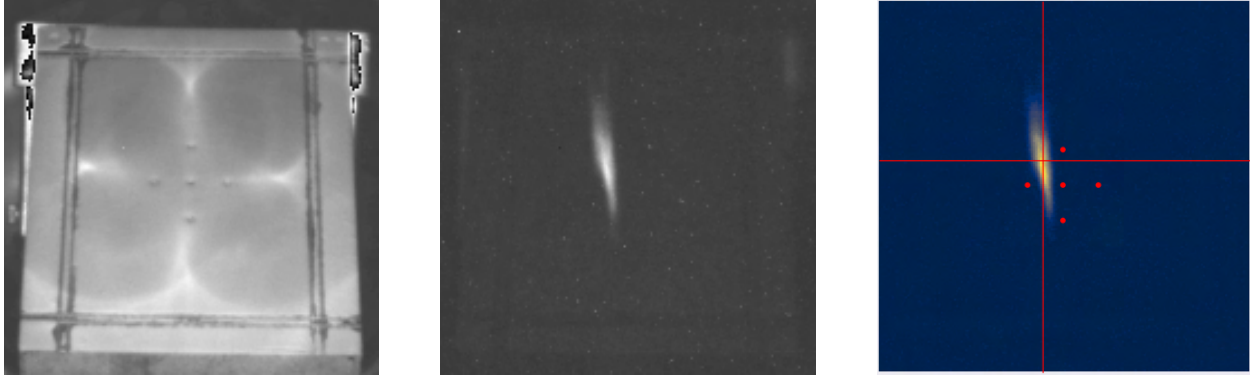


Figure 4.16: Viewer image analysis process. Left: CCD image of the image with light on to find scale from the 5 mm dot markings. Center: Raw TIFF image of the beam from CCD. Right: Background subtracted beam image with the red lines marking the beam spot center, and red dots indicating the center with 5 mm distance between each dot. In this image, each pixel corresponds to approximately 0.15 mm.

to the total integration over the entire axis is greater than or equal to 50%. Other methods were considered such as fitting the beam spot shape with one or more Gaussian shapes or finding the weighted mean of the distribution, however the median method was chosen due to its robustness when handling any irregular beam shapes including heavy tails that occur due to optical effects upstream. The beam spot width was needed for beam optics optimizations and was defined as $\pm 1\sigma$ of each beam profile distribution. This was found using the same ratio of cumulative sum over total sum and taking the pixel location where the integral was closest to 15.9% as -1σ , and 84.1% as $+1\sigma$. Figure 4.17 is an example of the full image processing results.

Beam Centering Methods

The SECAR beamline includes two diagnostic devices, the BCM and the viewer, that are crucial for centering the beam and ensuring optimal rejection and transmission. In the initial stages of commissioning during the H₂ beam run on July 27, 2018, a test of the performance of the BCM and viewer devices was done to identify the most efficient and precise of the two for beam centering during the initial tuning. Throughout this test, the currents in B1 and

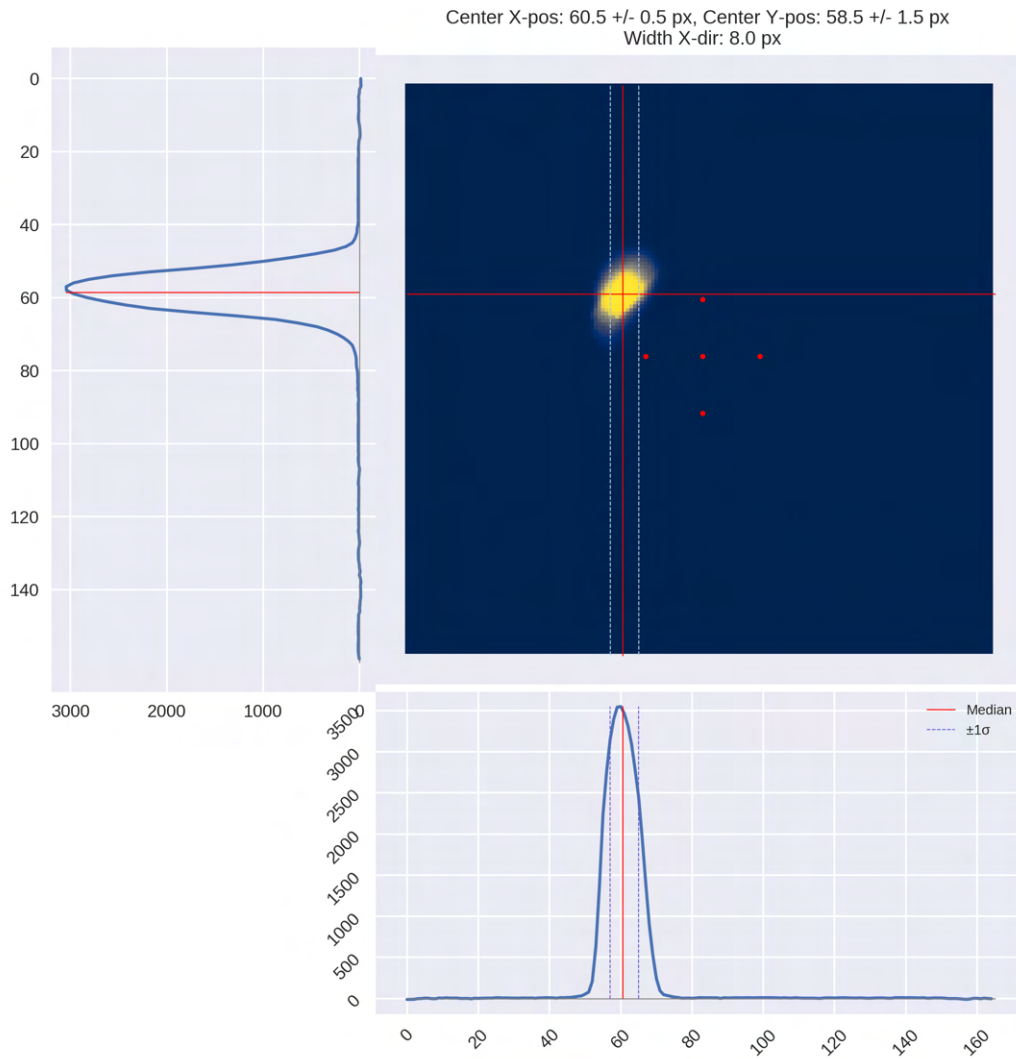


Figure 4.17: Viewer image analysis at FP1: Red lines indicate beam center as calculated from the median of the distribution, blue dashed lines indicate the width in the x-direction defined as $\pm 1\sigma$. The locations are indicated in pixels, and the scale is 5 mm to 16 pixels.

B2 were increased slowly from 110.56 to 110.76 A in steps of 0.01 A, scanning the areas of Viewer2 and BCM1 horizontally at FP1. This scan corresponded to a 13.5 pixel change in position of the center of the beam on the viewer output, corresponding to approximately 2 mm along the viewer and BCM.

A viewer image was saved at each step for a total of 20 images during the scan. They were each background subtracted and resulted in a background-free beam spot image. The counts along the x-axis (long axis) were integrated to show a 1D Gaussian-looking peak. To compare this centering method with the BCM, the median data point along the integrated curve in the x-direction was taken as described above, with an error of 0.5 pixels, to find that the beam center crosses the center of the viewer between 110.67 - 110.68 A.

During the BCM testing portion of the test, a significant amount of noise was recorded on each plate, as seen in Figure 4.18. This issue contributed to a large error bar that was derived from the fluctuations and deviation from linearity of the archived BCM data. Moreover, the BCM plates occasionally read negative currents. Those current were divided over the readings of the adjacent plates in the analysis. The results, shown in Figure 4.19, indicate that within uncertainties, the BCM records the crossing of the sum of the left plates and the sum of the right plates between 110.67 - 110.71 A.

Comparing the BCM's ease of use and robustness in finding the center of any beam spot with the viewer's analysis method and results, it was determined that the viewer supersedes the BCM as the beam centering device of choice for initial tuning and optimizing the beam trajectory in SECAR independently of alignment and beam spot shape. It was later concluded that the noise seen in the BCM was partly due to the drive motor not shutting off when the devices are in place, in addition to some electronic noise that required some rewiring to resolve the issue. Nevertheless, the viewer remained the main choice for tuning in

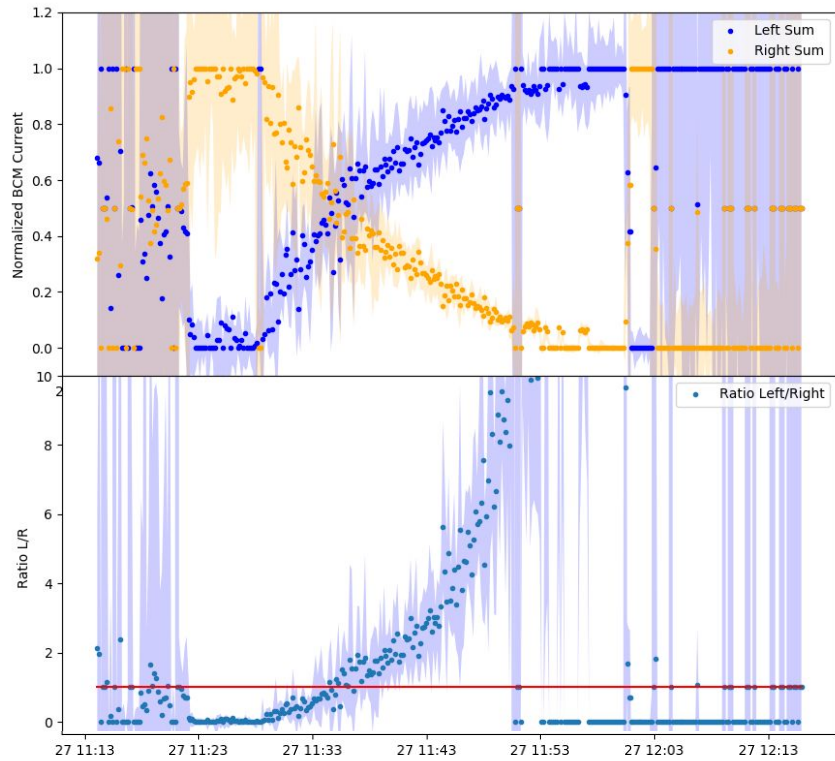


Figure 4.18: Top: Normalized currents on the left side (blue) and right side (orange) as a function of time. The point where they cross is the center region of the BCM. The uncertainty on the measurements is shown in the shaded region. Bottom: Ratio of left current to right current on the BCM. It should be equal to 1 when the beam crosses the center of the BCM.

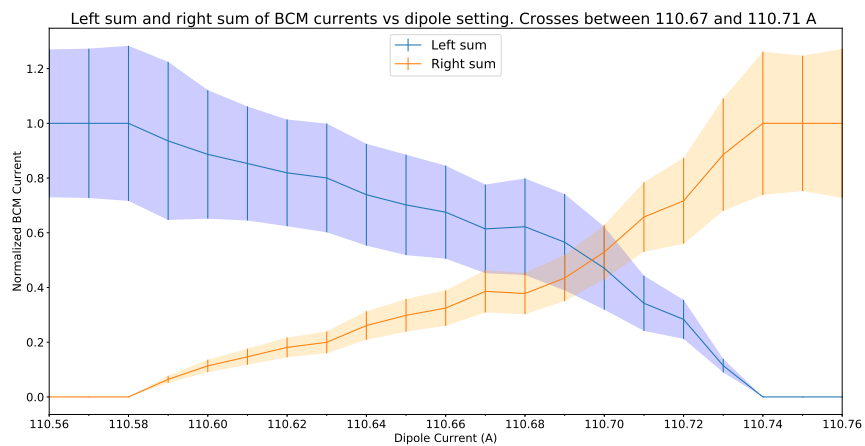


Figure 4.19: Final results showing the left side current (blue) and right side current (orange) as a function of dipole current. The shaded region of overlapping blue and orange between 110.67 and 110.71 A is the region when the beam was centered.

this work. In Chapter 5, a detailed walk-through of the beam tuning procedures is given, the methods of which will reinforce the decision of using the viewer as the initial beam centering diagnostic device for tuning via quadrupole steering due to the need to monitor the beam spot shape and location. In the future, the BCM may be useful for precision tuning of well shaped beams in dipoles and steerers, or the centering of non-attenuated or low intensity beams that can't be easily tuned with a viewer, provided the magnetic elements and the beamline are well aligned with the BCM center.

Chapter 5

Tuning and Bayesian Optimization

To achieve precision measurements, SECAR creates separation between unreacted beam and recoil particles of different mass but similar momentum by bringing both to a focus in two mass-dispersed planes along the separator. The separation goals require a centered recoil beam and finely tuned quadrupole fields to maximize the mass resolution and unreacted beam suppression of the device. The critical first step in establishing the correct ion optical setting is to center a pilot beam along the optical axis and adjust the quadrupoles and higher order elements to achieve the correct beam spot shapes, sizes, and foci at critical locations. The separator can then be scaled from the pilot beam setting to the recoil setting by scaling all magnets according to the $B\rho$ change. This chapter discusses the methods used to achieve an optimal tune that supports SECAR's separation goals, and presents the initial implementation of an efficient machine learning algorithm that allows for objective and precise tuning of the device.

5.1 Tuning Methods

A properly centered pilot beam along the beam line's ion optical axis is critical to achieve good transmission and provide a starting point to scale to the recoil rigidity. Although all SECAR electromagnetic elements were aligned to 0.2 mm and 0.01° to the nominal beam axis in the facility's alignment coordinate system, it is still necessary to experimentally confirm

that the beam is on the ion optical axis and not rely solely on space coordinates provided by the diagnostics such as beam viewers. This section describes the steps taken to align any incoming beam through the JENSA chamber into the SECAR beam line as well as the methods to tune the dipole bending magnets to align the beam through FP4 at the end of SECAR.

To ensure there is no deviation from the central optical axis, a tuning procedure was established making use of existing diagnostic and magnetic devices to indirectly probe the incoming beam angular deviation and center the beam in all SECAR magnets. This method uses the steering observed due to quadrupole magnets as a probe of the beam's deviation from the magnetic axis. In a quadrupole magnet, a particle feels a force proportional to the distance from the central axis (Lorentz force, Equation 1.2), where the net force is zero. When the incoming beam is aligned with the central optical axis of a quadrupole magnet, changes in the quadrupole strength should only focus and de-focus the beam distribution in the x- or y-direction depending on the polarity of the quadrupole. If there is some deviation from the axis, the beam will feel imbalanced forces from the quadrupole fields and is caused to steer in one direction or the other as the quadrupole strengths varies. Based on this behavior, the tuning procedure for the incoming beam was developed using the SECAR quadrupoles for probing deviations of the beam from the optical axis. The two ReA3 steerer pairs at BTS34:D1413 and D1431 (see Figure 5.1) are employed to adjust the angle and position of the beam impinging on the target. If the beam is deviated from the central ion optical axis, movements of the beam spot are observed on one of the viewers installed at some distance downstream when quadrupoles are varied upstream. The SECAR layout in Figure 5.1 displays all viewers used in this chapter for this purpose. In addition to centering the beam, this method ensures quadrupoles can later be adjusted without shifting the beam's

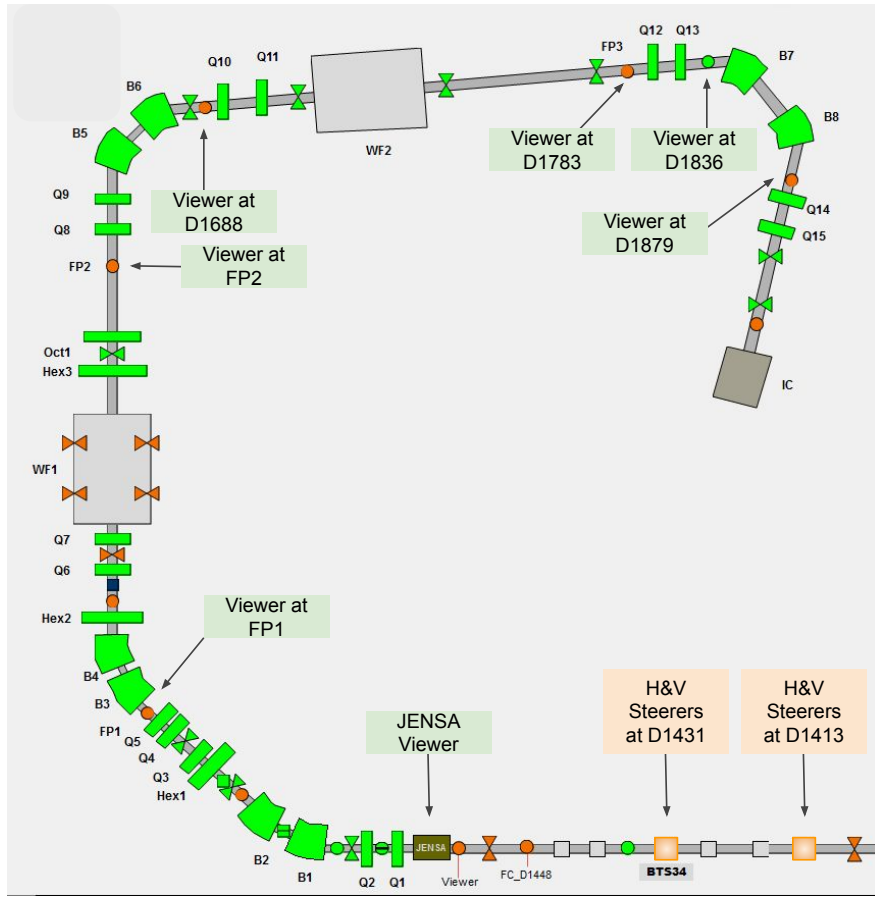
position and limiting transmission.

Prior requirements

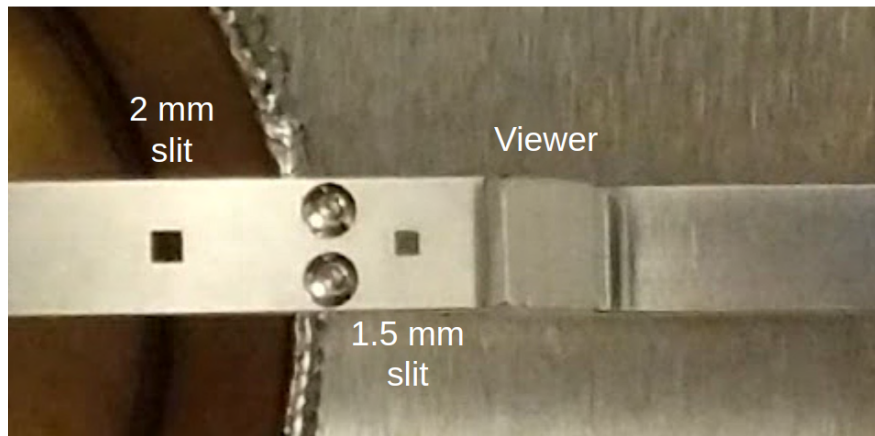
Before initiating any beam tuning in JENSA/SECAR, the incoming beam tuned by the ReA3 operators must meet certain requirements. The beam spot size at the JENSA target, visible through the viewer installed in the target chamber as shown in Figure 5.1 (b), should be restricted to 1.5 mm. This is accomplished by maximizing transmission through 2×2 mm and 1.5×1.5 mm apertures available on the same drive as the viewer. Transmission is measured from the last ReA3 section upstream of SECAR using the last ReA3 Faraday cup (FC_D1448) and the first SECAR cup (FC1) after Q2. The copper apertures installed in the upstream and downstream JENSA cubes as discussed in Chapter 3 (see Figure 3.9) can read current when beam is hitting them, and they serve as further diagnostics for the operators as they adjust the tune, minimizing any current reading on those apertures while maximizing the transmission between the two cups on both sides of the chamber. The restrictions imposed by those apertures guarantee a maximum incoming angle of ± 3.4 mrad. During this part, the operators tune the ReA3 dipoles and multipoles, but leave the two horizontal and vertical steerer pairs upstream of JENSA, shown in Figure 5.1, set to zero. Once these requirements are met, the tuning using SECAR diagnostics and magnets begins, utilizing those ReA3 steerers as needed.

5.1.1 Manual Tuning Procedure

In this section, the method is described as used with the first two quadrupoles, Q1 and Q2, and the viewer at FP1. The same method applies for any suitable combination of quadrupoles and downstream viewers along the SECAR beamline. The procedure below outlines the steps taken to manually adjust the incoming beam angle, and subsequently tune



(a)



(b)

Figure 5.1: (a): SECAR layout with notable diagnostics used for tuning, including the upstream ReA3 beamline with the two steerer sets used for correcting the incoming angle. The first set is 7.2 m away from the first SECAR quadrupole, and the two sets are 1.8 m apart. (b): JENSA viewer and slits used in the manual tuning procedure.

the SECAR dipoles.

Step-by-Step Tuning Procedure

1. The quadrupoles are set to their nominal tune scaled from the standard COSY map to the appropriate $B\rho$ (see COSY map in Table 3.2).
2. The dipoles are scaled according to $B\rho$ and the NMR probes in B1 and B2 are matched to readback values within 10^{-5} T, while checking that the beam is approximately centered on the viewer at FP1. Then the dipole magnets are cycled to ensure reproducible fields when setting them later on.
3. With Q1 and Q2 at their nominal values and Q3 to Q5 off, the location of the beam spot center at the FP1 viewer is recorded (found either manually or through the automated image analysis program discussed in Section 4.3.1).
4. Q1 is set to half its original value (this was chosen for convenience, however any value away from the nominal that produces visible changes in the beam on the viewer is acceptable and does not change the effectiveness of the method). If the beam moves from its previously recorded position at FP1, the downstream ReA3 steerer set (D1431) is adjusted so that the beam position at the FP1 viewer goes back to the position recorded with the nominal Q1 setting.
5. Q1 is set back to nominal. Looking at the JENSA viewer, the upstream steerers (D1413) are adjusted to re-center the beam on the JENSA viewer, if needed.
6. The beam current readings on the downstream and upstream JENSA apertures are checked to verify that the previous step did not change the incoming beam angle too

much. If the apertures are reading current (more than 10% of the total beam current), the last steerer changes are reversed step by step until the current is less than 3 pA.

7. Steps 3 - 6 are repeated until there is no steering at FP1 due to Q1 (or the minimum possible steering) and no or minimal current readings on the target apertures.
8. The same steps are repeated with Q2, until both Q1 and Q2 do not steer (or steer minimally).
9. If the procedure is not converging to a setting where steering is minimal or decreasing without loss in transmission, the steerers are set back to zero and the procedure is repeated using the steerers in reverse: downstream steerers to center on the JENSA viewer and upstream steerers to center on FP1.
10. Once the beam is centered along the quadrupoles' ion optical axis, the dipoles pair is tuned. The steering effects in the x-direction of Q3, Q4 and Q5 after the dipoles are checked using a similar procedure to the one used with Q1 and Q2. Going down in current, B1 and B2 are adjusted simultaneously as needed until the beam does not steer when Q3 - Q5 are varied in strengths. This ensures the beam leaves the dipole pair and enters the quadrupoles along the ion optical center. If there is a need to go back up in current, the dipoles are cycled again.
11. If there is steering due to Q3 - Q5 in the y-direction, this is corrected using only the ReA3 vertical steerers following the same procedure as Q1 - Q2 utilizing the JENSA and the FP1 viewer. No SECAR elements are able to provide vertical adjustments.

The procedure has to be repeated at every viewer to fine tune any small angular deviations that are magnified downstream and each dipole pair has to be set in the same manner to

ensure a well centered beam up to the end of SECAR, making this manual procedure operator dependent and very time consuming. A faster and more robust method was needed to tune the entire separator. This led to the automation of most of the procedure as is described next for horizontal beam centering using the dipoles and in Section 5.3 for adjustments of the incoming beam position and angle using the ReA3 beamline steerers.

5.2 Dipoles and WF Tuning

Tuning dipoles in pairs is challenging as small field differences can introduce angles when leaving the pair. Each pair in SECAR has to be carefully cycled and their field readbacks matched to 10^{-5} T (using NMR probes for B1 - B2 and Hall probes for B3 - B8) before finding the correct field setting to center the beam in the dipoles. To accelerate the tuning procedure and make it more reproducible, a simple automated scan over the corresponding viewer for each pair was implemented to find the least steering path through the quadrupoles located between each dipole pair and a viewer downstream.

As an example, the steps below describe the automated scan for the case of B1 and B2 with the beam position monitored at the FP1 viewer:

1. The selected dipoles are set to a current that is significantly higher than the expected setting and positions the beam near the low bending radius edge of the viewer.
2. The automated scan is run. This prompts the cycling of the dipoles following the procedure outlined in Chapter 4.
3. Once settled, dipole field readbacks are matched by the automated script down to 10^{-5} T by decreasing the current in small steps as needed.

4. A series of images is taken of the beam spot at the FP1 viewer at four different quadrupole tunes varying only Q3 - Q5, as these quadrupoles are downstream of B1 - B2 and upstream of FP1. The quadrupole strengths at the four different tunes are selected beforehand with the only criterion being a change that keeps the beam spot visible (not too unfocused) on the viewer. In this case the tunes typically are: Q3 - Q5 at nominal, Q3 at -90 A with others at nominal, Q3 at two-thirds of its nominal strength with others at nominal, and Q4 at two-thirds of its nominal strength with other at nominal.
5. The steering distance is calculated from the mean distance between the beam centers of the four tune images taken using the viewer image analysis tool described in Section 4.3.1.
6. The dipole currents are simultaneously decreased by a step size specified by the operator (typically 0.06 to 0.02 A).
7. Step 3 - 6 are repeated.
8. Once the beam reaches the other end of the viewer, the script is halted and the steering distance as a function of dipole fields is plotted.
9. The curve is fit with a second degree polynomial, and the corresponding best magnetic field range is found by the magnetic field corresponding to the lowest steering value of the best fit and its corresponding uncertainty.
10. The dipoles are set to the best field values after cycling and matching the NMR probes again.

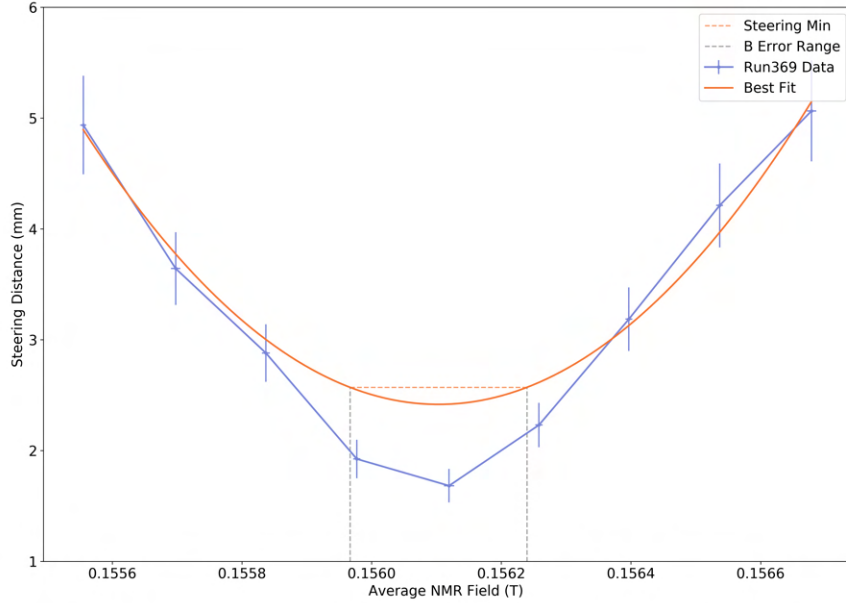


Figure 5.2: B1 - B2 dipole scan in steps of 0.06 A on FP1 to minimize steering in Q3 - Q5. The steering does not reach zero in this case, and this may be due to small deviations of the beam from the center that are not corrected at FP1. Fine tuning downstream where sensitivity to such small deviations is increased is often needed.

Figure 5.2 shows the average steering distance due to Q3 and Q4 (varied as detailed above) as a function of the NMR field value in B1 - B2. This scan was done in steps of 0.06 A to find the region of least steering, then fine tuned with smaller steps of 0.02 A as shown in Figure 5.3. The error on this steering distance was calculated to be $\sim 10\%$ from propagating the ± 1.5 pixel error on each x and y position corresponding to the accuracy in finding the median of the beam profile projected onto each axis (refer to the viewer image analysis in Chapter 4). The error on the magnetic field took into account the difference in field measurements between B1 and B2 which was at least 10^{-5} T and occasionally higher when small drifts occurred after matching them.

The WF dipoles are tuned in a similar fashion after setting the electrodes to the appropriate high voltage settings for the beam being tuned. These are simpler to tune as there is only one dipole magnet per WF. The quadrupoles Q8 and Q9 installed downstream of WF1

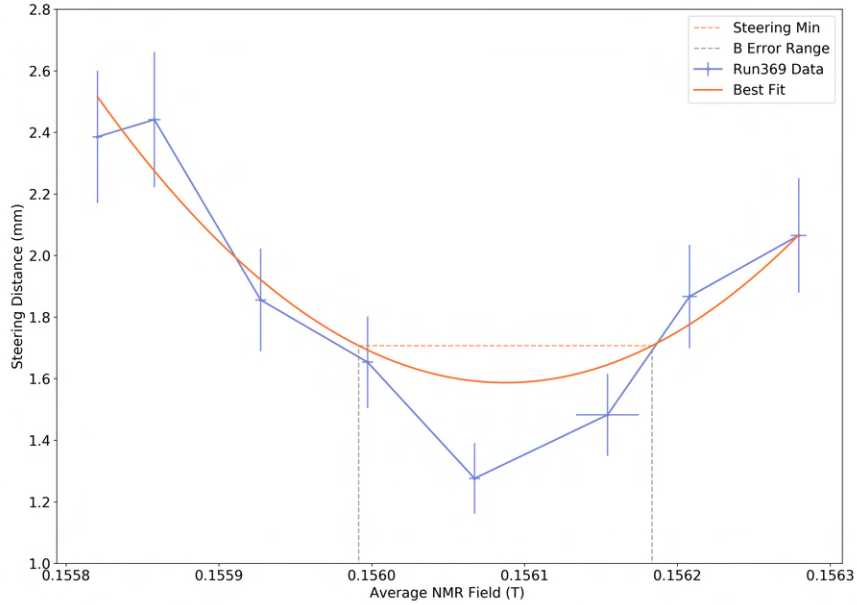


Figure 5.3: B1 - B2 dipole scan in steps of 0.02 A on FP1 to minimize steering in Q3/Q4.

and before B5 - B6 are used to correct the angle of the outgoing beam from the WF1 magnet using the viewer at location D1688. The viewer at D1783 at a larger distance can also be used when higher sensitivity is needed. Figure 5.4 shows the steering in the x-direction measured in Q8 and Q9 as a function of the WF1 dipole field at the viewer at D1688. Any vertical steering observed at this point has to be adjusted by fine tuning the vertical steerers in ReA3 at these viewers. Only WF1 was installed during the commissioning discussed in this work, however once installed WF2 will be tuned as described for WF1 using Q12 - Q13 at the viewer downstream of B8 (D1836).

5.3 Bayesian Optimization for Beam Tuning

Although the JENSA apertures allow the incoming angle of the beam to be limited to 3.4 mrad, SECAR requires smaller angles for optimal performance. As seen in the previous section, having different operators tune SECAR to that requirement manually is a time

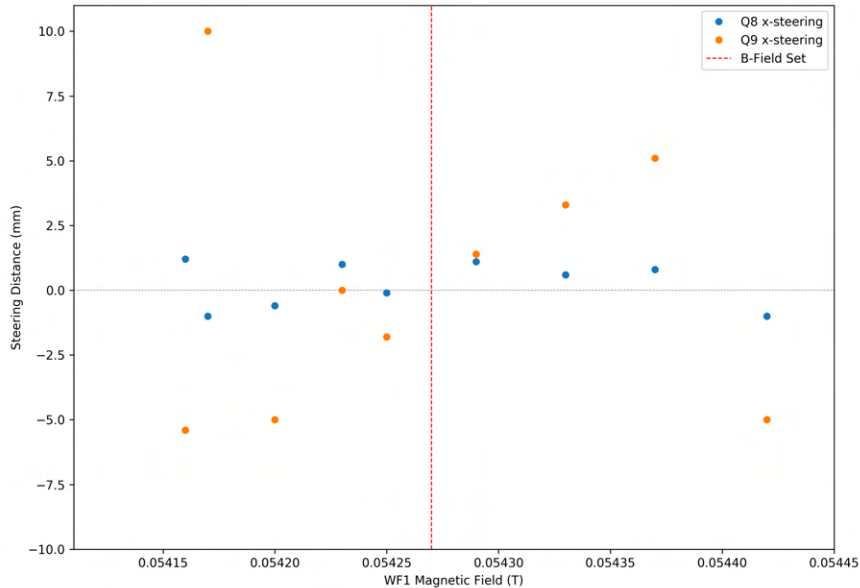


Figure 5.4: WF1 dipole magnet scan to minimize steering in Q8 and Q9 measured at D1688. The best field corresponding to the beam leaving the WF at the center is shown by the red dashed line.

consuming task that introduces bias and often leaves the separator in a sub-optimal non-reproducible state. An automated online Bayesian optimization was shown to efficiently tune the beam in SECAR during commissioning operations in 2020 thereby ensuring objective measures of tune quality and leaving the machine in a reproducible state that provides an optimal beam for maximizing the separator’s performance. In this section, the Bayesian approach is described and results from the first beam tests are presented.

5.3.1 The Bayesian Approach

A Bayesian optimization is a gradient-free global maximizer (or minimizer) of an unknown black-box function f . Each observation of f in the domain is unbiased and possibly noisy, and constitutes a part of prior data collected that informs the decision of where to place the next evaluation by applying Bayes’ theorem. The theorem describes the probability of an event based on prior knowledge of conditions that might be related to the event. This

method is an iterative search for a better optimum, making it a sequential optimization algorithm. It imposes a probabilistic distribution over the objective function values and its corresponding input axes to find the distribution of the function value at any new point in the domain. This is then used to choose a better optimum, and once the sample of observation is collected at that point, the procedure is repeated. The Bayesian optimization is essentially an interplay of two components. The first one is the underlying probabilistic model of the objective function, e.g. a Gaussian process. The second key component is the choice of acquisition function that places the criterion on how to choose the next point. Thorough introductions to Bayesian optimization can be found in [13, 86].

This approach is often taken when the function f is expensive to evaluate, for example due to computational limits of simulation codes. In the case of SECAR, thorough beam physics simulations incorporating the accelerator beamline upstream are not yet available and may not be sufficiently accurate. Given the high dimensionality of the system, a robust optimization of the experimental system is needed to validate and improve on the theoretical COSY parameters. With a proper surrogate model of the beam response in SECAR to changes in beamline parameters (magnet settings in SECAR and upstream), a Bayesian approach presents a good choice for addressing these issues while decreasing the time spent tuning and eliminating the bias introduced by operators.

Bayesian Priors

In the Bayesian formalism, samples from the true function are used to construct an estimate of the probabilistic model, i.e. the surrogate model. This surrogate can be used to model the true function and to select which observations are to be made next by applying Bayes' theorem. As there might be an infinite number of possible functions that could be consistent with the data, priors need to be imposed to inform the model on what is known

about the true function, e.g. smoothness, or variability. Assuming a noisy observation y that depends on an unknown parameter w given an input variable x

$$y = wx + \epsilon \tag{5.1}$$

with $\epsilon \sim \mathcal{N}(0, \sigma_n^2)$ as the stochastic noise in the observation y , a prior distribution $p(w)$ is defined on the parameter w . Probabilities based on the observed data are then computed as such

$$p(w|y, X) = \frac{p(y|X, w) \times p(w)}{p(y|X)}, \tag{5.2}$$

following Bayes' Rule

$$\textit{posterior} = \frac{\textit{likelihood} \times \textit{prior}}{\textit{marginal likelihood}} \tag{5.3}$$

where $p(w)$ represents the initial guess of the probability of w , and $p(y|X, w)$ is the likelihood that y is observed given X and w . The posterior $p(w|y, X)$ then contains information from both the data and prior distribution. Given a set of observations (y, X) , the probability that a new observation at position x_* will result in observation y_* can be calculated as

$$p(y_*|x_*, y, X) = \int p(y_*|x_*, w)p(w|y, X)dw. \tag{5.4}$$

This is referred to as the predictive distribution and it is given by weighting all possible predictions by their calculated posterior distribution to find the function value at some point x_* . Assuming the prior and the likelihood to be Gaussian, the predictive distribution is also Gaussian with a mean and variance corresponding to the predicted value of y_* .

5.3.2 Gaussian Processes

Gaussian processes are popular in Bayesian modeling for regression and classification. They are easy to implement, flexible and conveniently provide uncertainty estimates along with their predictions. A Gaussian process defines a distribution over functions, a generalization of the Gaussian probability distribution which describes random variables (scalars or vectors). In this work, a Gaussian process method for regression is described as applied to the tuning of SECAR. For a review on Gaussian processes, see [79]. Formally, a Gaussian process is a stochastic process with all of its finite-dimensional distributions being joint Gaussian distributions. In the bivariate case, taking a 2D joint Gaussian distribution with two normally distributed and correlated variables x_1 and x_2 with covariance matrix elements $\Sigma_{12} = \Sigma_{21} = 0.7$, the conditional probability of one of the variables can be derived given the other, as a measurement in one dimension (x_1 for example) will constrain the distribution of the other (x_2). This example is illustrated in Figure 5.5 where the 2D joint Gaussian probability density function of x_1 and x_2 is shown in blue with mean $\mu_1 = \mu_2 = 0$ and covariance Σ , and the probability of x_2 given a measurement of $x_1 = 1$ and given the distribution parameters $\Theta = ([0, 0]^T, \Sigma)$ is shown in the black solid line. Analogously to Bayes' rule in Equation 5.3, this conditional probability can be expressed in terms of the marginal distributions and the joint density distribution. In a Gaussian process, the posterior can be similarly expressed from the prior and the observations at all sampled input values to find the joint probability of all values of the unknown function f for all the input values in the domain. The Gaussian process then returns the mean and variance of a normal distribution over the possible values of f at any given input location in the domain.

Just as a Gaussian distribution is completely described by its mean and covariance, a

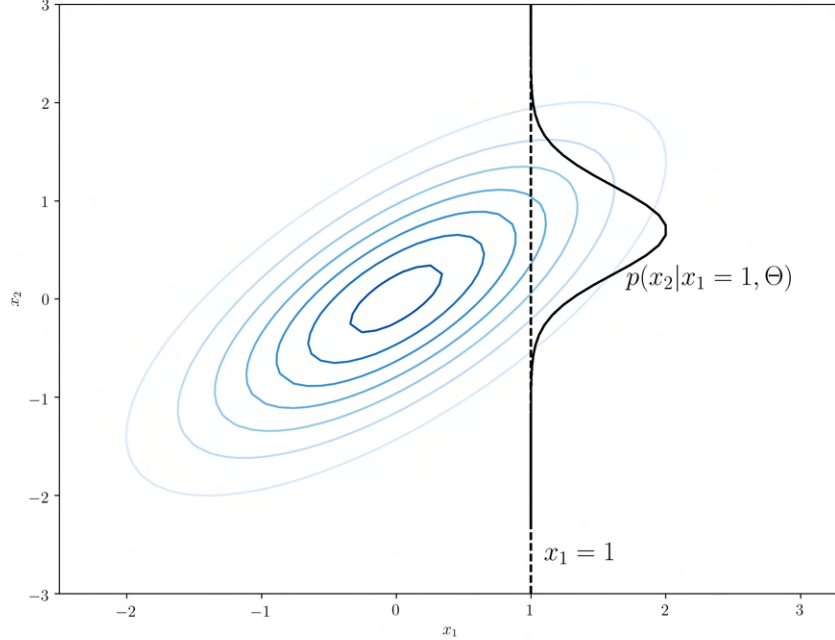


Figure 5.5: Conditional probability of x_2 given x_1 .

Gaussian process is completely specified by its mean function m and covariance function k :

$$f(x) \sim \mathcal{GP}(m(x), k(x, x')) \quad (5.5)$$

where

$$m(x) = \mathbb{E}[f(x)] \quad (5.6)$$

and

$$k(x, x') = \mathbb{E}[(f(x) - m(x))(f(x') - m(x')))]. \quad (5.7)$$

In this work, the covariance function defines the beam's response to changes in the input settings of different magnetic elements in the beamline and was selected to be the popular squared exponential (SE) kernel. With this choice, the variance is close to unity for variable with close inputs, and decreases with increasing distance between inputs. The SE function is

infinitely differentiable and thus is very smooth, a good model for beam response to magnetic field changes. The covariance function was defined as

$$k_{SE}(x_p, x_q) = \sigma_f^2 \exp\left(-\frac{|x_p - x_q|^2}{2\ell^2}\right), \quad (5.8)$$

where σ_f^2 is a scaling parameter that represents the output variance, and ℓ is the characteristic lengthscale parameter, a positive constant that roughly describes the distance that can be covered in the input space before points become correlated. Since experimental data represents a noisy version of the black box function, an independent and identically distributed Gaussian noise term ϵ with variance σ_n^2 is added as done in Equation 5.1, and the noisy observations become $\mathbf{y} = f(\mathbf{x}) + \epsilon$. The final form of the covariance function is given by

$$\text{cov}(y_p, y_q) = k_{SE}(x_p, x_q) + \sigma_n^2 \delta_{pq}, \quad (5.9)$$

where the Kronecker delta δ_{pq} is 1 for $p = q$ and zero otherwise. The signal variance σ_f^2 , the lengthscale ℓ , and the noise variance σ_n^2 parameters are free parameters known as *hyperparameters*. The covariance function learns them empirically from prior observed data through maximizing the log marginal likelihood with respect to the hyperparameters. The choice of hyperparameters is important as it has a significant effect on the quality of the Gaussian process predictions, and is discussed more in Subsection 5.3.3.

Assuming a prior that expresses the known beliefs about these parameters given n noisy observation points $\mathbf{x} = \{x_{1:n}\}$, taking the prior mean to be zero $m(\mathbf{x}) = 0$ without any loss of generalization, the prior covariance matrix is defined as

$$\text{cov}(\mathbf{y}) = \mathbf{K}(\mathbf{x}, \mathbf{x}) + \sigma_n^2 \mathbf{I} \quad (5.10)$$

following Equation 5.9. The matrix \mathbf{K} is written as

$$\mathbf{K} = \begin{bmatrix} k(x_1, x_1) & \dots & k(x_1, x_n) \\ \vdots & \ddots & \\ k(x_n, x_1) & & k(x_n, x_n) \end{bmatrix} \quad (5.11)$$

with k as the SE kernel given in Equation 5.8. Consequently, the prior given noisy data can be expressed as

$$\mathbf{y} \sim \mathcal{N}(0, \mathbf{K} + \sigma_n^2 I). \quad (5.12)$$

Given a new observation at x_* , the prior \mathbf{y} and the output f_* are jointly Gaussian and the joint prior distribution is

$$\begin{bmatrix} \mathbf{y} \\ f_* \end{bmatrix} \sim \mathcal{N}\left(0, \begin{bmatrix} \mathbf{K} + \sigma_n^2 I & \mathbf{k} \\ \mathbf{k}^T & k(x_*, x_*) \end{bmatrix}\right) \quad (5.13)$$

where

$$\mathbf{k} = [k(x_*, x_1) \quad k(x_*, x_2) \quad \dots \quad k(x_*, x_n)]. \quad (5.14)$$

To get the posterior distribution over functions, the conditional distribution can be derived from the joint prior distribution on the observations (see [79] for details):

$$p(f_* | \mathbf{x}, \mathbf{y}, x_*) = \mathcal{N}(\mu(x_*), \sigma^2(x_*)), \quad (5.15)$$

where f_* is the noise free predictions,

$$\mu(x_*) = \mathbf{k}^T (\mathbf{K} + \sigma_n^2 I)^{-1} \mathbf{y} \quad (5.16)$$

and

$$\sigma^2(x_*) = k(x_*, x_*) - \mathbf{k}^T (\mathbf{K} + \sigma_n^2 I)^{-1} \mathbf{k}. \quad (5.17)$$

The predictive distribution of the Gaussian process is completely described by the posterior mean $\mu(x_*)$ and variance $\sigma^2(x_*)$. Note that the latter only depends on the inputs, as expected for a Gaussian distribution.

5.3.3 Hyperparameter Selection

Since a Gaussian process model is a non-parametric model, its power lies in the crucial choice of the covariance function k , also known as the kernel function, as it determines most of the generalization properties of a Gaussian process model (e.g. smoothness, periodicity, linearity, etc). Therefore the important model parameters are the quantities used to parameterize the covariance function. For the selected SE kernel function defined in Equation 5.9, three parameters, the observation variance σ_f^2 , the noise variance σ_n^2 , and the lengthscale ℓ can be freely varied and constitute the hyperparameters of this model. The settings of these parameters ultimately determine how well the Gaussian process model will capture the features of the objective function being optimized. For instance, Figure 5.6 shows the effect of the lengthscale ℓ on the SE kernel, highlighting the importance of the choice of hyperparameters based on the properties of the function being modelled - the smoothness in this case. Typically the hyperparameter values are learned as samples are collected with every iteration by maximizing the log-likelihood of the observations, essentially providing a measure of the likelihood of the data given the model hyperparameters. To increase the efficiency of this learning process, an informative prior on the hyperparameters can be defined given some known properties of the function being sampled (function smoothness related to

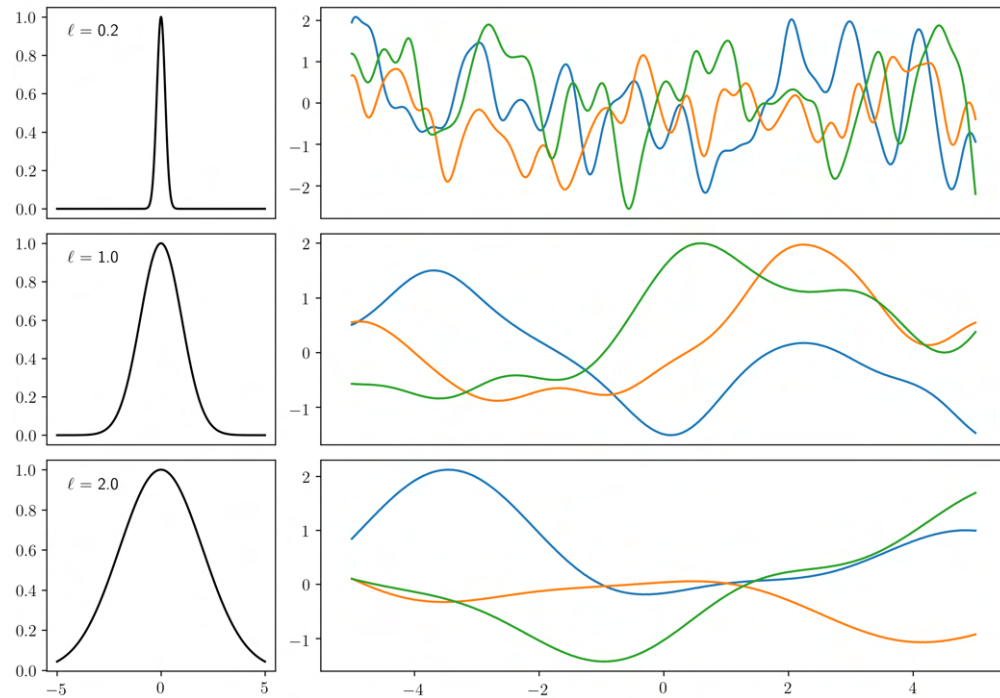


Figure 5.6: The effect of the lengthscale hyperparameter on the SE kernel from Equation 5.8 for $\ell = 0.2, 1, 2$. For each hyperparameter value, the function $k_{SE} = (0, \mathbf{x})$ is shown on the left and random samples from the Gaussian process prior are shown on the right.

the underlying beam physics for example). For an in-depth review on model selection for Gaussian process regression and marginal likelihood for hyperparameter selection, see [79].

In this work, the observation variance σ_f^2 is set and optimized by maximizing the log marginal likelihood with respect to the variance. For the lengthscale ℓ and the noise term σ_n^2 , a Gaussian prior with an appropriate mean and standard deviation was initialized for each at the beginning of every run. The initial values were set based on previous tuning experience and empirical data which made apparent the localized and smooth nature of the beam response to changes in the beamline. If the beam had some instability coming from upstream of SECAR and was moving on the viewer while all SECAR magnets were stable, the prior on the noise hyperparameter was increased accordingly (usually on the scale of 0.5 - 1 mm). Similarly, the lengthscale prior was adjusted according to the beam spot

position's sensitivity to changes in steerer currents. Subsequently the marginal likelihood was maximized with respect to each parameter at every new iteration. As will be seen in the next sections, both hyperparameters varied between tunes and at different locations in the beamline, making an empirical optimization using the sampled data the best option currently available to properly select the model's hyperparameters.

5.3.4 Acquisition Functions

The goal of a Bayesian optimization is to find the globally optimal solution in as few function evaluations as possible. This can be done through a utility function that, based on the collected data, estimates which unobserved sample point has the most potential to result in a maximum. The function determining at what point to evaluate the objective function next is called an *acquisition function* $a(x)$. High values in the acquisition function correspond to high values of the objective function. Simply maximizing $a(x)$ to find the next sampling point,

$$x_{next} = \operatorname{argmax} a(x), \tag{5.18}$$

is relatively easy to optimize as it depends only on the probabilistic model described by the posterior distribution derived in Equation 5.15.

There are two methods of searching for the next point with the highest potential for improvement on the current maximum. One method is to look near points with a high posterior mean $\mu(x)$ - called *exploitation*, and the other is to prefer points with a high posterior variance $\sigma^2(x)$ to explore away from known regions - called *exploration*. Exploiting too much runs the risk of getting stuck in a local optimum, while exploring too much means continuing to explore indefinitely even after finding a global optimum. The main property

that an acquisition function has to satisfy is the ability to trade-off between exploitation and exploration when choosing the next sampling point. The three most common types of acquisition functions are described briefly below.

Probability of Improvement

Initially introduced by Kushner et al. in 1964 [59], the *probability of improvement* (PI) function was the first acquisition function to be suggested. It selects the point with the highest PI over the current maximum $f(x^+)$ as the next query point and is defined for a normal posterior distribution characterized by $\mu(x)$ and $\sigma^2(x)$ as:

$$\begin{aligned} PI(x) &= P(f(x) \geq f(x^+)) \\ &= \Phi\left(\frac{\mu(x) - f(x^+)}{\sigma(x)}\right), \end{aligned} \tag{5.19}$$

where Φ indicates the cumulative distribution function (CDF). The disadvantage of this approach is that as given above, the PI is purely exploitative as $PI(x)$ will be large when $\sigma(x)$ is small. This can be remedied by adding a user-defined trade-off parameter $\kappa \geq 0$ to the function evaluation $f(x^+)$. With this modification, the PI selects the point most likely to provide an improvement of at least κ .

Expected Improvement

While the PI only looked at how likely is an improvement, a more complete function would additionally consider the magnitude of the improvement. The *expected improvement* function (EI) [71] chooses the next point as the point with the highest expected improvement over the current max $f(x^+)$. The EI expression for a posterior distribution with mean $\mu(x)$

and variance $\sigma^2(x)$ is

$$EI(x) = \begin{cases} (\mu(x) - f(x^+))\Phi(Z) + \sigma(x)\phi(Z) & \text{if } \sigma(x) > 0 \\ 0 & \text{if } \sigma(x) = 0 \end{cases} \quad (5.20)$$

with

$$Z = \frac{\mu(x) - f(x^+)}{\sigma(x)}, \quad (5.21)$$

where Φ and ϕ are the CDF and the probability density function (PDF) of the standard normal distribution, respectively. Similarly to the modification suggested for $PI(x)$, $EI(x)$ can be expressed in a more generalized form where a positive user-defined trade-off parameter κ is added to $f(x^+)$ [63].

Lower Confidence Bound

A *lower confidence bound* (LCB) acquisition function [24] is constructed from the Gaussian process posterior mean function $\mu(x)$ and its standard deviation $\sigma(x)$ and is a simple heuristic balancing of exploration and exploitation:

$$LCB(x) = \mu(x) - \xi\sigma(x), \quad (5.22)$$

where the term ξ is a positive user-defined exploration weight that defines the desired amount of exploration in regions of large uncertainty. The LCB is minimized (instead of maximized as in the case of the previously mentioned acquisition functions) and the next measurement is chosen to be sampled at that minimum and added to the GP. An analogous acquisition function, the *upper confidence bound* (GP-UCB), can be used for maximization problems instead. One disadvantage with this method is that the choice of exploration weight ξ will

depend on each specific application and may not always be straightforward to set.

In this work, a lower confidence bound (LCB) acquisition function with user defined exploration weight ξ was employed to select the next observation points. This choice presents a direct way to balance exploitation and exploration and a simple bound on how close each point is to the minimum.

5.3.5 Method and Algorithm

Implementing an online Bayesian approach to tuning SECAR required the integration of several parts, including the control system for the magnets being tuned, extraction of observations through diagnostics devices, and running the optimization program online during experiments. To facilitate communication between the optimization program and the control system described earlier in Section 4.1, PyEpics, a Python interface to the EPICS Channel Access (CA) library for the EPICS control system [73], was used. The Python GPy library [39] and the associated GPyOpt [92] tool were used for the Bayesian optimization and the Gaussian process framework, respectively. The viewer analysis tool discussed in Section 4.3.1 was used to generate the observations needed for the algorithm when sampling the unknown function. Although the diagnostic device was the same, the evaluation of the objective function at the viewer was different for each of the two optimizations described in this work. The beam incoming angle optimization was concerned with the steering of the beam measured at the viewer as is explained in detail in Subsection 5.3.6, and the ion optics optimization was modeling an objective function that depended on the beam spot's location and width in the x- and y- direction as is presented in Subsection 5.3.7.

While the objective function and the implementation varied depending on the optimization goal, the general algorithm remained the same and is described in Algorithm 1. Before

Algorithm 1 General Bayesian optimization algorithm for SECAR tuning.

- 1: Randomly select initial sampling point and evaluate objective function
 - 2: **while** some stopping criterion is not met **do**
 - 3: Maximize the acquisition function using the posterior mean and variance under the set exploration weight set to find next sampling point
 - 4: Evaluate the objective function at the selected point
 - 5: Add new observation to set of samples
 - 6: Select the minimum of the objective function evaluations to be the final tune
-

every optimization run, priors on the hyperparameters were defined before initializing the algorithm. As the beam tune quality varied throughout the different experiments, the prior on the noise term σ_n^2 in the covariance function was defined each time as a Gaussian with a mean and standard deviation that best described the noise observed in the viewer images, typically $\sigma_n^2 \sim \mathcal{N}(1, 0.5)$ (in units of pixels²). The prior on the lengthscale of the kernel chosen for the Gaussian process as defined in Equation 5.8 was also chosen to be of Gaussian form with a mean and standard deviation that best described how quickly the beam optics changed with changes in magnet settings, and varied from run to run. These parameters were empirically defined after observing the behavior of the beam in previous tuning runs and selecting the values that maximize speed of convergence to a global minimum. The exploration weight ξ was typically around 0.5, up to 3 when the domain covered by the magnets being optimized was large. After initializing the priors on the hyperparameters, the GPy software package automatically updated the priors at each iteration based on past observations.

In the early stages of developing this tuning code, the Gaussian process functions were explicitly defined and the algorithm was developed without the use of any external package for the framework. At that time, no automated marginal likelihood maximization was yet implemented for updating the hyperparameters and it was necessary to manually adjust

the lengthscale and noise when needed. Later on, the GPy library was adapted due to the ease of use of the frameworks and accessibility to useful features including setting priors on the hyperparameters and the capability of automatically adjusting those priors as more observations are sampled. It also offered a higher computational efficiency, allowing for hundreds of samples to be gathered in minutes, the only real bottleneck remaining being the time it takes for the magnets to settle at new current values before images of the new beam positions can be taken.

5.3.6 Beam Incoming Angle Optimization

The main drivers behind the need for an efficient automated solution that led to the implementation of a Bayesian approach to tuning were the subjectivity and the variable efficiency and capabilities of each operator during manual tuning. A new procedure based on the manual one detailed in Subsection 5.1.1 was devised based on Algorithm 1. The steps including centering the beam on the JENSA viewer and the FP1 viewer, as well as checking the transmission through the JENSA apertures (current readings) were not included in the automated procedure but were always checked manually at the end. Although a feedback from current readings along the system could be incorporated into the objective function, there currently seems to be little evidence that such a check is needed based on the successful experimental runs, as the algorithm is already able to find an optimum that allowed for full transmission through the system.

This optimization utilizes the quadrupoles' steering effects on the beam particles when some incoming beam angle with respect to the magnets' optical axis is present, similarly to the manual tuning method. It can be done using any combination of quadrupoles and downstream viewer. For simplicity, in the following discussion only Q1 and Q2 will be

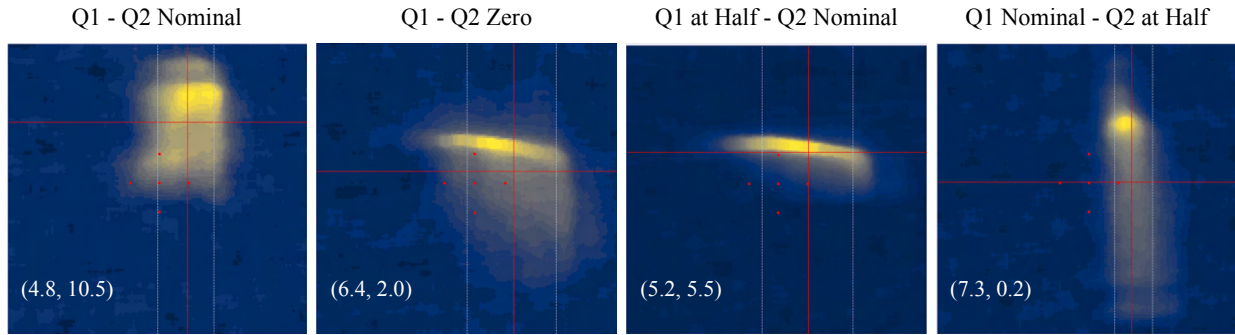


Figure 5.7: Sampling of an observation at the viewer. Four images taken at different quadrupole tunes are shown with the beam center location with respect to the central red dot in mm. The mean steering distance between the four beam spots is 4.7 mm.

considered paired with the FP1 viewer. A selection of four different quadrupole current settings were chosen for Q1 and Q2 so the beam spot changes were visible on the viewer. Typical settings were: both at nominal, both at zero, Q1 at half of the nominal while Q2 was at nominal, and vice versa, while Q3 - Q5 remain at zero to avoid deflection due to B1 and B2. However the current settings for Q1 and Q2 can be changed according to beam behavior with no noticeable effect on the speed or effectiveness of the method. The algorithm samples the objective function by taking four images at that viewer at the four different quadrupole settings. The centers of the beam spot at each setting is then computed, and the average distance between the four is returned as the value of the new observation y . This sampling process is demonstrated in Figure 5.7. The unknown function that is being minimized is then the average steering distance as a function of the four ReA3 steerer settings. The acquisition function is computed and minimized using the posterior mean and variance that included the new observation, and the next step (next four current values for the steerers) is selected and sampled. This iterates continuously as the algorithm explores a defined phase space of the steerer settings and samples the regions with highest probability of minimizing the mean steering value. The full procedure for tuning into the SECAR beamline using Q1 and Q2 at

FP1 is outlined below.

Step-by-Step Automated Tuning Procedure

1. The ReA3 operators tune the beam through the target chamber by maximizing the current read on FC1 through the JENSA 1.5 and 2 mm slits and keeping aperture readings at minimum. They also use the ReA3 quadrupoles to ensure a small (ideally 1.5 mm) beam spot at the JENSA viewer. This is done while keeping the four upstream horizontal and vertical ReA3 steerers at zero current.
2. Q1 - Q2 are set to their nominal tune scaling from the standard COSY map to the appropriate $B\rho$, while the others are left at zero. The choice of the four settings used to sample the steering function is defined and is typically the same as shown in Figure 5.7.
3. The dipoles are set to the value corresponding to the $B\rho$ of the beam, however they are not typically set to an accurate and calibrated tune yet and the x-position of the beam is off from the true center - this has no effect on tuning the incoming beam angle.
4. The tuning script is initialized with the desired bounds on the currents for the four steerers, defining the phase space for the parameters (typically -15 to 15 A, smaller when fine tuning). The exploration weight of the acquisition function (around 0.5) and the Gaussian priors for the noise and the covariance function's lengthscale factor are also initialized to the desired starting values, typically $\mathcal{N}(1,0.5)$ for the noise and $\mathcal{N}(10,2)$ for the lengthscale (note that the lengthscale may have a mean as low as 1 A at sensitive locations).
5. The optimization code is run following Algorithm 1.

6. Once the average steering distance reaches a minimum (typically 1 - 2 mm), the code is manually stopped and the steerers are set to the currents corresponding to the least steering tune.
7. The steering effects due to Q1 and Q2, along with the beam spot position at the JENSA viewer, and the transmission including JENSA aperture readings are checked manually to confirm the quality of the tune.

If the steerer phase space is large, it can be narrowed down around the best settings found and repeated to fine tune with a smaller exploration weight if needed. Typically this is done at the next viewer along the beamline. Although much less decision making and time is needed on the part of the operator compared to the manual tuning, a critical manual task remains to make sure the images are of acceptable quality for useful data extraction, including checking for proper background image subtraction and that the beam is hitting the viewer. Early attempts suffered from the latter problem until a conditional limit on the threshold was added to the algorithm to automatically check if beam was present at each iteration. If the condition is not met, the algorithm skips the iteration and moves on to the next best steerer settings. While this procedure highlighted the steps taken to tune all four steerers concurrently, it is possible to tune any subset of those steers while keeping others fixed by simply adjusting the magnet list that the algorithm takes as input. This was done when steering along one of the axes (usually the vertical axis) only needed adjusting and a 2D optimization was sufficient.

A similar optimization procedure was performed at FP1, FP2 and at viewers downstream of FP2 using different sets of quadrupoles as shown in Figure 5.1. This was especially helpful when the steering on the vertical axis needed fine tuning, as the sensitivity to small

angles increases further downstream. A simple change in the script to indicate the desired quadrupoles and correct viewer location can be made to switch the image acquisition to whichever viewer is being used. The first step was always to adjust the beam angle into the first section of SECAR at FP1, and the optimization was repeated at any subsequent viewer where steering was observed as the beam was transported through SECAR with the corresponding upstream quadrupoles as probes for the incoming angle. In many cases, it was critical to optimize the steering in several quadrupoles at and past FP2 to obtain a good tune at the mass slits at FP2.

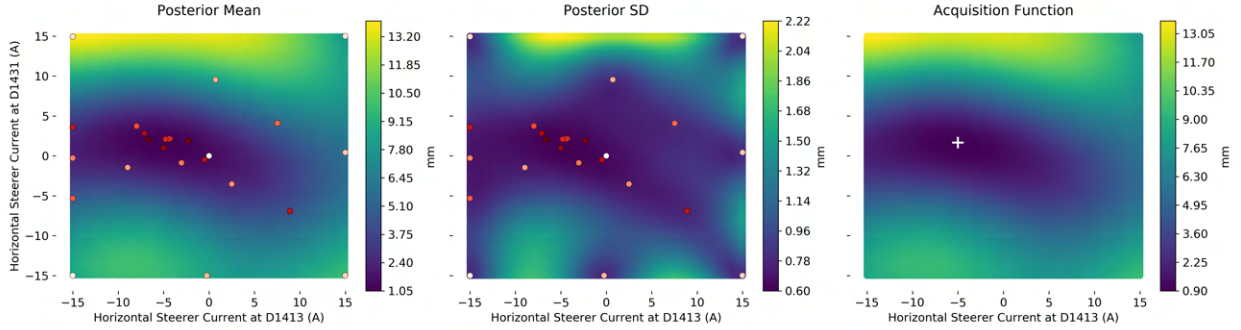
The general process to tune up to FP2 was as follows: After an on-axis tune was obtained at FP1, the dipoles pairs B1 - B2 and B3 - B4 and the WF1 were set following the tuning procedure described in Section 5.1.1. Once the beam was transmitted to FP2, the steering due to Q1 and Q2 was checked again at that location, in addition to any steering in the vertical direction observed with any of Q5 - Q7 upstream of FP2. If vertical steering is observed, the automated procedure is repeated using only the vertical ReA3 steerers, and varying the settings of the quadrupoles that steer while keeping the others at their nominal currents. The steerers' domain was constrained further when fine tuning to exploit the region of low steering that was already found, and generally taken as around ± 2 A of the current best tune. Steering in the x-direction at FP2 and beyond is generally dealt with by carefully tuning the dipole and the WF1 magnetic fields.

Results

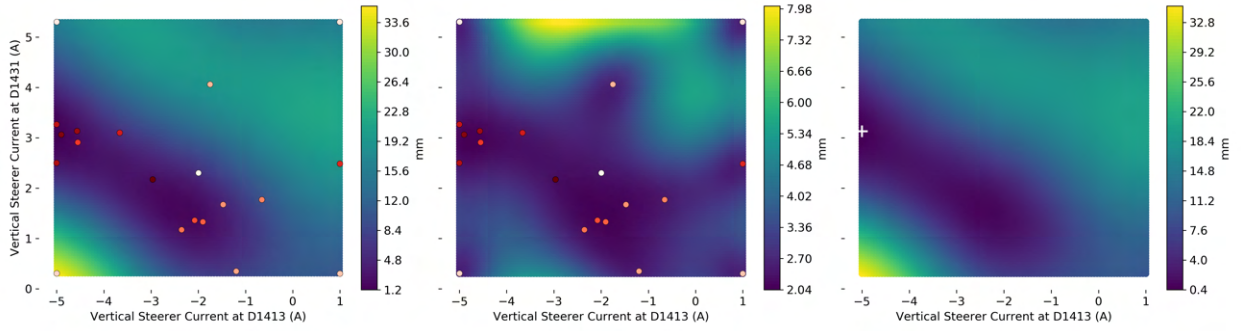
When the code is run, a first observation is made of the tune's initial settings and the first value of the objective function is calculated (total steering distance in 1D or 2D in pixels or mm). This value is then used as the input to the first iteration of Bayesian optimization in which the posterior mean and variance are computed to optimize the acquisition function.

Since computing these quantities is not costly, they are obtained for a large number of points in the phase space of optimization defined for the steerer magnets as shown in Figure 5.8. The left column shows a heatmap the posterior mean $\mu(x)$, the middle shows the posterior standard deviation (SD) $\sigma(x)$, and the right column shows the acquisition function for the most recent observation with a constant exploration weight ξ . In the posterior mean and SD heatmaps, the observations are overlaid as circular data points on the grid. The first observation point is shown in white while the next observations are shown in gradually darker shades of red, up to the most recent observation shown in dark red. The three rows correspond to three different instances where a 2D optimization was performed on either the vertical or horizontal steerers over different phase spaces as indicated by the axes. It can be seen from the posterior mean maps that it is low where the observation mean is low. Whereas for the posterior SD, it is low near the observed parts of the domain (near the sampled points) and high further away from them. On the acquisition function plots, the white cross indicates the next sample point, i.e. the minimum of the acquisition function. A good balance was achieved with exploration weight ξ of at least 0.5. The values adopted allowed for enough exploration to find the region of the global minimum after which exploitation was responsible for the fine tuning of the minimum value.

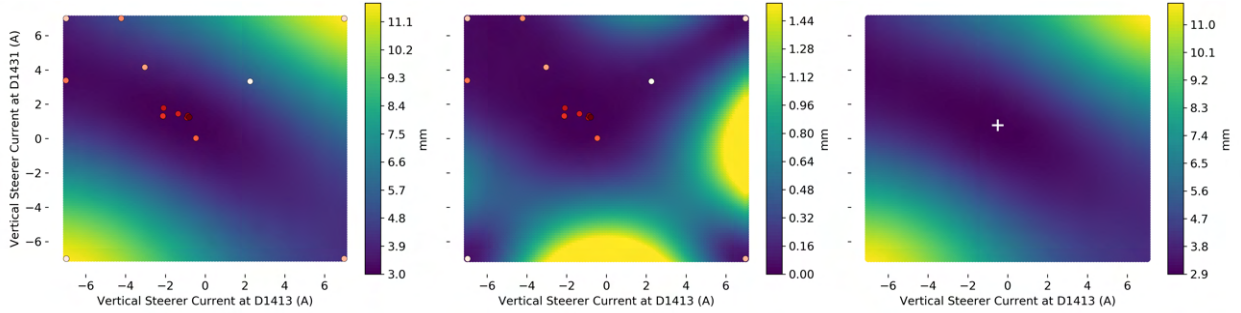
Figure 5.9 shows the speed of convergence of the algorithm for different setups. The domain varied in each case for each steerer magnet. The smallest domain shown in this figure was (-3,3) A for the two vertical steerers corresponding to the 2D with ^{133}Cs line, while the largest domain was (-10,10) A for each of the four steerers, corresponding to the 4D with ^{133}Cs line. In general all 2D optimizations converged within 15 to 20 iterations, while 4D optimizations took about double the number iterations, occasionally needing around 60 when the tune was particularly difficult and the phase space was large. The main criterion for



(a) $\ell = 10.8$ A, $\sigma_n^2 = 1.15$ pixels², $\xi = 3$



(b) $\ell = 1.2$ A, $\sigma_n^2 = 3.5$ pixels², $\xi = 0.5$



(c) $\ell = 5.1$ A, $\sigma_n^2 = 0.07$ pixels², $\xi = 0.3$

Figure 5.8: The posterior mean (left), standard deviation of the mean (middle) and acquisition function (right) for three different 2D steerer optimization runs. The observations are shown in the first left and middle columns by dots shaded by time of observation, with the darkest shade of red being the most recent observation. The next sample point is shown in the right column by the white cross indicating the minimum of the acquisition function. The most recent mean value for for lengthscale and noise variance priors are noted for each, as well as the exploration weight used.

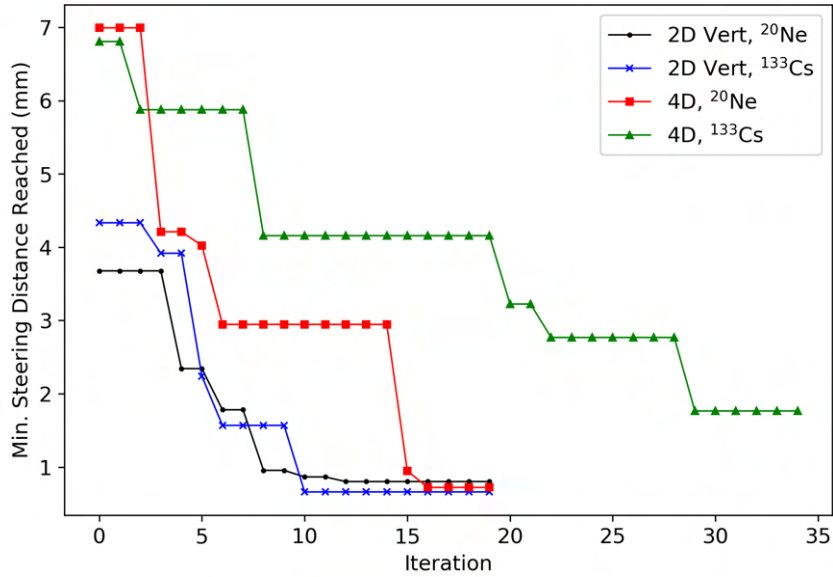


Figure 5.9: Best steering distance reached as a function of number of GP iterations, for 2D (vertical) and 4D optimizations during two different beam commissioning runs.

accepting a tune was reaching a minimum average steering distance from the initial nominal tune of at most 5 mm, typically closer to 2 mm, to avoid having deflection outside of the slit gaps that will be used at the focal planes while maximizing the transmission through the JENSA apertures and to the SECAR focal planes.

Figure 5.10 shows the beam spot steering between four quadrupole tunes at FP1 before (images a - d) and after (images e - h) optimization of the steerers where there was an order of magnitude of improvement on the steering distance. All images were taken at FP1 before the bending magnets were adjusted, so the x-position is not the final beam position. Only the first two quadrupoles upstream of the first two bending magnets, Q1 and Q2, were varied in strength in each image to create a deflection due to the incoming beam angle while Q3 - Q5 were set to zero. These results were obtained in 16 iterations with an exploration weight of 0.5 and initial priors for the lengthscale as $\mathcal{N}(6, 2)$ and for the noise variance as $\mathcal{N}(1, 0.5)$. The currents of the four steerers were free to vary within limits constrained only by the

visibility of the beam on the viewer. It would not have been possible to achieve to this level of precision with this efficiency with manual tuning.

This method was applied at every viewer up to the final focal plane along the SECAR beamline utilizing the quadrupoles upstream of each viewer to fine tune the angular deviation at each location. This was especially helpful to reduce small angular deviations whose effects were negligible at the first viewer location but significant towards the last section of the beamline. Full transmission was obtained after every run when the steerer domains were properly selected, indicating that there is little need for the algorithm to check transmission at every iteration. However such an addition to the objective function would help the algorithm constrain the domain as it explores without much input from the operators.

Final Angular Deviation

While observing steering effects gives some direction as to how the angular deviation of the beam from the optical axis is changing, quantifying these changes is not straightforward. To understand how tuning is impacting the beam angle, ion optical calculations using COSY INFINITY were used to determine the incoming angle that could create the observed level of steering for several runs. Since the x-direction along SECAR is dependent on the dipoles and the Wien filters, only the y-steering is discussed here.

Starting with an initial beam tune prior to optimization of the angular deviation, four images of the beam spot location at FP1, FP2 and D1688 corresponding to four different quadrupole tunes were taken with the viewers at each location. The beam spot location in the x- and y-direction was found for each, and the beam was observed to be steering around 7 mm at all locations. To compare these experimental results with COSY, the transfer matrix was calculated for each quadrupole setting, and the beam spot center in the x- and y-direction was found at FP1, FP2 and D1688 for a large range of initial beam angles covering

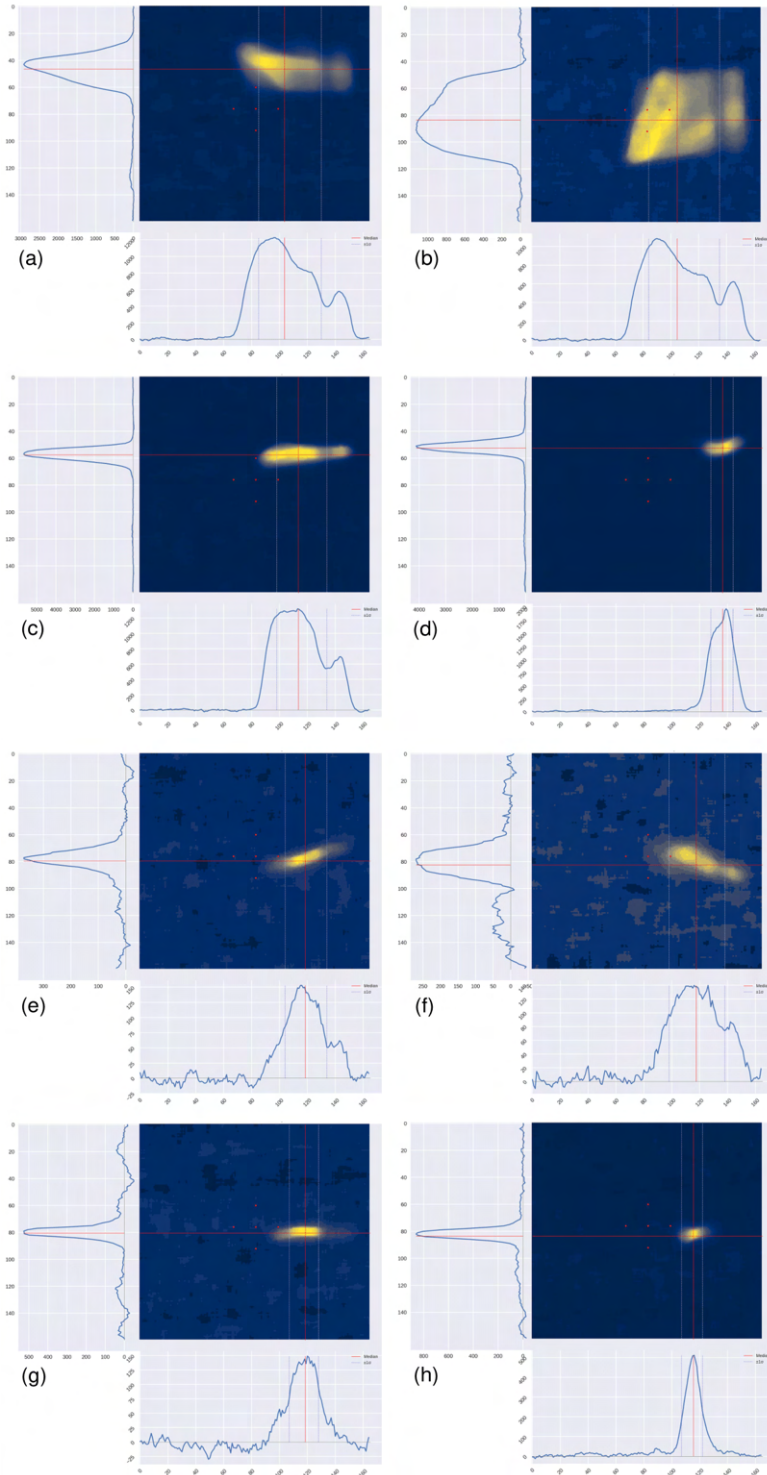


Figure 5.10: Beam spot steering at FP1 before (a - d) and after (e - h) optimization of the beam angle for a 4D run with a ^{20}Ne beam. The steering decreased from an average of 7 mm to an average of 0.2 mm. All axes are in pixels, and 16 pixels correspond to 5 mm.

-3.4 to 3.4 mrad. The initial angular deviation in the y-direction that could lead to a 7 mm steering was found to be 1.6 mrad.

The same comparison was repeated for the beam spot images after the incoming beam angle was adjusted using the Bayesian optimization at each of those locations. The remaining steering seen experimentally in the y-direction after optimization was 0.7, 0.4 and 0.6 mm at FP1, FP2 and D1688 respectively. It was found using COSY that the incoming y-angle explaining these results was 0.8 mrad.

These results highlight the effects of angular deviations as small as 1.6 mrad at the target and the importance of minimizing that deviation at different locations in SECAR. The tuning method presented is sensitive enough to ensure angles of <1 mrad on the target that are needed for full recoil acceptance. The effectiveness of the tuning procedure is highly dependent on the initial conditions of the beam, especially the upstream ReA3 beamline as it affects the beam at the JENSA target location. From multiple beam tests and ion optics comparisons, it was shown that the steering can be minimized to negligible levels, provided that the initial starting tune's angular deviation is not too large.

5.3.7 Ion Optics Optimization

For optimal separator performance, the unreacted beam particle suppression needs to be maximized by minimizing the horizontal beam spot sizes at the mass selection focal planes (FP2 and FP3). As only WF1 was installed at the time of these beam runs, optimization at FP2 is discussed in this work. Having a well focused beam of recoils that is well separated from the equally well focused unreacted beam is crucial for the mass resolution. To optimize the beam rejection, the ratio of the width w of the beam spot to the horizontal distance between the recoil focus and the unreacted beam focus Δx needs to be minimized at FP2 (see

Figure 3.5 for reference, black and blue lines). This allows for the slits to be closed as tightly as possible around the recoils and reduce transmission of any unwanted beam particles. Both the width and the beam separation are characteristic of the specific beam optics for each reaction: Δx is related to the mass difference between the beam and the recoil, while for given beam properties w depends solely on the quadrupoles Q1 - Q7, hexapoles Hex1 - Hex3, and the octupole Oct1 settings upstream of the velocity filter (WF1). While the optimal ion optical tune was determined through COSY INFINITY simulations, the best experimental ion optical setting is likely to be different owing to imperfections in the simulation. Therefore to minimize $w/\Delta x$, all focusing magnets upstream of FP2 need to be adjusted in such a way to minimize the width w at the mass slits while keeping full transmission and the beam position centered between the slits. This multidimensional optimization was tested during SECAR commissioning operations using the Bayesian approach described in Subsection 5.3.1, and is discussed here in detail.

The final ion optical settings need to transmit the beam fully within the angular (± 25 mrad) and energy ($\pm 3.1\%$) acceptance of the device (see Chapter 3 or [6] for more details on the SECAR design parameters). Along with a narrow beam spot width, having an ion optical focus so that the beam spot does not move within the separator's acceptance is crucial to allow slit gaps as narrow as possible. In this work, the limits of the energy acceptance were pushed by optimizing the focused beam spot position within an energy range of $\pm 4\%$ and ensuring the beam spot did not move significantly within that energy range. In the future, a similar measurement needs to be done for the angular acceptance.

Method

Once a well-aligned beam was transmitted to FP2, and after the WF1 settings were optimized, the quadrupoles (and some hexapoles) were optimized at the FP2 viewer. Algorithm

?? was adapted to this optimization goal. The unknown function f to be minimized now represents the beam spot width in the x-direction (projected on the x-axis) as a function of all seven quadrupole tune settings, as well as one or more of the hexapole magnets available upstream of FP2 (Hex3 and Oct1 were not included in these tests). The observations sampled in this case were simply the horizontal beam spot widths directly measured from the viewer images at FP2, defined as $\pm 1\sigma$ from the median peak of the beam spot following the viewer analysis method described in Section 4.3.1. The optimization takes the selected magnet current setting parameters as inputs and iterates over possible combinations to guide the selection of the next observation point.

As the optimization is being done at +4% and -4% dE/E as well as at the nominal energy, some sampled ion optical settings resulted in a very narrow beam, albeit away from the ion optical center of the beamline (effect of quadrupole steering when the beamline is not at the optimized initial energy tune). Additionally, depending on the tune being sampled, the beam occasionally took a shape that is too long in the y-direction - the beam spot edges could not be seen on the top and bottom of the viewers, raising concerns about losses in the beamline. To avoid having to check the transmission at every iteration, the beam spot widths in both x- and y-direction were checked by the optimizer at every iteration, a method that has provided 100% transmission as checked manually at the end of each optimization. To achieve that while keeping the beam centered, the objective function was weighted with the width in the y-direction, keeping it at most the size of a third of the viewer height, and penalized when the center location in the x-direction was far from the starting position by more than the size of the width. The final form of the objective function for this ion optical

optimization took the form

$$f(x_{GP}, w_{init,x}, w_{GP,x}, w_{GP,y}) = \left(\frac{x_{GP} + w_{GP,x} - x_{init,x}}{20} \right)^4 + \left(\frac{w_y}{70} \right)^4, \quad (5.23)$$

where the measurements of the GP sample beam position x_{GP} , initial width in the x-direction $w_{init,x}$, sample GP width in the x-direction $w_{GP,x}$, and sample GP width in the y-direction $w_{GP,y}$ were observed at the viewer installed at FP2. The function form and weights were derived empirically after several tests runs to maximize transmission and minimize beam spot movement from its initial starting point. With the updated objective function, Algorithm ?? was applied with the following details: f was sampled following Equation 5.23, and the inputs were the magnet current settings being optimized.

Once the optimization is run, the magnet setting providing the smallest value of f over the energy acceptance is selected as the final optimal tune. The procedure to optimize the quadrupoles and hexapoles upstream of FP2 is described below.

Step-by-Step Ion Optics Optimization Procedure

1. After achieving a non-steering tune at FP2 and setting B1 - B4 and WF1 correctly, all the quadrupoles and hexapoles are set to the nominal COSY settings scaled to the corresponding $B\rho$ (see COSY map in Table 3.2).
2. The initial position and width of the beam spot at FP2 are recorded at this energy. The former is used in the objective function as shown in Equation 5.23.
3. SECAR is scaled down 4% in energy from the nominal tune. The initial position and width are recorded at this energy as well.

4. The GP code is run to optimize the acquisition function at FP2 using Q1 - Q7 and Hex1 - Hex2. The domain for all magnets is defined as ± 15 A of the initial nominal values.
5. Once the algorithm has found a minimum for f in Equation 5.23 corresponding to a beam spot within about 2 mm of the original beam spot position and with a width smaller than the initial width, this best tune and width are recorded and called c1_1 (c*_ $\$$ convention is followed where c stands for *candidate*, * denotes the iteration of this procedure and $\$$ is the scaling iteration within each procedure).
6. SECAR is scaled up 4% in energy from the nominal tune. The dipoles and WF1 are cycled. The initial nominal width is recorded at this energy as well as the width using the scaled c1_1 tune.
7. The GP code is run to optimize the acquisition function at FP2 using Q1 - Q7 and Hex1 - Hex2. The domain for all magnets is defined as ± 2 A of the scaled c1_1 values.
8. Once a minimum is found again, the best tune and width are recorded and called c1_2
9. SECAR is scaled back to the initial (0%) energy from c1_2 and the width is recorded.
10. SECAR is scaled down 4% in energy again from c1_2 and the width is recorded.
11. The best tune between nominal and c1_2 is selected (or between nominal and all c*_ $\$$ iterations done).
12. A transmission check is done at every Faraday cup after selecting the final tune.

The best tune is defined as the one that minimizes the horizontal width as well as the deviation of the beam spot at FP2 from the initial position among all candidates. To quantify

that further, the slit gap settings to be used with each beam spot width to have $\pm 2\sigma$ of the beam pass through with an energy acceptance of $\pm 4\%$ is calculated, and the tune with the narrowest slit gap is the final optimized tune.

Results

This method was first tested during the June 2020 commissioning run with a $^{133}\text{Cs}^{41+}$ beam at 1 MeV/u. The above procedure was followed to optimize within an energy acceptance of $\pm 4\%$. The best tune achieved was labeled c4_2. In this run, the quadrupoles Q1 to Q7 and the hexapoles Hex1 and Hex2 were optimized. In July 2020, a second optimization was run with a $^{20}\text{Ne}^{8+}$ beam at 1.17 MeV/u where Q1 to Q7 and Q1Hex were optimized, while Q1Dipole, Hex1 and Hex2 were off. The c4_2 settings were compared to the last iteration c5_2 and to the nominal starting values. All these tunes were scaled to the corresponding $B\rho$ of each run. In both the ^{133}Cs and ^{20}Ne case, Hex3 and Oct1 were off.

Figure 5.13 displays the beam spot position (solid red lines) and width (dashed blue lines) at FP2 for c4_2, nominal, c5_1 and c5_2, with the rows corresponding to +4%, 0%, and -4% scaling in energy, respectively, for the case of the $^{20}\text{Ne}^{8+}$ beam. For each tune, the slit gap that has to be set to in order to let through 2σ of the beam distribution from the x-center in both directions within the full energy acceptance was calculated. Table 5.1 summarizes the results for both beam runs. Figure 5.12 shows the speed of convergence for 8D (Q1 - Q7 and Q1Hex) and 9D (Q1 - Q7 and Hex1 - Hex2) optimizations.

It is clear that the method offered an improvement in the width size with the ^{133}Cs beam, while no improvement was achieved on the nominal settings with the ^{20}Ne beam where the nominal tune still provided the best optics. A comparison of the beam spot before and after optimization with the ^{133}Cs beam is given in Figure 5.11. The total shift in x-position between the two images is about 1.3 mm and no significant change in the length in the

	Slits	Nominal	C3_1	C4_1	C4_2
$^{133}\text{Cs}^{41+}$, $B\rho =$ 0.4667 Tm	Left (mm)	59.76	60.08	57.66	60.73
	Right (mm)	65.89	66.53	65.40	64.92
	Gap (mm)	6.13	6.45	7.74	4.19
	Slits	Nominal	C4_2	C5_1	C5_2
$^{20}\text{Ne}^{8+}$, $B\rho =$ 0.3887 Tm	Left (mm)	62.02	63.79	341.5	55.40
	Right (mm)	70.24	72.66	417.5	67.66
	Gap (mm)	8.22	8.87	12.26	12.26

Table 5.1: Slit gaps needed to admit the 2σ beam width within dE/E for each tune.

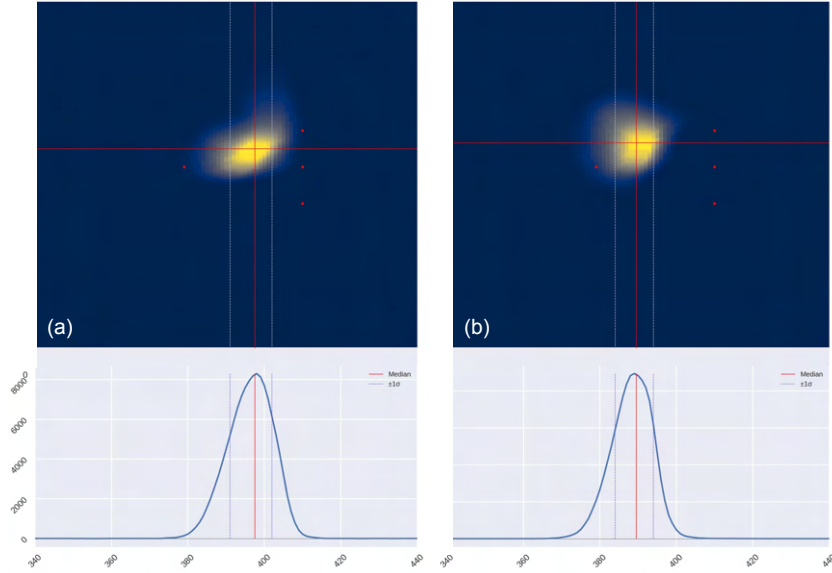


Figure 5.11: (a) Nominal and (b) after the GP optimization at FP2 for the ^{133}Cs commissioning run. Red dots indicate 5 mm. X-axis scale is in pixels, where 31 pixels is 5 mm.

Beam	$B\rho$ (Tm)	COSY (mm)	Nominal (mm)	Best (mm)
^{133}Cs	0.4667	4.08	3.55	3.22
^{20}Ne	0.3887	4.02	4.84	4.84

Table 5.2: Beam spot diameter at FP2 calculated in COSY with a target width of 1.5 mm (2σ), compared to the widths ($\pm 2\sigma$) measured experimentally with the nominal beam settings and with the best settings after optimization.

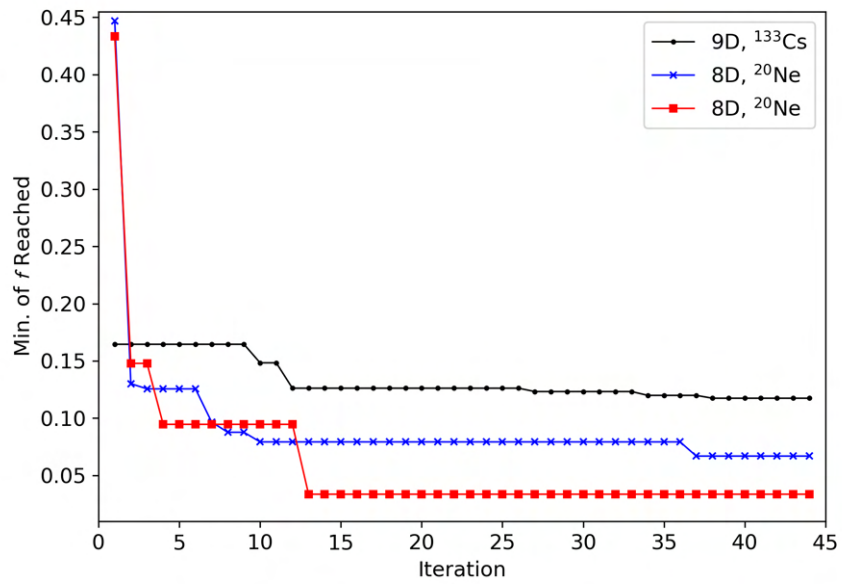


Figure 5.12: Minimum of the objective function defined in Equation 5.23, reached as a function of number of GP iterations, for 8D and 9D optimizations.

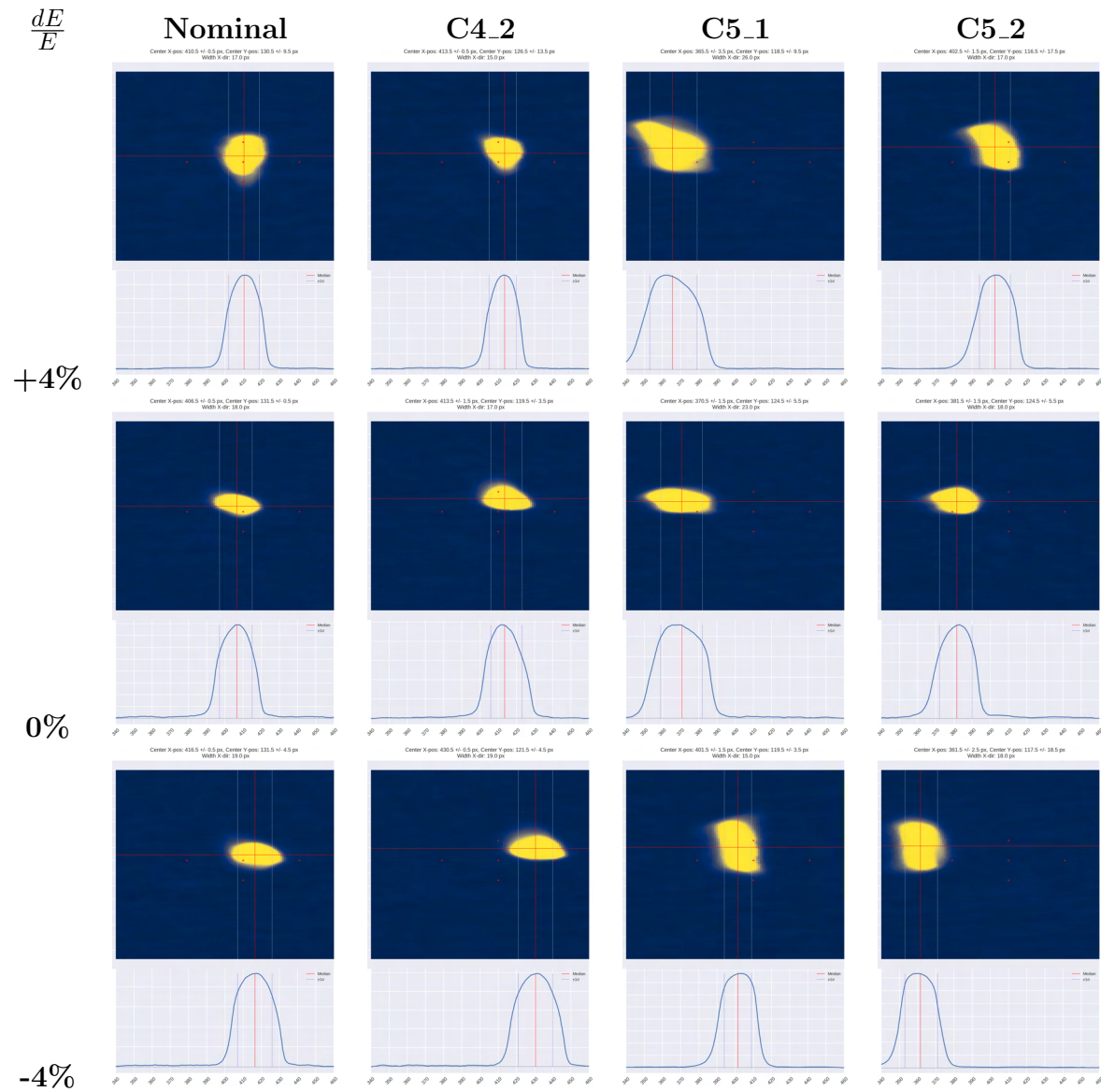


Figure 5.13: The ^{20}Ne beam $\pm 1\sigma$ widths within the energy acceptance. Scale is 31 pixels to 5 mm.

y-direction is seen. The beam spot widths ($\pm 2\sigma$) were compared with COSY calculations assuming a ± 1.5 mm radius in the x-direction at the target (2σ) and a negligible beam angle at the target. The COSY widths were calculated at FP2 and corrected up to fourth order. The results shown in Table 5.2 indicate that the nominal optics were sufficient to achieve the nominal mass resolution in the case of the ^{133}Cs beam. However with the ^{20}Ne beam, a beam size $\sim 20.6\%$ larger than theoretically predicted, and therefore a reduced mass resolution by the same amount, was observed experimentally. This may be due to higher order effects since the hexapoles were not included in the ^{20}Ne optimization.

The Bayesian optimization of the optics decreased the beam size by 9.2% in the case of the ^{133}Cs , but offered no improvement with the ^{20}Ne beam. The latter results may be attributed to the inclusion of Q1Hex in the optimization, which may have steering effects on the beam that were not compensated by the Q1Dipole, possibly driving the optimization away from the best optics.

These results have shown that it is beneficial to experimentally optimize the magnets when there is room for improvement on the nominal settings as seen in the case of the ^{133}Cs beam. The Bayesian approach taken using Gaussian processes was shown in these preliminary tests to be an efficient and precise way to achieve that in order to provide the best beam suppression possible. The ^{133}Cs measurements confirmed the ion optical design. While it is unclear why for the measurements with the ^{20}Ne beam a larger beam spot size than predicted was obtained, it may be owed to higher order contributions that need to be corrected to achieve the mass resolution. In Chapter 7, improvements on the presented tuning methods and Bayesian optimization are suggested to address this issue in the future.

Chapter 6

Dipole Energy Calibration

Astrophysical proton-induced reactions occur in narrow energy bands, and the precise energy of narrow resonances plays a crucial part in the reaction rate formalism discussed in Chapter 2. It is therefore necessary for the energy of the ion beams used in direct experimental measurements of such resonances to be known within a few keV to ensure the energy of the desired resonance is fully covered by the energy loss in the target. To that end, an independent and precise determination of the incoming beam energy is needed for SECAR. This chapter discusses the theory, method and results of the absolute energy calibration of the first magnetic bend in SECAR.

6.1 Theory

The absolute energy of a beam can typically be determined by the calibration of a bending magnet using energies of certain known resonances or thresholds. In the non-relativistic approximation, the magnetic rigidity of an ion with a total energy E is defined as

$$B\rho = \frac{\sqrt{2AE}}{Q}, \quad (6.1)$$

where A is the ion mass and Q is the ion charge. The effective radius ρ of a dipole bending magnet is dependent on the integration of the magnetic field along the reference beam

trajectory through the magnet, including any fringe fields, divided by the central field. The central magnetic field needed to force an ion on the central trajectory can be expressed as

$$B = k \frac{\sqrt{AE}}{Q}, \quad (6.2)$$

where k is a constant calibration factor. This factor is a characteristic of the magnet, but can be dependent on the applied field due to the progressive saturation of the iron poles. Therefore this factor needs to be experimentally determined for each magnet. Once a magnet is calibrated and k is known, the energy of a beam on the central trajectory can be directly related to the magnetic field.

This calibration becomes straightforward when centering on well-known particle energies, a list of which is recommended in [65]. Proton induced reaction measurements can yield high precision energy calibrations in the 0.3 - 3.5 MeV energy range. While the use of (p,n) reaction thresholds is particularly useful for high proton energies ($E_p = 4.2 - 9.5$ MeV) [12,95], a disadvantage arises from the lesser-known threshold energies and from high neutron background at that energy range [94]. Therefore low-energy proton induced reactions such as (p, γ) are generally employed to calibrate bending magnets. Several calibration measurements are typically needed to cover different regions of the magnetic rigidity domain of an instrument, however in most cases the absolute energy determination at higher energies will still depend on extrapolations towards higher magnetic rigidities. In this work, two well-known $^{27}\text{Al}(p,\gamma)^{28}\text{Si}$ resonances were used to directly measure the calibration factor at four different magnetic rigidities covering a significant fraction of the lower half of SECAR's rigidity acceptance, from 0.14 to 0.4 Tm. The chosen resonances had narrow widths and large resonances strengths, ideal for this application, and were suitable for ReA3's energy

E_R (keV/u)	E_x (MeV)	$\omega\gamma$ (eV)	Γ (keV)	BR	$B\rho$ (Tm)	Beam
1799.75	13.321 (1+)	1.94	0.45	0.94	0.3891, 0.1946	H_2^+ , H^+
991.86	12.542 (3+)	1.15	0.10	0.97	0.2888, 0.1444	H_2^+ , H^+

Table 6.1: Parameters of $^{27}\text{Al}(p,\gamma)^{28}\text{Si}$ resonances scanned for the dipole calibration.

range (0.3 - 3 MeV/u).

6.2 Resonant Reactions and Target Properties

The magnetic calibration factor in Equation 6.2 was measured with two well-known $^{27}\text{Al}(p,\gamma)$ resonances using two different beams (H^+ and H_2^+) with different magnetic rigidities for each resonance as listed in Table 6.1. The resonance energies E_R and strengths $\omega\gamma$ were adapted from [18], and the excited states E_x and widths Γ from [33]. An overview of narrow resonance capture reactions and laboratory yield measurements can be found in Chapter 2. The branching ratios BR taken from the decay schemes in [70] were added up from all the contributions to the 1.779 MeV first excited state in each cascade. The magnetic rigidity $B\rho$ with the corresponding projectiles for each resonance scanned is also listed.

In the resonant $^{27}\text{Al}(p,\gamma)$ reaction, a proton beam impinges on a ^{27}Al target with an energy that matches the resonance energy E_R within its width, and is captured by a target nucleus to produce an excited ^{28}Si nucleus at a state E_x . At de-excitation, γ -rays are emitted following the decay cascades described in [70]. The highest branching ratio of the decays in each cascade corresponds to the dominant transition from E_x to the first excited state at 1.779 MeV (2+), then finally to the ground state (0+). The latter transition's yield at each energy was measured by γ -ray detectors installed at the target location. The observed yield curve has an inflection point and a width corresponding to the resonance energy and the beam energy spread, respectively. The energy width of the resonances is negligible in the

cases considered here.

The ^{27}Al target foil used during these calibration measurements was fabricated at the NSCL's detector lab through the process of evaporation. The foil had a thickness 0.11 mg/cm^2 ($\sim 0.45 \text{ }\mu\text{m}$), falling under the category of semi-thick targets for resonance measurements. The energy loss in the target ΔE , corresponding to 21.4 keV and 14.5 keV at 992 and 1800 keV/u , respectively, is large enough to exceed the width of the resonance and to observe a thick-target yield curve while still being smaller than the energy distance to the next lower resonance. At these ratios of $\Delta E/\Gamma$, ~ 32 and 214 at 1800 keV/u and 992 keV/u respectively, this semi-thick target yield is comparable to an infinitely thick target yield. The difference of energies at which the yield is 50% of its maximum and the resonance energy E_R is at most $8 \times 10^{-3} \Gamma$, which is only a 3.6 eV deviation at 1800 keV/u [48]. For these values of $\Delta E/\Gamma$, the width is $\text{FWHM} \approx \Delta E$, and the slope of both the low-energy and high-energy edge of the yield curve is determined by the beam energy spread δ , decreasing with increasing spread. More significantly, for ratios $\delta/\Delta E \sim 0.5$, the maximum yield and the energy at 50% yield will be influenced by the beam energy resolution, decreasing the height of the yield curve and shifting the mid-point energy below the resonance energy. Although the beam energy spread was typically around 0.3% in this experiment, this effect was significant especially with the H^+ beam after going through the degrader described below when the spread was up to 0.5% ($\sim 5 \text{ keV}$ and 9 keV for the 992 and 1800 MeV/u resonances, respectively), resulting in a slight shift of the mid-point energy as shown in Figure 6.1. For this reason, the energy calibration was done by fitting the data with a theoretical yield model based on Equation 2.29 with the calibration factor k and the beam energy spread δ as fit parameters, instead of simply finding the mid-point of the rise of the yield curve.

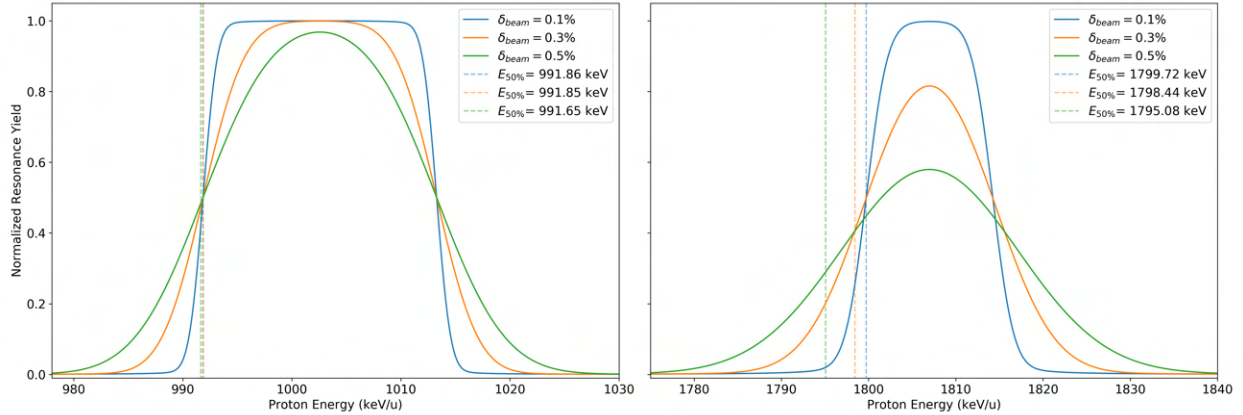


Figure 6.1: Effect of the beam energy spread on the maximum yield and on the mid-point of the rise plotted for a resonance energy of 991.86 keV/u (left) and 1799.75 keV/u (right). The energy at the mid-point is shown in dashed lines at the different energy spreads.

6.3 Experimental Setup

The dipole calibration experiment was performed in two parts at the NSCL’s ReA3 facility, where an off-line stable ion beam injector provided a singly charged proton beam using a small external filament. In September 2019, the first resonance energy scanned was 992 keV/u with an H_2^+ beam. In March 2020, the 1800 keV/u resonance was scanned with a H_2^+ beam, in addition to repeating both the 1800 keV/u and the 992 keV/u resonances with a H^+ beam. A carbon foil of 360 nm was used as a degrader to break the H_2 molecule. It was placed in the object of the horizontal separator (BTS30:D1256), with slits in the object point closed to 1.5 mm in HO and VE. To provide a consistent energy profile, the energy slits of ReA3 (BTS30:D1316) were closed to 7.5 mm in order to provide $\pm 0.5\%$ maximum energy dispersion ($\sim 0.5\%$ FWHM). The setup was identical in both runs except for the target foil that was swapped for a new one before the March 2020 run.

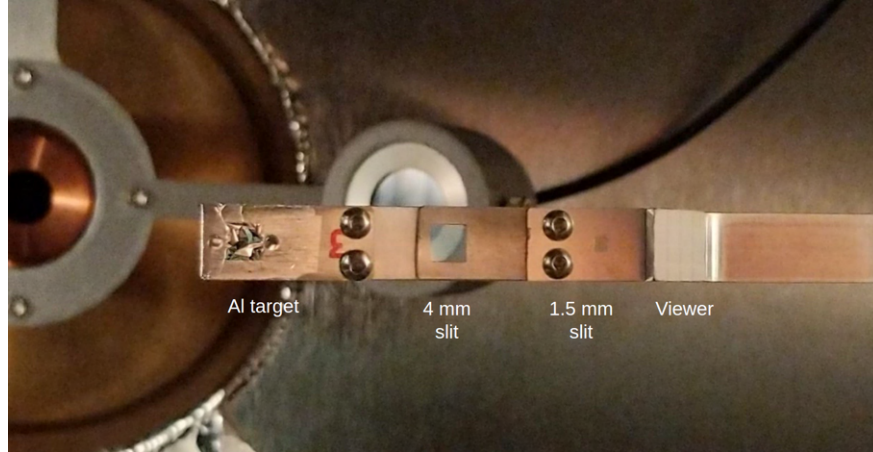


Figure 6.2: JENSA drive setup as used for the dipole calibration runs showing from left to right: Al target foil on 4×4 mm slit, empty 4×4 mm slit, empty 1.5×1.5 mm slit, viewer (slanted at a 45° angle). In this image, the drive is retracted out of the beam's path.

6.3.1 Target Installation

The aluminum foil was self-attached on a 4×4 mm stainless steel slit which was mounted on the JENSA viewer drive along with an identical open 4×4 mm slit for background measurements. Additionally, a 1.5×1.5 mm empty slit was mounted for tuning into SECAR along with the permanent installation of the viewer on that drive. This setup is shown in Figure 6.2. The drive and the drive motor are installed on the right side of the JENSA chamber looking downstream.

6.3.2 Gamma Detection Array

An array of 14 Scionix BGO scintillation detectors was installed on the left side of the JENSA target chamber (downstream direction) in a 7.25 inch diameter circular flange as shown in Figure 6.3. Each detector is comprised of a hexagonal shaped crystal with a length of 75 mm and face to face diameter of 35 mm, encased in a 0.5 mm thick aluminum housing, and read out by a 30 mm Hamamatsu photomultiplier tubes. Since the the right side port of the



Figure 6.3: Setup of the 14 BGO array used for the dipole calibration runs. The flange is mounted on the JENSA chamber.

target chamber was taken up by the JENSA diagnostic drive that includes the target foil, it was not possible to have an array covering both sides of the beamline. For that reason, this flange was manufactured for this experiment at the University of Notre Dame to bring the array as close as possible to the target foil. The depth of the flange was 8.8 inches (accounting for its 0.125 inch thickness), maximizing the efficiency. The center of the flange is approximately 1.9 inches away from the target when the latter is inserted into position along the beam axis. The solid angle coverage of the array around the position of the target foil (in front of the jet) was calculated using a Monte Carlo simulation to be 2.2 sr.

Data Acquisition

The NSCL DDAS system (see Chapter 3) was used to process the BGO array signals in this measurement [77]. A single XIA digital gamma finder (Pixie-16) was used in a XIA crate for the 14 detectors. The Pixie-16 module has 16 channels that take the signal coming from the PMTs and converts them into their digital representation, employing 100 MSPS

ADCs. The DDAS crate was read out by a computer through which the NSCLDAQ handled the data flow produced by the γ -rays in the detector array. The ReadoutGUI was the main interface with the NSCLDAQ where all experiment controls were handled. A SpectTcl implementation for unpacking the event data from the NSCLDAQ was used to export the raw γ -ray spectra for analysis using Python scripts.

BGO Array Calibration and Efficiency

Each of the 14 BGO detectors processes the deposited energy from incoming γ -rays differently which leads to the same γ -ray energy's photopeaks showing up at different ADC channels for each detector. It is thus necessary to individually calibrate each detector in the array. Once that calibration is applied, the spectra from all detectors can be added by energy and the array can be treated as one large detector, making low count peaks in individual spectra more prominent when summed. This energy calibration was done using the well-know γ -ray decays of a ^{137}Cs and a ^{60}Co radioactive sources. The former emits a γ -ray at 661.7 keV and the latter emits two γ -rays at 1173.2 and 1332.5 keV. The sources were placed in the JENSA chamber on the jet receiver, near the location of the target. The recorded net peaks of known energies from the two calibration sources were fitted in each detector spectrum with a Gaussian on top of an exponential function to determine the peak centers. A linear fitting function of the form

$$energy = m \times channel + b \tag{6.3}$$

was applied to the channel numbers corresponding to the center of each energy.

Using the net area under the Gaussian fits of the source photopeaks and the known half-life and current activities of the sources, the array efficiency was determined at those

γ -ray energies. A ^{207}Bi source was used in this test as well to determine the efficiency near the γ -ray energy of interest, however inconsistencies found in the source activity documents rendered these runs unusable. The ^{137}Cs and ^{60}Co source efficiency measurements were 8.8% at 662 keV and 6.8% for 1332 keV. The array's efficiency at 1779 keV was varied when fitting the final yield curve model to the experimental yield as will be described in Section 6.5.4 and resulted in a mean value of 5.7% at 1779 keV.

6.3.3 SECAR Beamline

The first two SECAR dipoles, B1 and B2, were calibrated in this experiment. Four Caylar NMR probes connected to an NMR20 Gaussmeter are permanently installed in those dipoles. One high range and one low range probe are in each of B1 and B2, the former covering 0.16 to 0.8 T and the latter 0.037 to 0.18 T. The absolute precision of the field measurement of the NMR probes is in the order of 10^{-6} . The reader is referred to Chapter 4 for details on the stability of the NMR probes and the reproducibility of the magnetic fields in the dipoles.

The first part of the SECAR beamline up to FP1 was utilized for the purposes of this calibration. Three Faraday cups were used to measure transmission through SECAR: the last ReA3 cup upstream of JENSA (BTS34:D1448), the first cup after Q2 (FC1 at BTS35:D1485) and the cup at FP1 (FC2 at BTS35:D1542). In order to obtain an accurate calibration, one has to ensure the beam is on the ion optical axis. This was done by ensuring quadrupoles do not steer the beam when their strengths are varied. The tuning methods described at length in Chapter 5 for adjusting the incoming beam angle and setting the dipoles were used in this calibration experiment. The viewer at FP1 was the main diagnostic tool used for minimizing steering and tuning the entire setup. The quadrupoles Q1 and Q2, both upstream of B1 and B2, were used to probe the incoming angle of the beam through JENSA along with the

JENSA viewer and the ReA3 steerers upstream (BTS34:D1413 and D1431). The angle of the beam outgoing from B1 and B2, and therefore the dipole NMR field values corresponding to a centered beam, were adjusted by minimizing the steering in Q3, Q4 and Q5, all three located between B2 and FP1.

6.4 Experimental Procedures

A properly aligned beam along the beamline's ion optical axis is critical to achieve accurate calibration of the dipoles. Careful assessment of the delivered beam quality and the transmission at each energy change was necessary before moving on to data collection and eventually the tuning of the two dipoles. Some requirements had to be met to confirm a good starting tune upstream. Those metrics ensured a full beam on the target foil and the ability to successfully achieve a well-tuned beam at FP1. Transmission from the last ReA3 cup at D1448 through the 4×4 slits in the JENSA drive read out on FC1 in SECAR had to be at least 85%, and the FC1 aperture had to read at most 10% of the current read in the collector (beam loss to aperture $\leq 10\%$). Failing to meet these requirements would warrant a re-tune to adjust the incoming angle upstream or the beam size at the target. To help constrain the incoming beam angle and keep the beam close to the dipoles' center axis, the ReA3 collimators at BTS34:D1435 and BTS34:D1448, each having a 5 mm diameter, were inserted every time B1 and B2 were being tuned. However no constraints on the angle were kept downstream of the target as the JENSA apertures (refer to Subsection 3.5.1) at that location were removed for this experiment due to beam losses that could not be accounted for in the beam current integration. Additionally as mentioned earlier, the beam energy spread was fixed by setting the energy slits of ReA3 (BTS30:D1316) at a gap of 7.5 mm in

order to provide $\pm 0.5\%$ maximum energy dispersion ($\sim 0.5\%$ FWHM).

After receiving a new beam energy and checking the quality of the tune, the next step was to collect beam on target data with a subsequent background run through the 4×4 slit at that energy. The current was integrated in FC1 for both those runs. Once the ^{27}Al and the background spectra were collected, the JENSA drive was removed, the ReA3 collimators were inserted, and the beam tuning through JENSA using the ReA3 steerers and guided by the steering in Q1 and Q2 began, until the beam was aligned to the optical axis. Following that centering, the dipoles were ready to be tuned at that energy by adjusting the magnet currents to ensure the beam is exiting the dipoles along the center as determined by the absence of steering in Q3 - Q5.

The method with which the incoming beam angle was adjusted, determining how the beam enters the dipole pair, varied between the run in September 2019 (the first resonance energy scan at 992 keV/u with H_2) and the remainder of the runs in March 2020. In 2019, SECAR was still being tuned manually as described in Subsection 5.1.1. By the next runs in 2020, the automated Bayesian optimization (Section 5.3) was being used to tune the incoming beam angle coming into SECAR from the ReA3 beamline, and an automated scanning script (Subsection 5.2) was used to find the dipole fields that centered the beam along the optical axis of Q3 - Q5. The setup was otherwise identical for all runs.

Once B1 and B2 were set and the beam spot did not steer at FP1, the beam energy was changed by 1 - 3 keV and the process was repeated until a yield curve was seen. Due to time constraints and difficulties in obtaining a good tune at some energies, some resonances could not be sampled sufficiently to observe the full yield curve shape. Additionally, as will be apparent in the next sections, the beam energy spread (up to $\sim 0.5\%$) decreased the maximum yield for some runs, leading to a shift in the energy at which the yield reached

50% of its maximum below the resonance energy E_R by as much as 0.26% as shown in Figure 6.1. However as noted in Section 6.2, this effect did not introduce any issues in the analysis presented.

It is important to note that the readings of the NMR probes in B1 and B2 were matched to within 10^{-5} T during manual and automated tuning, as specified in Chapter 5, to ensure no angle is introduced by the dipoles bending at slightly different strengths. Having both magnets with the same field bending a beam coming in on the optical axis such that it emerges as it entered, with no angle on the optical axis, allows for the calibration of a single field parameter for the pair. The cycling method used at the start of each tune followed the established procedures that were discussed in Chapter 4 to achieve reliable and reproducible readings. The dipoles were always cycled three times at the beginning of each tune, were always set by going down in current, and in the event of an increase, were cycled again. This allowed for reproducible and matched field readings in B1 and B2, and the average of the two measurements was taken as the calibration field at each scanned energy.

6.5 Analysis and Errors

6.5.1 Beam Current Integration and Normalization

FC1 was used for collecting the beam current during all target runs. In order to correctly estimate how much beam was impinging on the foil, a background run with the 4×4 empty slit (identical to the target mount) inserted was taken after each target run. The current readings from each run were extracted from the data archive database for analysis. The charge collected during the target run was scaled (down for H_2 beam and up for H^+) to the background run to correct for losses due to the target widening the beam shape downstream.

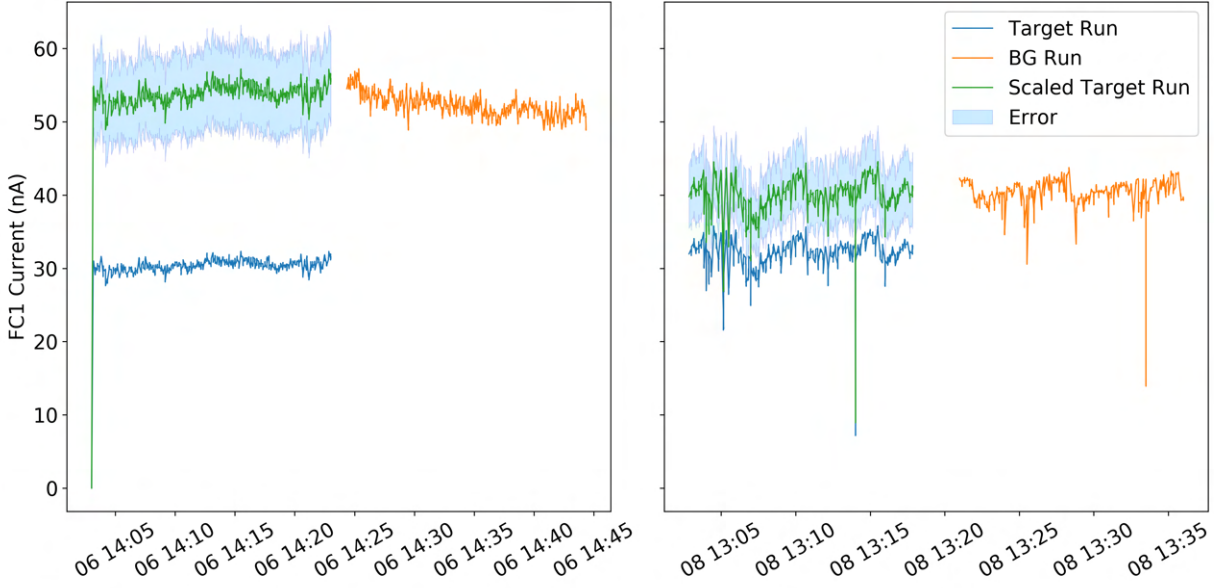


Figure 6.4: Scaling of two different target run beam currents using background current readings, within error bars.

The scale factor was determined by taking the ratio of the averages of the last 20% of the recorded current during the target runs and the first 20% of the background run. The ion source had some instabilities that included sudden drops in intensity on FC1 readings, making it difficult to analyze some runs. To account for most of those variations especially within the time interval between target and background run, a conservative $\pm 12\%$ error on the scale factor was introduced. Figure 6.4 shows two runs' normalization scaling (green line represents the scaled current) with the associated error shown in shaded blue. As absolute currents were not needed for the purposes of this calibration, this was sufficient to obtain relative currents from run to run.

6.5.2 Dipole Field Determination

As mentioned in Section 6.4, the dipole fields at each energy were determined by tuning B1 and B2 through minimizing the steering in Q3, Q4 and Q5. Since tuning was still being done

manually in 2019 during the first resonance scan, the fields values were taken as recorded during each run. By the next runs in March 2020, SECAR tuning had moved to a more efficient and objective automated scan that employs the steering minimization method.

The automated dipole scan recorded the beam spot center position and the steering distance due to Q3 - Q5 at FP1 as a function of the average NMR field in B1 and B2. Refer to Section 5.2 for more details on the scanning method. A parabola was fitted to the scanned curve and the minimum of the parabola was taken as the calibration field. The error on the field at the minimum was $\sim 0.05 - 0.07\%$, and was obtained from the error on the calculated steering distance in the y-axis that is propagated from the ± 1.5 pixel uncertainty on each of the four beam spot locations that quantified the steering. Figure 6.5 shows the results of an automated scan for one of the runs. The steering distance of the beam spot with its associated error as a function of the average of the NMR readings is shown in blue. The orange line is a parabolic fit to the data and the dashed line indicates the region where the best field value lies.

Although the manual and automated methods followed the same criteria for finding the best tune (least steering region), it is likely some error was introduced in the former as operators had to select the best tune visually without any objectively quantitative aid. The subtle differences in steering along the minimum of the curve delineated by the dashed line in Figure 6.5 are hardly noticeable to the human eye, making the error on the determined field at least as large as those derived in the parabolic scans. To quantify the error on the manually derived fields, the mean error and its standard deviation on the field values from the automated scans (the areas delineated by the dashed line for all March 2020 runs) was determined, and a σ_B of 0.05% was adapted for the 992 keV/u with H_2^+ resonance scan measurements.

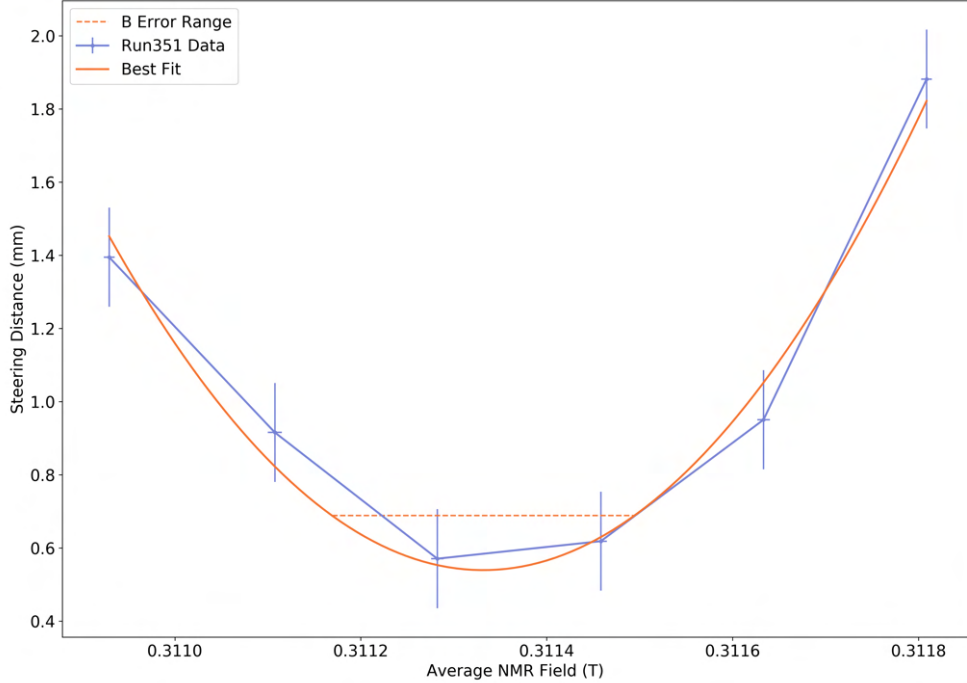


Figure 6.5: B1 - B2 dipole scan on FP1 to minimize steering in Q3 - Q5. The error on the steering distance is calculated from a 1.5 pixel error on each beam spot location measurement. The dashed line indicates the region where the best field value lies.

6.5.3 Gamma-ray Spectra

The raw γ -ray data extracted for each individual detector from the NSCLDAQ were energy calibrated using the calibration curves described in Subsection 6.3.2 then histogrammed and binned in 5 keV bins. The spectra of all 14 detectors were summed for each run, after which the $E_\gamma = 1779$ keV peak was prominent and easy to identify for all runs. The resonance yields were obtained from the γ -ray yield of the 1779 keV peak. To do that, each run was background subtracted after adjusting for the run time using the empty 4×4 slit runs, followed by a Gaussian peak fitting with a χ^2 -minimization method around the 1.8 MeV region in the spectrum. For the $E_p = 992$ keV/u resonance, the peak of interest was isolated in that region. At $E_p = 1800$ keV/u, lower energy γ -rays were detected from $^{27}\text{Al}(p,\alpha)^{24}\text{Mg}$ at 1369 keV and from a resonant contribution of $^{27}\text{Al}(p,p')^{27}\text{Al}$ at 844 and 1015 keV [52],

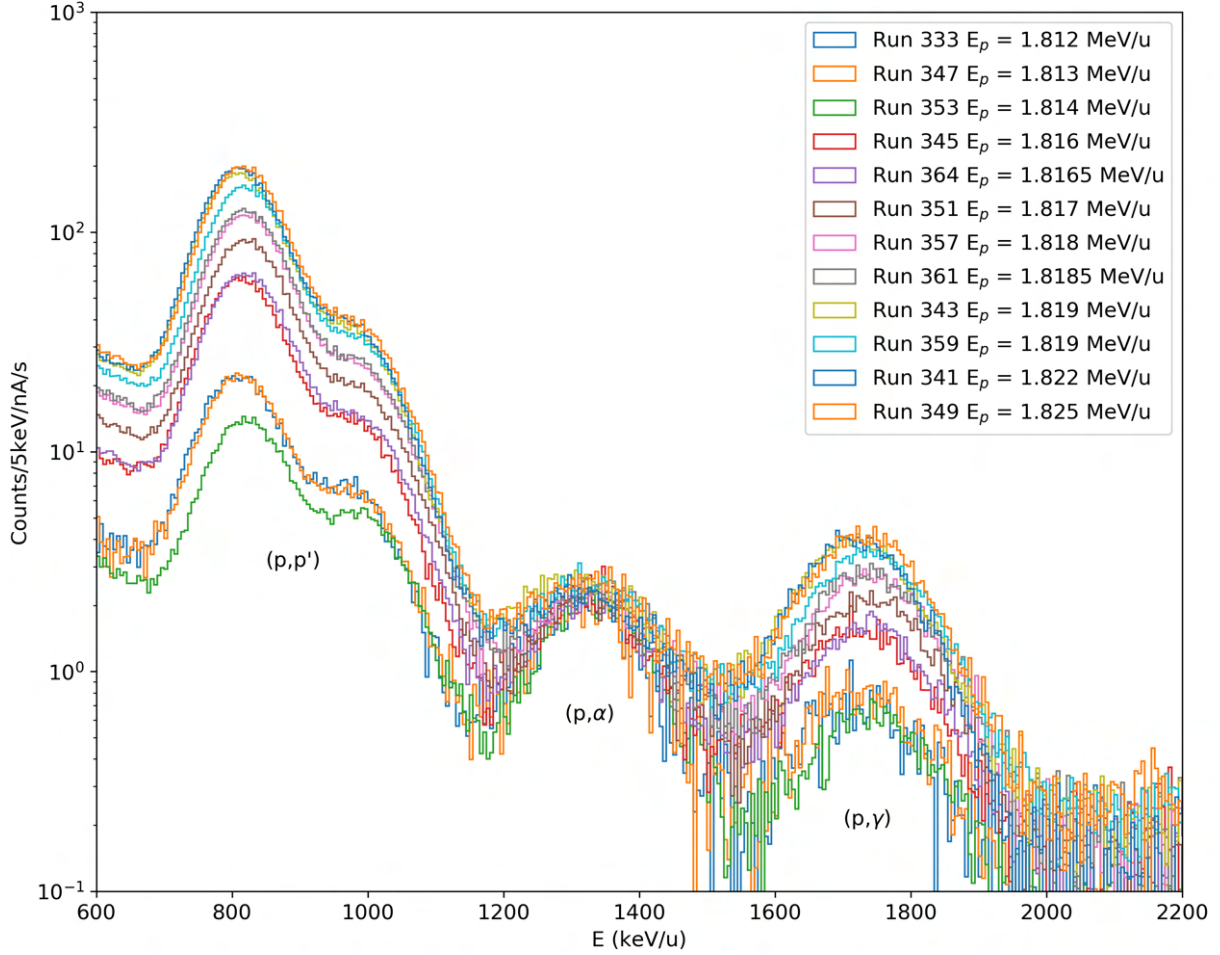


Figure 6.6: BGO array spectra of all runs scanning the 1800 keV/u resonance with H_2 beam. The incoming beam energy E_p corresponds to the ReA3 energies reported. From left to right, the resonant contribution of $^{27}\text{Al}(p,p')^{27}\text{Al}$ at 844 and 1015 keV, the $^{27}\text{Al}(p,\alpha)^{24}\text{Mg}$ peak at 1369 keV, and the $^{27}\text{Al}(p,\gamma)^{28}\text{Si}$ peak at 1779 keV are seen.

as shown in Figure 6.6.

Since this measurement does not aim at deriving absolute resonance strengths but rather focuses on the relative change in yield between runs, consistency in fitting the data between runs was emphasized. For all the runs during the 1800 keV/u scans, a Gaussian curve was fitted to each of the four prominent peaks with an exponential and constant background. The width was a free fitting parameter for the first peak at 844 keV only, and the other three widths were each scaled from that width parameter σ_{844} according to their energy following

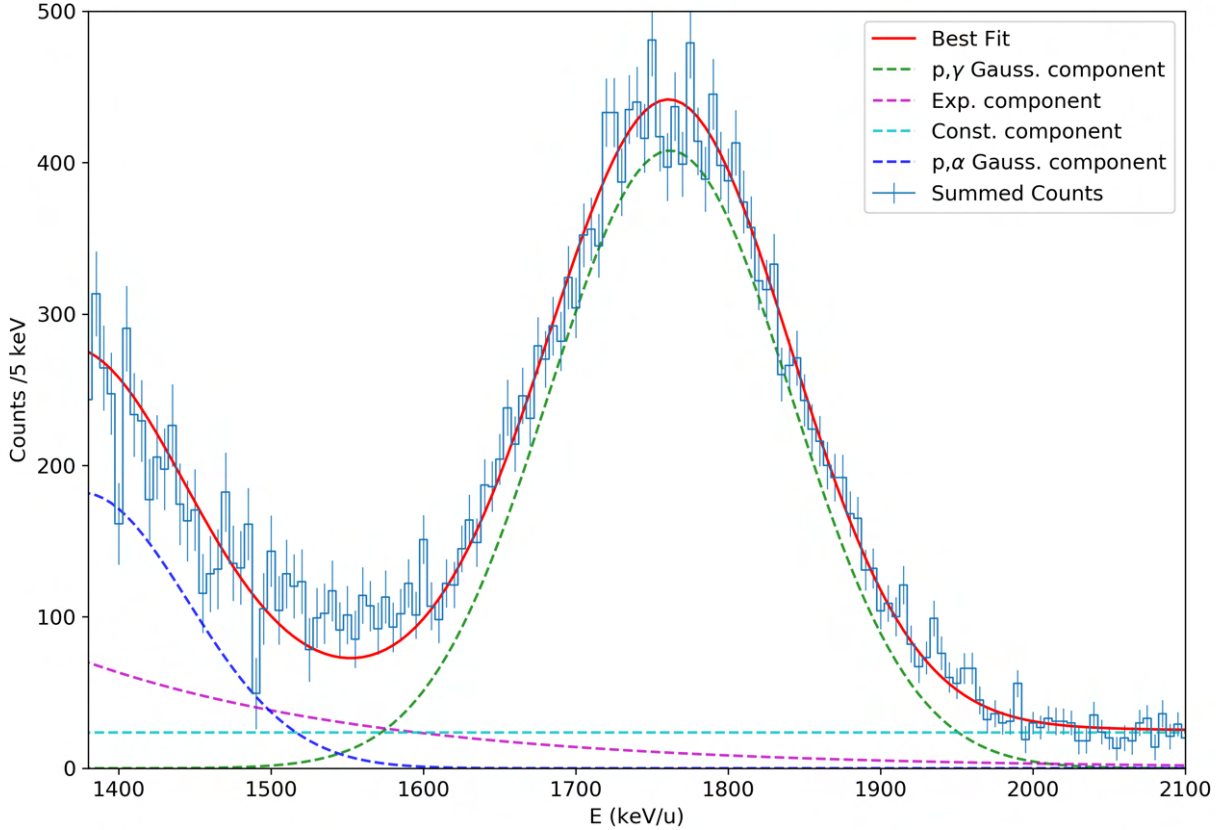


Figure 6.7: The 1779 keV peak at the $E_p = 1800$ keV/u resonance with a Gaussian (green) and a exponential (magenta) plus constant (cyan) background fits. On the left is the (p,α) peak with a Gaussian fit (blue).

the relation $\sigma = \sigma_{844} \sqrt{E/844}$. An example of the resulting fit around the 1779 keV area of interest is shown in Figure 6.7. Since the peak was isolated in the 992 keV/u scan spectra, a single Gaussian with a width scaled from the average width of the 844 keV peak from the 1800 keV/u scans with a constant background was fitted to the data. Summing corrections were determined to be negligible.

The total number of detected photons from the (p,γ) reaction, \mathcal{N} , was extracted by integrating the area under the Gaussian peak fitted at 1779 keV. The resonance yield at

each scanned energy was defined as

$$Y_{exp} = \frac{\mathcal{N}}{e} \quad (6.4)$$

where \mathcal{N}_p is the number of incident protons calculated from the total accumulated charge and the elementary charge e , given the runtime Δt and the normalization current I

$$\mathcal{N}_p = \frac{I\Delta t}{e}. \quad (6.5)$$

6.5.4 Yield Curve Fitting and Uncertainties

A thick target yield model was used to derive the magnetic field at the resonance energy, and therefore the energy calibration factor at that energy. In this calibration, the fitting parameters for the model were the calibration factor k and the beam energy spread δ . The upper limit on the energy spread was set to 0.5% as the ReA3 beamline dispersion slits upstream were adjusted to maintain that constraint at all energies. The theoretical yield model used to fit the experimental data was adapted from Equation 2.29 and was defined as

$$Y_{th,lab} = \frac{\lambda^2}{2\pi} \frac{\omega\gamma}{\epsilon} \eta BR \frac{1}{\sqrt{2\pi}\delta} \int_{E_i-3\delta}^{E_i+3\delta} \left[\text{atan}\left(\frac{E - E_R}{\Gamma/2}\right) - \text{atan}\left(\frac{E - E_R - \Delta E}{\Gamma/2}\right) \right] e^{-\frac{(E-E_i)^2}{2\delta^2}} dE \quad (6.6)$$

where λ is the de Broglie wavelength at the resonance energy, $\omega\gamma$ is the resonance strength, ϵ is the stopping power at the resonance energy, BR is the branching ratio of the 1.779 MeV γ -ray, E_R is the resonance energy, η is the detection efficiency, δ is the energy spread, Γ

is the total resonance width, and ΔE is the total energy loss in the target. The resonance parameters are given in Table 6.1. The stopping power ϵ and the energy loss ΔE were obtained from the SRIM code [101]. E_i , the total energy of the incoming beam, was defined as $\frac{B^2}{k^2 A^2}$, where B is the average NMR value of the tune at that energy, A is the total mass of the incoming beam particle, and k is the dipole calibration factor. Since the BGO array efficiency η in Equation 6.6 was not known at the γ -ray energies measured (see Section 6.3.2), it was treated a free parameter in the fitting as well.

The fitting parameters k , δ and η were varied simultaneously within a defined grid space in a χ^2 -minimization algorithm to fit the experimental data Y_{exp} to the theoretical yield Y_{th} given by Equation 6.6. At each point in the three-dimensional space defined by the values of k , δ , and η , the χ^2 statistic was calculated for N data samples following

$$\chi^2 = \sum_i^N \frac{(Y_{th,i} - Y_{exp,i})^2}{\sigma_{T,i}^2}, \quad (6.7)$$

where the total two-dimensional variance is

$$\sigma_T^2 = \sigma_Y^2 + \left(\frac{dY_{th}}{dB} \sigma_B \right)^2, \quad (6.8)$$

and

$$\left(\frac{\sigma_Y}{Y} \right)^2 = \left(\frac{\sigma_N}{N} \right)^2 + \left(\frac{\sigma_I}{I} \right)^2. \quad (6.9)$$

For the choice of a 1σ (68%) confidence interval, the value of the critical χ^2 statistic was derived from the integration of the χ^2 probability distribution at 68% or higher

$$\int_{\chi_{v,68\%}^2}^{\infty} f(\chi^2) d\chi^2 = 0.32 \quad (6.10)$$

where v is the number of degrees of freedom, and the probability distribution is defined as

$$f(\chi^2) = \frac{1}{2^{v/2}\Gamma(v/2)} e^{-\chi^2/2} (\chi^2)^{(v/2)-1}. \quad (6.11)$$

All k , δ and η parameters in the search grid that resulted in a χ^2 that was less than or equal than $\chi_{v,68\%}^2$ were included in the final result. The mean of the values fallen within the $\chi_{v,68\%}^2$ contour region defined the best fit value for each parameter, and the statistical error on that mean was the distance to the contour limit values.

A source of systematic uncertainty on this measurement was the SRIM derived stopping power ϵ for H in Al which has an associated $\sim 5\%$ error [51], affecting the height and the width of the curve. The stopping power was varied within its error to estimate the subsequent effect on the fitting parameters and it was shown that its contribution to the error on the calibration factor was at most 0.02%.

A larger source of systematic uncertainty was introduced by the tuning method itself, and more specifically, how well the beam trajectory through the magnets is known. It was observed over the tuning runs, including the commissioning runs to FP4 in June and July of 2020 (see Chapter 5) when small residual angular deviations of the incoming beam angle were corrected downstream, that the resulting beam spot positions after centering in B1 and B2 have a spread of ± 1.25 mm at FP1. This measure represents the uncertainty on the tuning method and the precision to which the ion optical axis is known after centering the beam and tuning the SECAR beamline. Using the dipole magnets' measured dispersion of $1363 \text{ mm}/\frac{dB}{B}$, the effect on the magnetic field is $\pm 0.09\%$. This systematic error contribution to σ_B was added to the final field values in this calibration, the results of which are presented below.

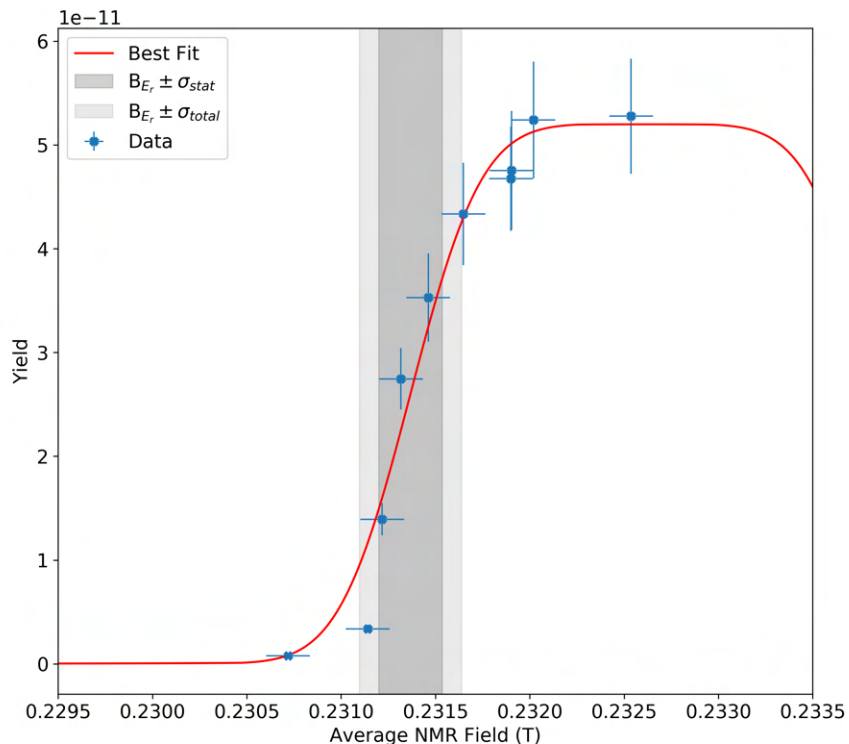


Figure 6.8: The $^{27}\text{Al}(p,\gamma)^{28}\text{Si}$ resonance at 992 keV/u with an H_2^+ beam. The solid curve is the theoretical yield fit to the data. The dark gray shaded area indicates the region of the magnetic field at E_R within the statistical error of the fit. The light gray shaded area is the total error.

In the following figures, the results for all of the yield curve fits are presented. The resonance scans at 992 keV/u are shown in Figures 6.8 and 6.9, and the 1800 keV/u resonance scans are shown in Figures 6.10 and 6.11. The red curve is the best fit of the theoretical yield model defined in Equation 6.6 to the measured γ -yield data. The dark gray shaded areas indicate the region of the magnetic field at E_R within the statistical error of the fit, and the light gray shaded areas are the total error after including the systematic sources of uncertainty.

Since the yield curve shape is known and is dictated by the physics represented in Equation 6.6, it was clear that the additional scatter observed in the case of the 1800 keV/u resonances was introduced by an unknown error in the horizontal direction, and that the

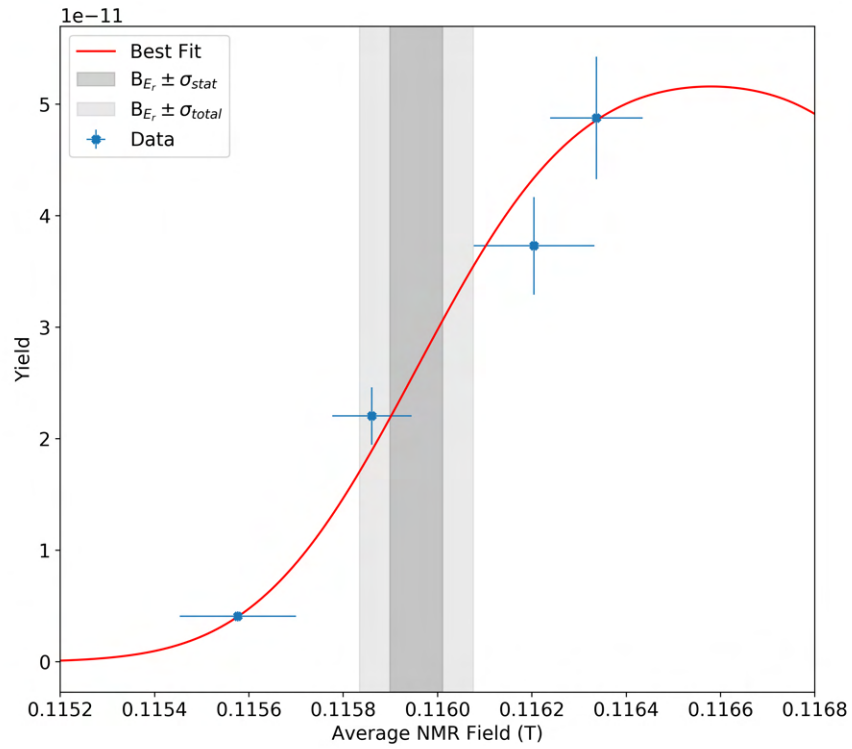


Figure 6.9: The $^{27}\text{Al}(p,\gamma)^{28}\text{Si}$ resonance at 992 keV/u with an H^+ beam.

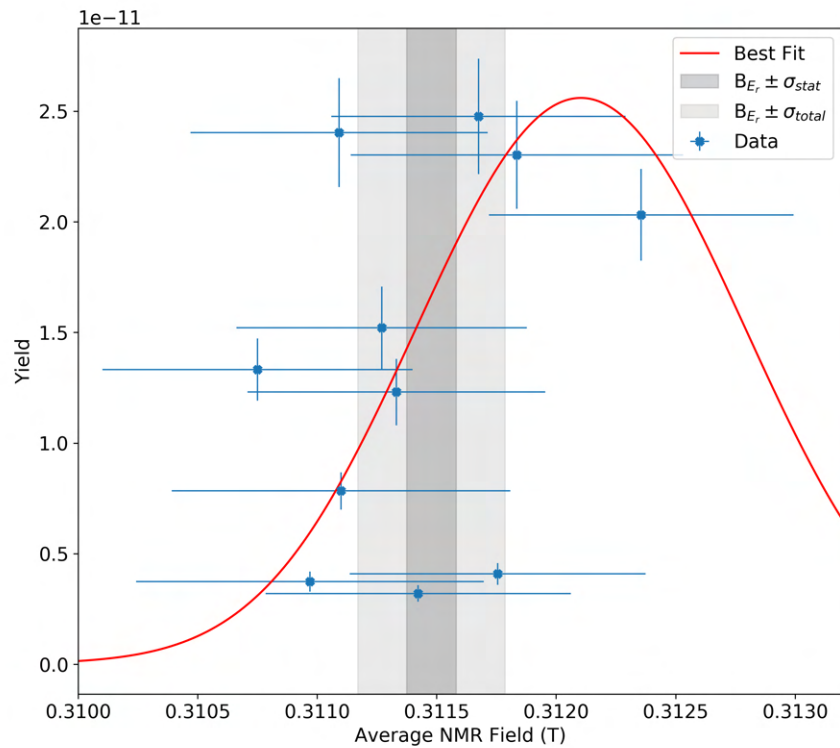


Figure 6.10: The $^{27}\text{Al}(p,\gamma)^{28}\text{Si}$ resonance at 1800 keV/u with an H_2^+ beam.

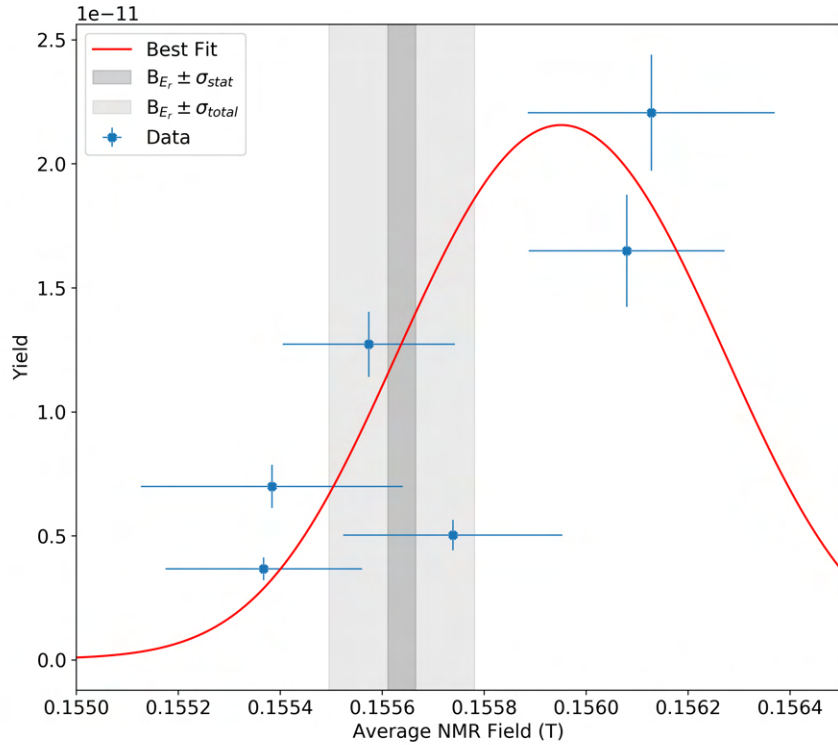


Figure 6.11: The $^{27}\text{Al}(p,\gamma)^{28}\text{Si}$ resonance at 1800 keV/u with an H^+ beam.

error on the NMR field was underestimated. This was likely due to the beam entering the dipoles at different angles for this particular energy tune. The measured NMR fields correspond to the beam exiting the dipoles at the center (least steering path through Q3 - Q7) regardless of the point of entrance of the beam into the dipoles. Therefore with an improperly tuned beam upstream of B1 and B2, the NMR readings may not be providing an accurate value of what the true field should be when the beam is properly centered. To quantify the missing uncertainty, the error in the x-axis was increased for this scan to get a reasonable χ^2 value.

E_R (keV/u)	k ($T\sqrt{keVamu}$)	dk/k (%)	δ (keV)	$d\delta/\delta$ (%)	B_R (T)	dB_R/B_R (%)
991.86	3.64357×10^{-3}	0.07	2.53	35.97	0.231368	0.07
991.86	3.65263×10^{-3}	0.05	4.51	9.98	0.115955	0.05
1799.75	3.64193×10^{-3}	0.03	6.15	28.29	0.311478	0.03
1799.75	3.63958×10^{-3}	0.02	5.00	18.20	0.155639	0.02

Table 6.2: Calibration factors, beam energy spreads and calibration dipole fields obtained for the $^{27}\text{Al}(p,\gamma)^{28}\text{Si}$ resonance energies with their statistical uncertainties.

6.5.5 Energy Calibration Results

The final fitting parameters for each resonance and their corresponding statistical errors are summarized in Table 6.2. The final uncertainty on the calibration field B_R after adding the systematic and statistical errors in quadrature was up to 0.12% for the $E_p = 992$ keV/u scan and 0.09% for the 1800 keV/u scans. The final mean value for the BGO array efficiency was $5.7\% \pm 0.5\%$ at 1779 keV.

Since the magnet may exhibit some residual field at zero excitation, a linear regression with a non-zero intercept was applied to the data. From Equation 6.2, it is clear that the calibration factor is the slope when looking at the magnetic fields at E_R as a function of the resonance energies. Figure 6.12 displays the resulting linear fit and its residuals from the resonances measured. The uncertainties on the calibration factor k were derived by bootstrapping the data: a sub-sample was randomly generated 10000 times with replacement to compute the error contributions from the fitting and from the input calibration fields. The resulting calibration factor was $k = 3.6501\times 10^{-3} \pm 6.2\times 10^{-6}$ (0.17%) T/\sqrt{keVamu} .

This energy calibration enables the determination of the energy of an incoming beam from the NMR fields of B1 and B2 once the beam has been properly tuned following the procedures outlined in Chapter 5. For instance, taking a $^{20}\text{Ne}^{8+}$ beam (to be used in the final commissioning experiment planned for SECAR), the projected energies within the magnetic

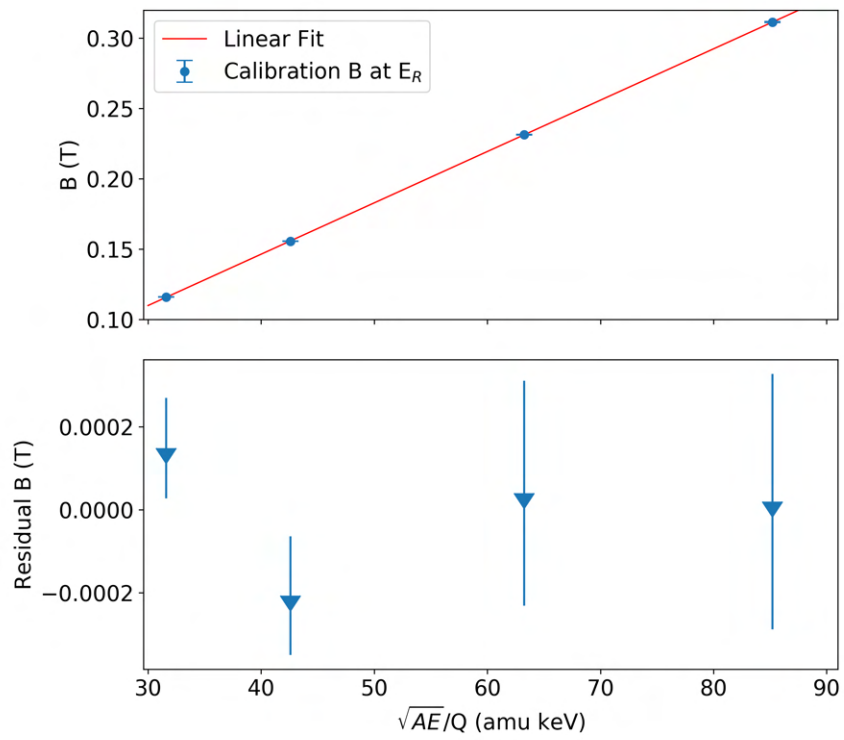


Figure 6.12: Calibration fit to the fields at the resonance energies and their corresponding errors and residuals. The slope is the dipole calibration factor k .

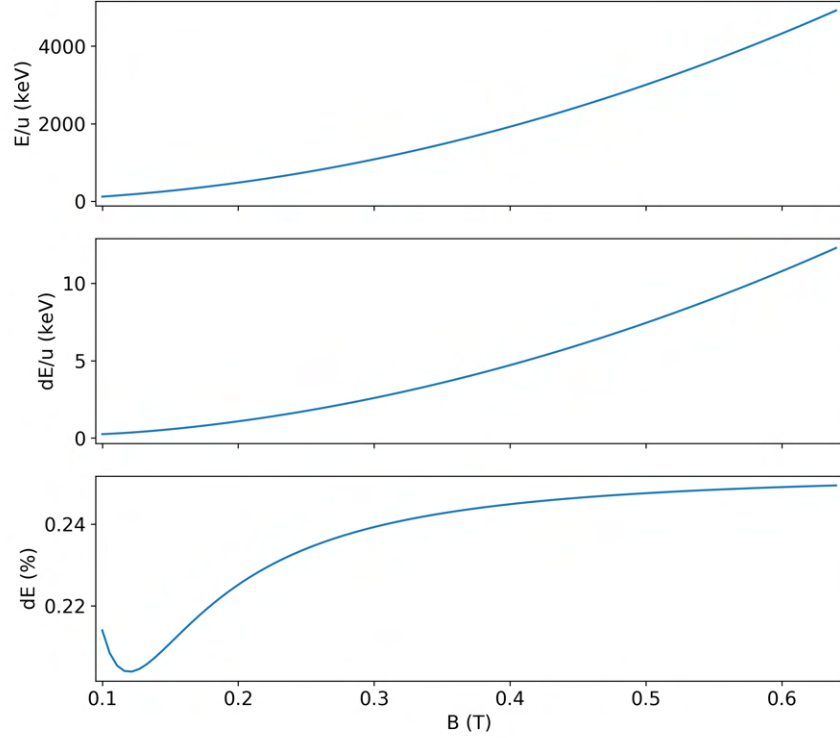


Figure 6.13: Projected energy of a $^{20}\text{Ne}^{8+}$ beam over the B range in keV (top) and its projected error in keV (middle) and percent (bottom).

rigidity acceptance of SECAR that can be measured are shown in the top plot of Figure 6.13. The error on that energy estimate is shown in the middle plot, with the value as a percentage of the beam energy in the bottom plot. For a $^{20}\text{Ne}^{8+}$ beam with an estimated energy around 1.18 MeV/u, the uncertainty on an energy measurement using the calibrated magnets B1 and B2 is $\sim 0.24\%$.

Comparison to ReA3 Beam Energy Measurements

The beam energy delivered to SECAR is also reported by the ReA3 operations team based on measurements using a calibrated magnetic beam analyzer with a beam energy determination uncertainty of $\Delta E/E \sim 0.25\%$ [62]. The beam energies determined from the best fit resonance yield curves in this experiment can be directly compared to these reported energies. The most straightforward comparison is at the point corresponding to

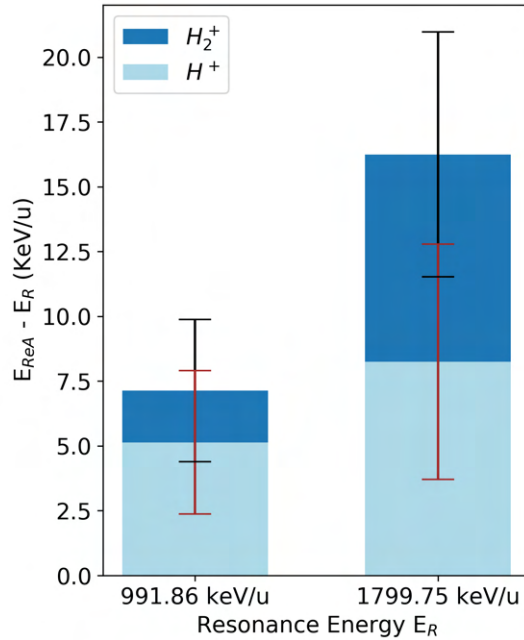


Figure 6.14: The difference between the reported energy ($\Delta E/E \sim 0.25\%$) at the mid-point of each scanned curve and the known resonance energy.

the well-known resonance energy E_R . By interpolating the two closest reported energies to that mid-point, the ReA3 energy at that point, labeled E_{ReA} , was determined. Taking the difference between the resonance energies E_R and E_{ReA} , it was found that the reported energies were consistently overestimated.¹ The results are visualized in Figure 6.14. This solidifies the importance of the energy calibration described in this work as an independent way of measuring the incoming beam energy during SECAR experiments.

Relativistic Calibration

For higher accuracy at higher energies, the energy calibration was also done relativistically. In this case, the location of the resonance energy E_R on the yield curve at the inflection point is assumed to be the same as the non-relativistic case. A relativistic relationship between B and E was derived, using the total energy E_T and kinetic energy KE definitions:

¹It was later found that the time-of-flight calibration of the ReA3 accelerator [96] provides a beam energy ($\Delta E/E = 0.24\%$) with deviations from the measured resonance energies of around 1 - 6 keV [43].

$$E_T = \gamma mc^2 = \sqrt{(pc)^2 + (E_0)^2} \quad (6.12)$$

and

$$KE = (\gamma - 1)mc^2, \quad (6.13)$$

where m is the rest mass, E_0 is the rest energy, and γ is the Lorentz factor. Defining E^* as $(pc)^2$ and using Equation 6.13, one can write

$$E^* = (KE + E_0)^2 - E_0^2. \quad (6.14)$$

Using the results from Table 6.2 and the calculated E^* at each resonance measurement, a linear regression of the form

$$B = k_{rel} \frac{\sqrt{E^*}}{Q} + \text{intercept} \quad (6.15)$$

was fitted to the data to derive the relativistic calibration factor k_{rel} . Figure 6.15 displays the resulting linear fit and its residuals from the measured data. The resulting calibration factor was $k_{rel} = 2.6664 \times 10^{-6} \pm 5.0 \times 10^{-9}$ (0.19%) T/keV.

Taking the example of the $^{20}\text{Ne}^{8+}$ beam again, the projected E^* values within the magnetic rigidity acceptance of SECAR that can be measured are shown in the top plot of Figure 6.16. The error on the prediction is shown in the middle plot, with the value as a percentage of the E^* prediction in the bottom plot. For a $^{20}\text{Ne}^{8+}$ beam with an estimated energy around 1.18 MeV/u, the uncertainty on an energy measurement using this relativistic calibration is $\sim 0.18\%$. The relativistic kinetic energy KE derived from E^* , the corresponding

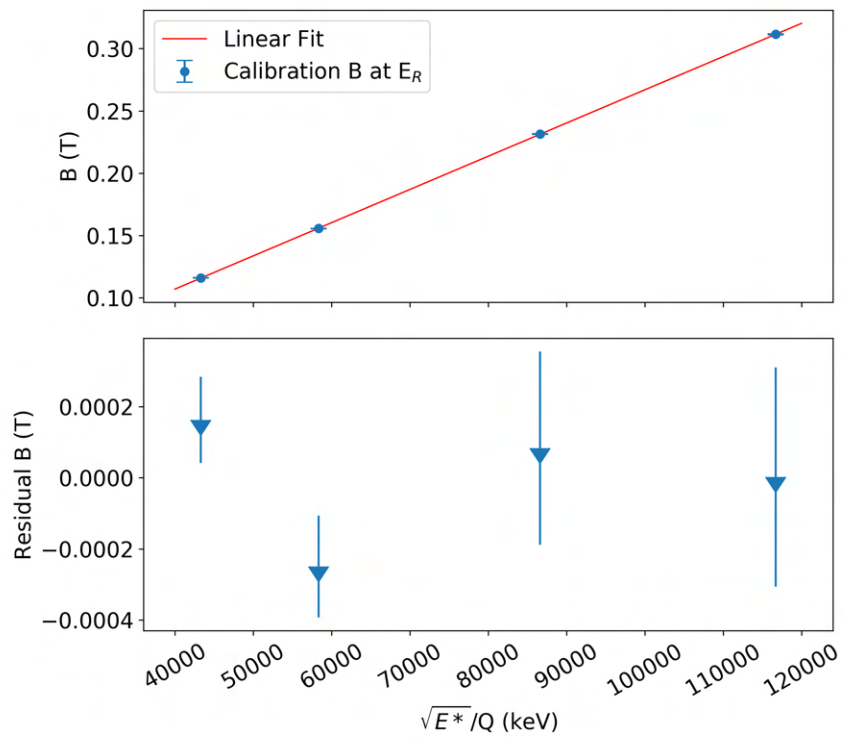


Figure 6.15: Relativistic calibration fit to the fields at the resonance energies and their corresponding errors and residuals.

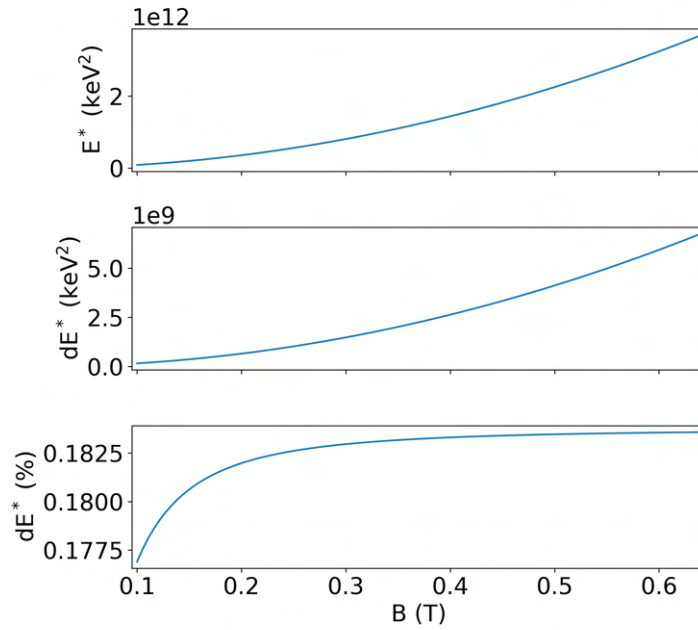


Figure 6.16: Projected E^* of a $^{20}\text{Ne}^{8+}$ beam over the B range (top), its projected error (middle), and percent error (bottom).

non-relativistic energy KE_0 (total energy from the top plot of Figure 6.13), and their ratio are shown in Figure 6.17.

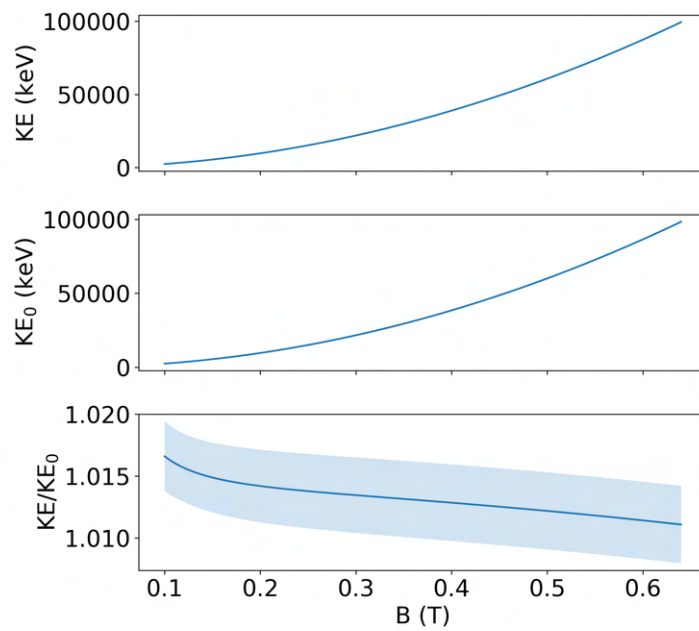


Figure 6.17: The relativistic kinetic energy KE (top), the non-relativistic kinetic energy KE_0 (middle), and their ratio with its error shown with the shaded region (bottom) for a $^{20}\text{Ne}^{8+}$ beam over the B range.

Chapter 7

Conclusions

In this thesis, stable beam commissioning of the new SECAR recoil separator was presented. First, the installation and testing of beamline components including the critical diagnostics was achieved, in addition to establishing operational procedures necessary to attain reproducible and stable machine states that meet the stringent scientific requirements. Subsequently, beam tests allowed for the establishment of a tuning procedure and the implementation of an automated online ML-based approach to optimizing magnet settings, improving the efficiency of the method, the reliability of the results, and the performance of the device. Additionally, the energy calibration of the first bending magnetic dipole pair was achieved via measurements of the γ -ray yields of two $^{27}\text{Al}(p,\gamma)^{28}\text{Si}$ resonances.

Beginning with robust diagnostics and reliable electromagnetic components, tuning procedures were developed to properly transport pilot beams through the beamline. This consisted of adjusting the incoming angle of the beam to center it along SECAR's ion optical axis by tuning the ReA3 steerers installed upstream of the JENSA chamber. After this was achieved, each dipole pair was properly set as the beam was transported through the beamline. In an effort to increase objectivity, efficiency, and reproducibility, a ML-based approach was implemented to optimize the incoming beam's angular deviation. A viewer image analysis software was developed to provide the ML algorithm with precise beam spot locations, facilitating online optimizations. The steering observed on the viewers due to quadrupole magnet strength changes upstream was used to assess the beam's deviation from the ion opti-

cal center as a function of the ReA3 steerer settings. A minimization of this steering ensures the beam is on the ion optical axis. This method, previously used by operators tuning by hand, was successfully implemented into a robust ML algorithm regardless of the beam spot shape changes associated with quadrupole magnet changes. This first implementation of an online Bayesian optimization of a nuclear astrophysics recoil separator was shown to increase the efficiency and precision in achieving the stringent beam parameter requirements needed for optimal separator performance as compared to manual tuning methods. The beam size at the target is still manually checked and provided by the ReA3 operations team. While for the SECAR performance it is critical that the incoming beam on the target has a small angle (< 1 mrad), there is no diagnostics to ensure this. The gas target apertures restrict the beam angle only to < 3.4 mrad. In this thesis, it was demonstrated that SECAR diagnostics in connection with the Bayesian approach for tuning ReA3 beamline steerers can be effectively employed to achieve the required small angles. With this method, negligible angular deviation in the y-direction was found. A small remaining deviation in the x-direction can be adjusted with bending optical elements. This method is now used routinely for all separator tuning, and can generally be applied to other separators and accelerator beamlines.

The ion optical settings of the system are critical for the mass resolution. An optimization of the quadrupoles and higher order elements was performed within an upper limit of the energy acceptance of $\pm 4\%$ using a Bayesian approach with Gaussian processes. A weighted function incorporating the beam width and location was modeled as a function of the magnet settings and minimized at FP2. The ^{133}Cs beam measurements confirmed the ion optical design and were improved by over 9% with the presented method. In the case of the ^{20}Ne beam measurements, a lower than predicted ion optical performance was observed with the nominal settings and the approach presented did not succeed in improving it. This

may be attributed to higher order contributions that were not corrected in this run. More measurements are needed to characterize the ion optics of the system.

The energy calibration of the first dipole pair has been completed by measuring $^{27}\text{Al}(p,\gamma)$ resonant reactions at $E_p = 992$ and 1800 keV/u using H^+ and H_2^+ beams. A BGO detector array was utilized to measure the γ -ray thick target yield around the resonance energy and resulted in a calibration factor $k = 3.6501 \times 10^{-3} \pm 6.2 \times 10^{-6}$ (0.17%) T/ $\sqrt{\text{keVamu}}$. The dominant uncertainty in this calibration is attributed to the inconsistent incident beam angle into the dipole pair. This represents the limitation of the tuning method employed to adjust the incoming beam angle using the ReA3 steerers. Additionally, a relativistic energy calibration was done for higher accuracy when extrapolating to higher energies, and the resulting relativistic calibration factor was $k_{rel} = 2.6664 \times 10^{-6} \pm 5.0 \times 10^{-9}$ (0.19%) T/keV.

7.1 Next Steps and Future Developments

This work constituted a significant portion of the SECAR commissioning. Tests with the JENSA gas target, along with a verification of the angular and energy acceptances of the system, remain to be done ahead of the measurement of a $^{20}\text{Ne}(p,\gamma)$ resonance marking the completion of the SECAR commissioning operations. Continued work on beamline tuning procedures and optimizations will build upon the work presented in this thesis. Several pathways for future developments and improvements are discussed below.

The alignment of the beamline elements arose as a critical issue during the commissioning. There are two parts to the alignment. First, the SECAR beamline ion optical center must be aligned to the ReA3 accelerator beamline. Empirical evidence during tuning has indicated that there is a slight misalignment in the y-direction (perpendicular to the beam

axis) between the ReA3 and the SECAR ion optical axis. This has proven to cause delays in obtaining an acceptable starting tune for the optimization. Additionally, the last ReA3 quadrupoles installed downstream of the steerer magnets may cause steering in an otherwise non-steering and centered tune in SECAR, and this makes setting the appropriate focus and beam spot size that are critical for SECAR performance challenging. This issue may be resolved by extending the Bayesian optimization to the beam spot size and transmission through JENSA and the upstream ReA3 quadrupoles. Second, diagnostic elements along SECAR should be aligned to the optical center. Devices such as BCMs need to be aligned well in order to be useful for centering the beam. Other devices such as the viewers need not be perfectly aligned as the methods with which the centering is done do not rely on visual centers, but rather on the behavior of the steering on the viewers. Several of the viewers currently installed have center locations that deviate from the optical center by as much as 7 mm. As more tuning experience will lead to better knowledge of the ion optical centers at all viewer locations, it may be advantageous to align the physical centers of the viewers with the ion optical center to make tuning more straightforward.

There are several paths to improve and build upon the initial implementation of the Bayesian optimization to the tuning of the ReA3 steerers presented in this work to increase the efficiency of the algorithm. Incorporating transmission measurements (at apertures and Faraday cups) as well as beam position information at the target may increase the efficiency with which the incoming angle is tuned by providing additional constraints on the steerer phase space and reducing the number of observations needed. Additionally, expanding the optimization to include more of the upstream ReA3 beamline or utilizing the extensive ReA3 archived data to inform on incoming beam parameters may be helpful in understanding the properties of the beam. As stated earlier, extending the Bayesian optimization to include the

beam spot size and the transmission through JENSA and the upstream ReA3 quadrupoles may reduce the complications introduced by any misalignment that exists between the ReA3 and the SECAR beamlines. As more tests are performed and more data is collected, a relationship between beam species, beam rigidity and the hyperparameters of the Gaussian process covariance function can be derived for each section of the beamline, possibly increasing the efficiency of subsequent runs. Future work can also include thorough ion optical comparisons of the beam angle in SECAR after the beamline is fully tuned and at different stages of the optimization to gain a better understanding of the system.

The optimization of the ion optical settings was shown to be successful in the case of the ^{133}Cs beam. Further measurements are needed to assess both the robustness of the method and the ion optical characteristics of SECAR (i.e. mass resolution) compared to its design, and to investigate why the method was insufficient in the case of the ^{20}Ne . These measurements should include the optimization of all the higher order corrective elements. Additional optimizations are needed to confirm the settings within the angular acceptance, for example by using a foil at the target to create angular straggling and repeating the method presented in this thesis. The Bayesian optimization may be improved in several ways. As quadrupoles are designed to work in pairs or triplets, a physics-informed correlation matrix can be added to the covariance function of the Gaussian process model to arrive at better optics more efficiently (e.g. see [42]). This can be obtained using the currently available COSY INFINITY model of SECAR. Moreover, the algorithm can be expanded into a multi-objective optimization [32] to efficiently improve the COSY model, and ultimately the experimental device, in achieving a high mass resolution for different scientific experiments. By simultaneously optimizing several transfer matrix elements including the distance from the beam center in the x-direction given the initial fractional angle, energy and mass difference of the beam

particles compared to mean value at the mass slits, the full Pareto front of this optimization can be reached with fewer observations. The multi-objective approach can also be useful in online implementations such as the ones presented in this work where multiple optimization goals are often being sought out (e.g. see [82]). Combining such methods will make achieving the design mass resolution possible in an efficient and reproducible way, and may even lead to further improvements.

Lastly, as tuning procedures improve and more data is available on the central ion optical axis, it may be beneficial to perform additional measurements to increase accuracy of the dipole calibration factor obtained in this work. In the future, this calibration should be extended to higher rigidities ($B\rho = 0.4 - 0.8 \text{ Tm}$), for example using time-of-flight measurements of high rigidity beams.

In conclusion, the work presented in this thesis made significant contributions to the commissioning of SECAR. This included initial studies of the properties of the system, a first demonstration of an online ML-based tuning in an astrophysics recoil separator, and the energy calibration of the first bending dipole pair to provide independent measurements of the incoming beam energy in SECAR. This work paves the way for SECAR to achieve its scientific goals by establishing operational approaches that optimize the recoil separator's performance. As FRIB comes online, SECAR will be utilized for measurements to improve our understanding of novae, X-ray bursts, and other explosive astrophysical environments.

REFERENCES

REFERENCES

- [1] C. Angulo, M. Couder, S. Cherubini, W. Galster, J.-S. Graulich, P. Leleux, F. Vanderbist, and A. Shotter. First results with the recoil separator ARES. *Nuclear Physics A*, 688(1-2):462–464, 5 2001.
- [2] D. W. Bardayan. Transfer reactions in nuclear astrophysics. *Journal of Physics G: Nuclear and Particle Physics*, 43(4):043001, 2016.
- [3] D. W. Bardayan, J. C. Blackmon, W. Bradfield-Smith, C. R. Brune, A. E. Champagne, T. Davinson, B. A. Johnson, R. L. Kozub, C. S. Lee, R. Lewis, P. D. Parker, A. C. Shotter, M. S. Smith, D. W. Visser, and P. J. Woods. Destruction of ^{18}F via $^{18}\text{F}(p, \alpha)^{15}\text{O}$ burning through the $E_{\text{c.m.}} = 665$ keV resonance. *Phys. Rev. C*, 63:065802, May 2001.
- [4] D. W. Bardayan, K. A. Chipps, R. P. Fitzgerald, J. C. Blackmon, K. Y. Chae, A. E. Champagne, U. Greife, R. Hatarik, R. L. Kozub, C. Matei, B. H. Moazen, C. D. Nesaraja, S. D. Pain, W. A. Peters, S. T. Pittman, J. F. Shriner, and M. S. Smith. Direct measurements of (p, γ) cross-sections at astrophysical energies using radioactive beams and the Daresbury Recoil Separator. *European Physical Journal A*, 42(3):457–460, 2009.
- [5] R. D. Belian, J. P. Conner, and W. D. Evans. The discovery of x-ray bursts from a region in the constellation Norma. *ApJ*, 206:L135–L138, June 1976.
- [6] G. P. A. Berg, M. Couder, M. T. Moran, K. Smith, M. Wiescher, H. Schatz, U. Hager, C. Wrede, F. Montes, G. Perdikakis, X. Wu, A. Zeller, M. S. Smith, D. W. Bardayan, K. A. Chipps, S. D. Pain, J. Blackmon, U. Greife, K. E. Rehm, and R. V. Janssens. Design of SECAR a recoil mass separator for astrophysical capture reactions with radioactive beams. *Nuclear Instruments and Methods in Physics Research, Section A: Accelerators, Spectrometers, Detectors and Associated Equipment*, 877(March 2017):87–103, 2018.
- [7] C. A. Bertulani and A. Gade. Nuclear astrophysics with radioactive beams. *Physics Reports*, 485(6):195–259, 2010.
- [8] L. Bildsten. Thermonuclear burning on rapidly accreting neutron stars. In *The Many Faces of Neutron Stars*, pages 419–449. 1998.
- [9] S. Bishop, R. E. Azuma, L. Buchmann, A. A. Chen, M. L. Chatterjee, J. M. D’Auria, S. Engel, D. Gigliotti, U. Greife, M. Hernanz, D. Hunter, A. Hussein,

- D. Hutcheon, C. Jewett, J. José, J. King, S. Kubono, A. M. Laird, M. Lamey, R. Lewis, W. Liu, S. Michimasa, A. Olin, D. Ottewell, P. D. Parker, J. G. Rogers, F. Strieder, and C. Wrede. $^{21}\text{Na}(p, \gamma)^{22}\text{Mg}$ reaction and oxygen-neon novae. *Phys. Rev. Lett.*, 90:162501, Apr 2003.
- [10] J. M. Blatt and V. F. Weisskopf. *Theoretical Nuclear Physics*. Wiley, 1952.
- [11] M. F. Bode and A. Evans. *Classical Novae*, volume 43. 2008.
- [12] S. A. Brindhaban, P. H. Barker, M. J. Keeling, and W. B. Wood. Accelerator beam energy calibration with the $^{27}\text{Al}(p, n)$ and $^{27}\text{Al}(p, \gamma)$ reactions. *Nuclear Inst. and Methods in Physics Research, A*, 340(3):436–441, 3 1994.
- [13] E. Brochu, V. M. Cora, and N. de Freitas. A tutorial on Bayesian optimization of expensive cost functions, with application to active user modeling and hierarchical reinforcement learning. 12 2010.
- [14] K. Chipps. Private communication.
- [15] K. A. Chipps, D. W. Bardayan, J. C. Blackmon, K. Y. Chae, U. Greife, R. Hatarik, R. L. Kozub, C. Matei, B. H. Moazen, C. D. Nesaraja, S. D. Pain, W. A. Peters, S. T. Pittman, J. F. Shriner, and M. S. Smith. First direct measurement of the $^{17}\text{F}(p, \gamma)^{18}\text{Ne}$ cross section. *Physical Review Letters*, 102(15):152502, 4 2009.
- [16] K. A. Chipps, D. W. Bardayan, C. D. Nesaraja, M. S. Smith, J. C. Blackmon, K. Y. Chae, B. H. Moazen, S. T. Pittman, U. Greife, R. Hatarik, W. A. Peters, R. L. Kozub, J. F. Shriner, C. Matei, and S. D. Pain. The $^{17}\text{F}(p, \gamma)^{18}\text{Ne}$ resonant cross section. *Physical Review C - Nuclear Physics*, 80(6):065810, 12 2009.
- [17] K. A. Chipps, U. Greife, D. W. Bardayan, J. C. Blackmon, A. Kontos, L. E. Linhardt, M. Matos, S. D. Pain, S. T. Pittman, A. Sachs, H. Schatz, K. T. Schmitt, M. S. Smith, and P. Thompson. The Jet Experiments in Nuclear Structure and Astrophysics (JENSA) gas jet target. *Nuclear Instruments and Methods in Physics Research, Section A: Accelerators, Spectrometers, Detectors and Associated Equipment*, 763:553–564, 2014.
- [18] C. Chronidou, K. Spyrou, S. Harissopulos, S. Kossionides, and T. Paradellis. Resonance strength measurements of the $^{27}\text{Al}(p, \gamma)^{28}\text{Si}$ reaction in the energy range $E_p = 0.8\text{--}2.0$ MeV. *The European Physical Journal A*, 6(3):303–308, 11 1999.
- [19] D. D. Clayton. *Principles of stellar evolution and nucleosynthesis*. 1983.

- [20] R. R. C. Clement, D. Bazin, W. Benenson, B. A. Brown, A. L. Cole, M. W. Cooper, P. A. DeYoung, A. Estrade, M. A. Famiano, N. H. Frank, A. Gade, T. Glasmacher, P. T. Hosmer, W. G. Lynch, F. Montes, W. F. Mueller, G. F. Peaslee, P. Santi, H. Schatz, B. M. Sherrill, M.-J. van Goethem, and M. S. Wallace. New approach for measuring properties of rp -process nuclei. *Phys. Rev. Lett.*, 92:172502, Apr 2004.
- [21] M. Couder, C. Angulo, E. Casarejos, P. Demaret, P. Leleux, and F. Vanderbist. Study of the $^{19}\text{Ne}(p,\gamma)^{20}\text{Na}$ reaction and subsequent improvements to ARES. *Nuclear Physics A*, 758(1-4 SPEC. ISS.):741–744, 2005.
- [22] M. Couder, C. Angulo, W. Galster, J. S. Graulich, P. Leleux, P. Lipnik, G. Tabacaru, and F. Vanderbist. Performance of the ARES recoil separator for (p, γ) reaction measurements. *Nuclear Instruments and Methods in Physics Research, Section A: Accelerators, Spectrometers, Detectors and Associated Equipment*, 506(1-2):26–34, 2003.
- [23] M. Couder, G. P. Berg, J. Görres, P. J. LeBlanc, L. O. Lamm, E. Stech, M. Wiescher, and J. Hinnefeld. Design of the recoil mass separator St. George. *Nuclear Instruments and Methods in Physics Research, Section A: Accelerators, Spectrometers, Detectors and Associated Equipment*, 587(1):35–45, 2008.
- [24] D. D. Cox and S. John. SDO: A statistical method for global optimization. In *in Multidisciplinary Design Optimization: State-of-the-Art*, pages 315–329, 1997.
- [25] A. Cumming. Thermonuclear x-ray bursts: theory vs. observations. *Nuclear Physics B - Proceedings Supplements*, 132:435–445, Jun 2004.
- [26] R. H. Cyburt, A. M. Amthor, A. Heger, E. Johnson, L. Keek, Z. Meisel, H. Schatz, and K. Smith. Dependence of X-ray burst models on nuclear reaction rates. 7 2016.
- [27] R. H. Cyburt, B. D. Fields, K. A. Olive, and T.-H. Yeh. Big bang nucleosynthesis: Present status. *Rev. Mod. Phys.*, 88:015004, Feb 2016.
- [28] B. Davids, R. H. Cyburt, J. José, and S. Mythili. The influence of uncertainties in the $^{15}\text{O}(\alpha, \gamma)^{19}\text{Ne}$ reaction rate on models of type I X-ray bursts. *Astrophysical Journal*, 735(1), 2011.
- [29] A. Di Leva, M. De Cesare, D. Schürmann, N. De Cesare, A. D’Onofrio, L. Gialanella, R. Kunz, G. Imbriani, A. Ordine, V. Roca, D. Rogalla, C. Rolfs, M. Romano, E. Somorjai, F. Strieder, and F. Terrasi. Recoil separator ERNA: Measurement of $^3\text{He}(\alpha, \gamma)^7\text{Be}$. *Nuclear Instruments and Methods in Physics Research, Section A: Accelerators, Spectrometers, Detectors and Associated Equipment*, 595(2):381–390, 2008.

- [30] J. Duris, D. Kennedy, A. Hanuka, J. Shtalenkova, A. Edelen, P. Baxevanis, A. Egger, T. Cope, M. McIntire, S. Ermon, and D. Ratner. Bayesian Optimization of a Free-Electron Laser. *Physical Review Letters*, 124(12), 2020.
- [31] J. M. D’Auria, R. E. Azuma, S. Bishop, L. Buchmann, M. L. Chatterjee, A. A. Chen, S. Engel, D. Gigliotti, U. Greife, D. Hunter, A. Hussein, D. Hutcheon, C. C. Jewett, J. José, J. D. King, A. M. Laird, M. Lamey, R. Lewis, W. Liu, A. Olin, D. Ottewell, P. Parker, J. Rogers, C. Ruiz, M. Trinczek, and C. Wrede. The Na 21 (p , γ) Mg 22 reaction from E c.m. = 200 to 1103 keV in novae and x-ray bursts. *Physical Review C*, 69(6):065803, 6 2004.
- [32] M. T. Emmerich and A. H. Deutz. A tutorial on multiobjective optimization: fundamentals and evolutionary methods. *Natural Computing*, 17(3):585–609, 2018.
- [33] P. M. Endt. Energy levels of A = 21-44 nuclei (VII). *Nuclear Physics, Section A*, 521(C):1–400, 12 1990.
- [34] S. Engel. Commissioning and operation of DRAGON. *Nuclear Instruments and Methods in Physics Research, Section B: Beam Interactions with Materials and Atoms*, 204(November):154–158, 2003.
- [35] J. Fisker, V. Barnard, J. Görres, K. Langanke, G. Martínez-Pinedo, and M. Wiescher. Shell model based reaction rates for rp-process nuclei in the mass range A = 44–63. *Atomic Data and Nuclear Data Tables*, 79(2):241 – 292, 2001.
- [36] J. L. Fisker, J. Gorres, M. Wiescher, and B. Davids. The importance of $^{15}\text{O}(\alpha,\gamma)^{19}\text{Ne}$ to X-ray bursts and superbursts. *The Astrophysical Journal*, 650(1):332–337, 2006.
- [37] J. L. Fisker, F.-K. Thielemann, and M. Wiescher. The nuclear reaction waiting points: ^{22}Mg , ^{26}Si , ^{30}S , and ^{34}Ar and bolometrically double-peaked type I X-ray bursts. *The Astrophysical Journal*, 608(1):L61–L64, 2004.
- [38] D. K. Galloway, A. J. Goodwin, and L. Keek. Thermonuclear burst observations for model comparisons: A reference sample. PASA, 34:e019, Apr. 2017.
- [39] GPy. GPy: A Gaussian process framework in Python, 2012.
- [40] J.-S. Graulich, S. Cherubini, R. Coszach, S. El Hajjami, W. Galster, P. Leleux, W. Bradfield-Smith, T. Davinson, A. Di Pietro, A. C. Shotton, J. Görres, M. Wiescher, F. Binon, and J. Vanhorenbeeck. 7.07 MeV resonant state in ^{19}Ne reexamined through a new measurement of the $^{18}\text{F}(p,\alpha)^{15}\text{O}$ reaction and $^{18}\text{F}(p,p)$ scattering. *Phys. Rev. C*, 63:011302, Dec 2000.

- [41] J. Grindlay, H. Gursky, H. Schnopper, D. R. Parsignault, J. Heise, A. C. Brinkman, and J. Schrijver. Discovery of intense x-ray bursts from the globular cluster NGC 6624. *ApJ*, 205:L127–L130, May 1976.
- [42] A. Hanuka, X. Huang, J. Shtalenkova, D. Kennedy, A. Edelen, V. R. Lalchand, D. Ratner, and J. Duris. Physics-informed Gaussian process for online optimization of particle accelerators. pages 1–6, 2020.
- [43] A. Henriques. Private communication.
- [44] M. Hernanz, J. Gómez-Gomar, and J. José. Gamma-ray signatures of classical novae. *AIP Conference Proceedings*, 587(1):498–507, 2001.
- [45] H. Herndl, J. Görres, M. Wiescher, B. A. Brown, and L. Van Wormer. Proton capture reaction rates in the rp process. *Phys. Rev. C*, 52:1078–1094, Aug 1995.
- [46] A. Hood. Private communication.
- [47] D. A. Hutcheon, S. Bishop, L. Buchmann, M. L. Chatterjee, A. A. Chen, J. M. D’Auria, S. Engel, D. Gigliotti, U. Greife, D. Hunter, A. Hussein, C. C. Jewett, N. Khan, M. Lamey, A. M. Laird, W. Liu, A. Olin, D. Ottewell, J. G. Rogers, G. Roy, H. Sprenger, and C. Wrede. The DRAGON facility for nuclear astrophysics at TRIUMF-ISAC: Design, construction and operation. *Nuclear Instruments and Methods in Physics Research, Section A: Accelerators, Spectrometers, Detectors and Associated Equipment*, 498(1-3):190–210, 2003.
- [48] C. Iliadis. *Nuclear Physics of Stars*. John Wiley Sons, Ltd, 2015.
- [49] C. Iliadis, A. Champagne, J. Jose, S. Starrfield, and P. Tupper. The Effects of Thermonuclear Reaction-Rate Variations on Nova Nucleosynthesis: A Sensitivity Study. *The Astrophysical Journal Supplement Series*, 142:105–137, 2002.
- [50] C. Iliadis, J. M. D’Auria, S. Starrfield, W. J. Thompson, and M. Wiescher. Proton-induced thermonuclear reaction rates for $\{A\} = 20\text{--}40$ nuclei. *The Astrophysical Journal Supplement Series*, 134(1):151–171, 2001.
- [51] J. F. Ziegler. The stopping and range of ions in matter, 2011.
- [52] A. Jokar, O. Kakuee, M. Lamehi-Rachti, N. Sharifzadeh, and V. Fathollahi. Differential cross section measurements of $^{27}\text{Al}(p,p/\gamma)^{27}\text{Al}$ and $^{27}\text{Al}(p,\alpha\gamma)^{24}\text{Mg}$ reactions in the

energy range of 1.6-3.0 MeV. *Nuclear Instruments and Methods in Physics Research, Section B: Beam Interactions with Materials and Atoms*, 362:138–141, 2015.

- [53] J. José, A. Coc, and M. Hernanz. Synthesis of intermediate-mass elements in classical novae: From Si to Ca. *ApJ*, 560(2):897–906, Oct. 2001.
- [54] J. José, M. Hernanz, and C. Iliadis. Nucleosynthesis in classical novae. *Nuclear Physics A*, 777:550–578, 10 2006.
- [55] L. Keek, R. H. Cyburt, and A. Heger. Reaction rate and composition dependence of the stability of thermonuclear burning on accreting neutron stars. *Astrophysical Journal*, 787(2), 2014.
- [56] J. J. Kolata, A. Roberts, A. M. Howard, D. Shapira, J. F. Liang, C. J. Gross, R. L. Varner, Z. Kohley, A. N. Villano, H. Amro, W. Loveland, and E. Chavez. Fusion of $^{124,132}\text{Sn}$ with $^{40,48}\text{Ca}$. *Physical Review C - Nuclear Physics*, 85(5):054603, 5 2012.
- [57] A. Kontos, D. SchürmannSch, C. Akers, M. Couder, D. Robertson, E. Stech, R. Talwar, and M. Wiescher. HIPPO: A supersonic helium jet gas target for nuclear astrophysics. 2011.
- [58] R. M. Kremer, C. A. Barnes, K. H. Chang, H. C. Evans, B. W. Filippone, K. H. Hahn, and L. W. Mitchell. Coincidence measurement of the $^{12}\text{C}(\alpha,\gamma)^{16}\text{O}$ cross section at low energies. *Physical Review Letters*, 60(15):1475–1478, 4 1988.
- [59] H. J. Kushner. A new method of locating the maximum point of an arbitrary multipeak curve in the presence of noise. *Journal of Basic Engineering*, 86(1):97–106, 03 1964.
- [60] D. Q. Lamb. Some startling discoveries about X-ray bursts. *The Astrophysical Journal Supplement Series*, 127(2):395–408, 2000.
- [61] W. H. G. Lewin, J. van Paradijs, and R. E. Taam. X-ray bursts. *Space Sci. Rev.*, 62(3-4):223–389, Sept. 1993.
- [62] L.-Y. Lin. *Rare Isotope Beam Energy Measurements and Scintillator Developments for ReA3*. PhD thesis, Michigan State University, 2015.
- [63] D. J. Lizotte. *Practical Bayesian Optimization*. PhD thesis, University of Alberta, CAN, 2008. AAINR46365.

- [64] K. Makino and M. Berz. COSY INFINITY version 9. *Nuclear Instruments and Methods in Physics Research, Section A: Accelerators, Spectrometers, Detectors and Associated Equipment*, 558(1):346–350, 2006.
- [65] J. B. Marion. Accelerator calibration energies. *Reviews of Modern Physics*, 38(4):660–668, 10 1966.
- [66] M. Matoš, A. Estradé, H. Schatz, D. Bazin, M. Famiano, A. Gade, S. George, W. G. Lynch, Z. Meisel, M. Portillo, A. Rogers, D. Shapira, A. Stolz, M. Wallace, and J. Yurkon. Time-of-flight mass measurements of exotic nuclei. *Nuclear Instruments and Methods in Physics Research, Section A: Accelerators, Spectrometers, Detectors and Associated Equipment*, 696:171–179, 12 2012.
- [67] M. McIntire, T. Cope, D. Ratner, and S. Ermon. Bayesian optimization of FEL performance at LCLS. *IPAC 2016 - Proceedings of the 7th International Particle Accelerator Conference*, pages 2972–2975, 2016.
- [68] Z. Meisel. Consistent modeling of GS 1826-24 x-ray bursts for multiple accretion rates demonstrates the possibility of constraining rp-process reaction rates. *ApJ*, 860(2):147, June 2018.
- [69] Z. Meisel, M. T. Moran, G. Gilardy, J. Schmitt, C. Seymour, and M. Couder. Energy acceptance of the St. George recoil separator. *Nuclear Instruments and Methods in Physics Research, Section A: Accelerators, Spectrometers, Detectors and Associated Equipment*, 850(January):48–53, 2017.
- [70] M. Meyer and N. Wolmarans. A study of the excited states of ^{28}Si by means of the $^{27}\text{Al}(p, \gamma)^{28}\text{Si}$ reaction in the energy range $E_p = 0.1\text{--}29.01$ MeV. *Nuclear Physics A*, 136(3):663–672, 1969.
- [71] J. Mockus, V. Tiesis, and A. Zilinskas. The application of Bayesian methods for seeking the extremum. *Towards Global Optimization*, 2(117-129):2, 1978.
- [72] L. Morales, C. Seymour, M. Couder, A. Dombos, S. Moylan, G. Gilardy, J. Hinnefeld, P. Huestis, D. Robertson, E. Stech, M. Skulski, G. P. A. Berg, and M. Wiescher. First detection of ^{18}F from the $^{14}\text{N}(\alpha, \gamma)^{18}\text{F}$ reaction with the St. George recoil mass separator. In *APS Division of Nuclear Physics Meeting Abstracts*, volume 2019 of *APS Meeting Abstracts*, page EG.009, Jan. 2019.
- [73] M. Newville, K. Lauer, Dchabot, T. A. Caswell, A. Péteut, S. Hartman, Rokvintar, R. Clarken, D. Allan, and T. Birke. pyepics/pyepics 3.2.7, 2017.

- [74] I. Orion and L. Wielopolski. Response function of the BGO and NaI(Tl) detectors using Monte Carlo simulations. *Annals of the New York Academy of Sciences*, 904, 2000.
- [75] A. Parikh, J. José, F. Moreno, and C. Iliadis. The effects of variations in nuclear processes on type I X-ray burst nucleosynthesis. *The Astrophysical Journal Supplement Series*, 178(1):110–136, 2008.
- [76] A. Parikh, J. José, G. Sala, and C. Iliadis. Nucleosynthesis in type I X-ray bursts. *Progress in Particle and Nuclear Physics*, 69:225–253, 3 2013.
- [77] C. J. Prokop, S. N. Liddick, B. L. Abromeit, A. T. Chemey, N. R. Larson, S. Suchyta, and J. R. Tompkins. Digital data acquisition system implementation at the National Superconducting Cyclotron Laboratory. *Nuclear Instruments and Methods in Physics Research, Section A: Accelerators, Spectrometers, Detectors and Associated Equipment*, 741:163–168, 2014.
- [78] D. Psaltis. Accreting neutron stars and black holes: a decade of discoveries. *Compact Stellar X-ray Sources*, pages 1–38, 2009.
- [79] C. E. Rasmussen and C. K. I. Williams. *Gaussian Processes for Machine Learning*. MIT Press, Cambridge, 2018.
- [80] T. Rauscher and F.-K. Thielemann. Tables of nuclear cross sections and reaction rates: an addendum to the paper “Astrophysical reaction rates from statistical model calculations”. *Atomic Data and Nuclear Data Tables*, 79(1):47 – 64, 2001.
- [81] D. Rogalla, D. Schürmann, F. Strieder, M. Aliotta, N. DeCesare, A. DiLeva, C. Lubritto, A. D’Onofrio, L. Gialanella, G. Imbriani, J. Kluge, A. Ordine, V. Roca, H. Röcken, C. Rolfs, M. Romano, F. Schümann, F. Terrasi, and H. P. Trautvetter. Recoil separator ERNA: Acceptances in angle and energy. *Nuclear Instruments and Methods in Physics Research, Section A: Accelerators, Spectrometers, Detectors and Associated Equipment*, 513(3):573–578, 2003.
- [82] R. Roussel, A. Hanuka, and A. Edelen. Multi-objective Bayesian optimization for accelerator tuning, 2020.
- [83] C. Ruiz, U. Greife, and U. Hager. Recoil separators for radiative capture using radioactive ion beams: Recent advances and detection techniques, 2014.

- [84] H. Schatz, A. Aprahamian, V. Barnard, L. Bildsten, A. Cumming, M. Ouellette, T. Rauscher, F.-K. Thielemann, and M. Wiescher. End point of the rp process on accreting neutron stars. *Phys. Rev. Lett.*, 86:3471–3474, Apr 2001.
- [85] H. Schatz, A. Aprahamian, J. Göres, M. Wiescher, T. Rauscher, J. F. Rembges, F. K. Thielemann, B. Pfeiffer, P. Möller, K. L. Kratz, H. Herndl, B. A. Brown, and H. Rebel. Rp-process nucleosynthesis at extreme temperature and density conditions. *Physics Report*, 294(4):167–263, 1998.
- [86] B. Shahriari, K. Swersky, Z. Wang, R. P. Adams, and N. de Freitas. Taking the human out of the loop: A review of Bayesian optimization. *Proceedings of the IEEE*, 104(1):148–175, 2016.
- [87] R. J. Shaloo, S. J. Dann, J. N. Gruse, C. I. Underwood, A. F. Antoine, C. Arran, M. Backhouse, C. D. Baird, M. D. Balcazar, N. Bourgeois, J. A. Cardarelli, P. Hatfield, J. Kang, K. Krushelnick, S. P. Mangles, C. D. Murphy, N. Lu, J. Osterhoff, K. Pöder, P. P. Rajeev, C. P. Ridgers, S. Rozario, M. P. Selwood, A. J. Shahani, D. R. Symes, A. G. Thomas, C. Thornton, Z. Najmudin, and M. J. Streeter. Automation and control of laser wakefield accelerators using Bayesian optimisation. *arXiv*, pages 0–7, 2020.
- [88] D. Shapira, T. Lewis, and L. Hulett. A fast and accurate position-sensitive timing detector based on secondary electron emission. *Nuclear Instruments and Methods in Physics Research Section A: Accelerators, Spectrometers, Detectors and Associated Equipment*, 454(2-3):409–420, 11 2000.
- [89] A. Simon, J. Fallis, A. Spyrou, A. M. Laird, C. Ruiz, L. Buchmann, B. R. Fulton, D. Hutcheon, L. Martin, D. Ottewell, and A. Rojas. Radiative capture reactions with heavy beams: Extending the capabilities of DRAGON. *European Physical Journal A*, 49(5):1–5, 2013.
- [90] S. K. Sjue, B. S. Nara Singh, P. Adsley, L. Buchmann, M. Carmona-Gallardo, B. Davids, J. Fallis, B. R. Fulton, N. Galinski, U. Hager, M. Hass, D. Howell, D. A. Hutcheon, A. M. Laird, L. Martin, D. Ottewell, S. Reeve, C. Ruiz, G. Ruprecht, and S. Triambak. Beam suppression of the DRAGON recoil separator for ${}^3\text{He}(\alpha, \gamma){}^7\text{Be}$. *Nuclear Instruments and Methods in Physics Research, Section A: Accelerators, Spectrometers, Detectors and Associated Equipment*, 700:179–181, 2013.
- [91] M. Smith, C. Rolfs, and C. Barnes. A recoil separator for use in radioactive ion beam experiments. *Nuclear Instruments and Methods in Physics Research Section A: Accelerators, Spectrometers, Detectors and Associated Equipment*, 306(1-2):233–239, 8 1991.

- [92] The GPyOpt authors. GPyOpt: a Bayesian optimization framework in Python, 2016.
- [93] F.-K. Thielemann, F. Brachwitz, C. Freiburghaus, E. Kolbe, G. Martinez-Pinedo, T. Rauscher, F. Rembges, W. Hix, M. Liebendörfer, A. Mezzacappa, K.-L. Kratz, B. Pfeiffer, K. Langanke, K. Nomoto, S. Rosswog, H. Schatz, and W. Wiescher. Element synthesis in stars. *Progress in Particle and Nuclear Physics*, 46(1):5–22, 2001.
- [94] H. Trautvetter, K. Elix, C. Rolfs, and K. Brand. Energy determination of heavy-ion beams. *Nuclear Instruments and Methods*, 161(2):173–182, 5 1979.
- [95] N. Ueta, V. H. Rotberg, D. Pereira, M. N. Rao, and O. Sala. Calibration of the tandem pelletron accelerator. *Revista Brasileira de Física*, 6(3):413, 1976.
- [96] A. C. C. Villari, D. B. Crisp, A. Lapierre, S. Nash, T. Summers, and Q. Zhao. Energy calibration of the ReA3 accelerator by time-of-flight technique1. *Journal of Physics: Conference Series*, 1350:012156, November 2019.
- [97] R. K. Wallace and S. E. Woosley. Explosive hydrogen burning. *ApJS*, 45:389–420, Feb. 1981.
- [98] B. Warner. *Cataclysmic Variable Stars*. Cambridge Astrophysics. Cambridge University Press, 1995.
- [99] S. E. Woosley, A. Heger, A. Cumming, R. D. Hoffman, J. Pruet, T. Rauscher, J. L. Fisker, H. Schatz, B. A. Brown, and M. Wiescher. Models for Type I X-Ray Bursts with Improved Nuclear Physics. *The Astrophysical Journal Supplement Series*, 151(1):75–102, 2004.
- [100] M. Zamfir, A. Cumming, and D. K. Galloway. Constraints on neutron star mass and radius in GS 1826-24 from sub-eddington x-ray bursts. *ApJ*, 749(1):69, Apr. 2012.
- [101] J. F. Ziegler, M. D. Ziegler, and J. P. Biersack. SRIM - The stopping and range of ions in matter (2010). *Nuclear Instruments and Methods in Physics Research, Section B: Beam Interactions with Materials and Atoms*, 268(11-12):1818–1823, 2010.